Technical University Munich
School of Natural Sciences
Department of Physics

Development of the Optical Module and Environmental Monitoring Prospects for the Pacific Ocean Neutrino Experiment

Martin Dinkel

March 20, 2024

Master Thesis

Chair of Experimental Physics with Cosmic Particles

First Examiner: Prof. Dr. Elisa Resconi
Second Examiner: Prof. Dr. Lothar Oberauer
Advisor: M.Sc. Christian Spannfellner

Abstract

The Pacific Ocean Neutrino Experiment (P-ONE) is a large-scale, multi-cubic-kilometre Neutrino Telescope currently under development. It will be located in the North-East Pacific at the Cascadia Basin, 200 km offshore Vancouver Island, in a depth of 2660 metres. The first functional line P-ONE-1 of the future detector is planned to be deployed in 2025. P-ONE-1 consists of 20 optical and calibration modules distributed over a length of around one kilometre and is designed to serve as a blueprint for future detector lines.

In the scope of this thesis, the current design of P-ONE-1s' Optical Module (P-OM) and the planned production of the P-OM are presented. The P-OM comprises two glass hemispheres attached to a titanium assembly cylinder between both hemispheres. In each hemisphere, eight photomultiplier tubes (PMTs) are arranged to detect Cherenkov light emitted by secondary particles produced by neutrino interactions. The PMTs are optically coupled to the glass hemisphere with an optical gel pad. The multi-PMT design enables the management of elevated background rates in the depths of the North-East Pacific Ocean. At the same time, the P-OM's streamlined and modular mechanical structure facilitates effortless scalability for the construction of the complete P-ONE detector.

In this thesis, the focus lies on three main topics: First, the preparation of the PMTs for the production of the P-OMs, including a characterisation test, and setting up a scalable production line for the hemispheres. Second, CTD data taken close to the site of P-ONE-1 were analysed, and water samples from the deep sea at Cascadia Basin were tested regarding the attenuation length. Last, the development of an Oceanography Sensor Interface will be presented. It shall be able to transmit power and communication wireless from the inside of the module to an outside receiver device.

Acknowledgments

Firstly, it should be noted that this work would not have been possible without the excellent work of the ECP working group at TUM and the P-ONE collaboration.

Additionally, I want to thank the Hanns-Seidel-Stiftung for supporting me over the whole duration of my studies.

I sincerely thank Professor Elisa Resconi for providing and enabling this thesis. The level of trust and responsibility given to me is truly remarkable and allowed me to gain valuable insights into the project and the research. I would also like to express my gratitude for the opportunity to travel to the collaboration meetings in Krakow and Philadelphia and the characterisation testing in Aachen.

I would also like to thank the entire P-ONE-1 working group here at TUM. The weekly meetings and discussions with you were always productive and helpful but also uplifting. Without all of you and your constant input and assistance, this work would not have turned out as it is now.

I want to express my sincere gratitude to Vincent Rompel for his constant support and tireless willingness to prepare the setup for the water sample measurements and to conduct the experiments together. Without you, these measurements would not have been possible. Thank you very much!

I would like to express special thanks to Christian Spannfellner for supervising my work and your trust in me and my work. I also want to thank you for the many helpful tips, discussions and suggestions.
I also want to thank Lea Ginzkey, who tirelessly worked with me on the development of the production and integration of the P-OM, always maintaining order and overview. Without you, the production of the P-OMs would not be in such a good state.
Furthermore, I would like to thank Vincent Gousy-Leblanc for your patience and perseverance in introducing me to the world of PMTs and always being open to questions. I am especially grateful for your help with the characterisation tests of the PMTs. I'm glad to call all three of you my friends now. Thank you all!

Furthermore, I would like to thank my parents, who have always supported me throughout my entire studies, including the final thesis during the last twelve months.

Finally, I want to thank my girlfriend for her unconditional love and support. Especially during the past year, it was reassuring to always have you by my side and to rely on your support. Thank you for being by my side.

Contents

1 Multimessenger Physics Introduction **1**
1.1 Cosmic Rays . . . 2
1.2 Gamma Rays . . . 2
1.3 Gravitational Waves . . . 3
1.4 Neutrinos . . . 3

2 Neutrino Detection **5**
2.1 Principle of Neutrino Interaction . . . 5
2.2 Neutrino Oscillations . . . 6
2.3 Neutrino Signatures . . . 7
2.4 Neutrino Flux . . . 9
2.5 Astrophysical Sources of Neutrinos . . . 12
2.6 Neutrino Telescopes . . . 13

3 Pacific Ocean Neutrino Experiment (P-ONE) **18**
3.1 Pathfinder Missions . . . 18
3.2 P-ONE-1 . . . 20

4 P-ONE Optical Module **22**
4.1 Conceptional Design . . . 22
4.2 PMTs and μBase . . . 23
4.3 Production of the Optical Module . . . 28
4.4 Evaluation of Assembled Hemispheres . . . 34
4.5 Outlook . . . 35

5 Oceanphysics Introduction **36**
5.1 Properties of Water . . . 36
5.2 Salinity . . . 37
5.3 Dissolved Gases in Oceans . . . 39
5.4 Physical Oceanography . . . 43

6 Water Characterization in Cascadia Basin **48**
6.1 Analysis of CTD data at Cascadia Basin . . . 48
6.2 Optical Characterisation of Water Samples from Cascadia Basin . . . 52
6.2.1 Experimental Setup at TUM . . . 53
6.2.2 Optical Properties of Water Samples . . . 56

7 Oceanography Sensor Interface **74**
7.1 Wireless Power Transfer . . . 75
7.2 Wireless Communication System . . . 82
7.3 Integration in Optical Module . . . 82
7.4 Outlook for the Oceanography Sensor Interface . . . 85

A Appendix **87**
A.1 Coating Procedure of PMTs 87
A.2 Procedure of Gel Pad Production 90
A.3 Procedure of PMT Integration 96

1 Multimessenger Physics Introduction

Since ancient times, humankind has observed the stars and the sky. However, their exploration of the universe was confined to observations in the visible optical spectrum. Though, as the 20th century unfolded, the capacity to perceive the cosmos expanded significantly. The advent of radio spectrum exploration and the deployment of space-based telescopes marked a key moment, allowing to delve into areas beyond the optical spectrum. This technological leap opened new frontiers, enabling the observation of astrophysical phenomena in radio, infrared, ultraviolet, and X-ray wavelengths. The early 21st century witnessed a transformative phase in astronomical instrumentation. Gravitational wave detectors, neutrino telescopes, and cosmic ray detectors emerged as useful tools. This confluence of diverse observation techniques gave rise to the interdisciplinary field of multimessenger astronomy [1, 2]. One of the components of multimessenger astronomy is the utilisation of neutrino telescopes. These detectors have been instrumental in capturing signals from astrophysical neutrino sources. Recent observations from these telescopes have focused on the galactic plane [1, 3]. Recently, researchers identified neutrino emissions from the galactic plane with a significance level of $4.5\,\sigma$. The observed signal aligns with the modelled diffuse emission from the galactic plane. However, intriguingly, it could also originate from a population of unresolved point sources within the region [3]. Accompanying this discovery, a graphical representation of the galactic plane showcases the different messengers at play. This visual representation highlights the synergy between various observational techniques, offering a comprehensive view of the astrophysical phenomena in this celestial region [3].

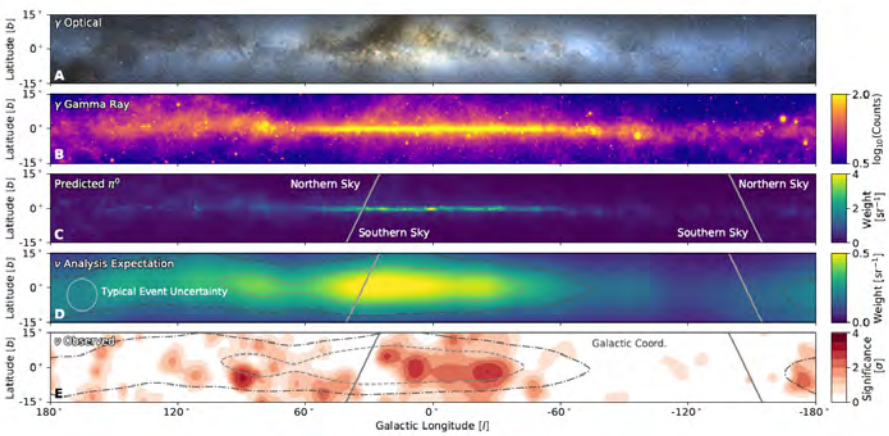

Fig. 1.1: The plane of the Milky Way galaxy in photons and neutrinos [3].

Furthermore, specific signals from sources such as TXS 0506+056 and NGC 1068 have been detected, adding further layers to our understanding of cosmic events [4, 5]. In multimessenger astronomy, several crucial astrophysical messengers play pivotal roles in discovering the universe. The following sections introduce these key messengers, highlighting their characteristics and contributions to our cosmic knowledge.

1.1 Cosmic Rays

Cosmic rays primarily consist of ionised nuclei, mostly comprising high-energy protons, alpha particles and heavier nuclei. Those cosmic rays that remain in space and have not undergone any interaction with the Earth´s atmosphere are named primary cosmic rays. After interacting with the earth´s atmosphere, the resulting particles are called secondary cosmic rays. The interaction process is described by the following formula 1.1 [1, 2, 6].

$$p + N \rightarrow \pi^{\pm}, \pi^{0}, K^{\pm}, K^{0}, p, n, ... \tag{1.1}$$

This signifies that primary cosmic rays undergo hadronic decay due to atmospheric interaction, producing neutrinos, protons, kaons, and pions. Subsequently, secondary cosmic rays interact strongly with atmospheric nuclei, initiating a cascade of hadronic particles known as hadronic showers [1]. Charged pions and kaons contribute to the generation of a weakly interacting muonic and neutrino component. Muons with relativistic energies are produced during the atmospheric shower, and despite their short lifetimes, they can reach the Earth's surface [2]. An additional electromagnetic component is introduced through the decay of pions and the production of positrons and electrons. Hereby, the decay of neutral pions plays a pivotal role, as illustrated in the following formula 1.2. The resulting photons have energies high enough for pair production, leading to the creation of positron-electron pairs. Photons can also be generated through bremsstrahlung of charged particles [1, 2].

$$\pi^{0} \rightarrow \gamma + \gamma \tag{1.2}$$

1.2 Gamma Rays

Gamma rays can emerge due to cosmic ray interactions during their journey through the universe. These high-energy photons result from various intricate processes, each contributing to the dynamic interplay of cosmic observations. One prominent mechanism giving rise to gamma rays is synchrotron radiation induced by the interaction of cosmic rays with magnetic fields. This process involves the acceleration of charged particles along curved paths, leading to the emission of gamma rays as they release energy in the form of photons [1]. Similarly, bremsstrahlung, caused by the interaction of cosmic rays with electric fields, contributes to generating gamma rays. In this process, charged particles emit gamma rays as they accelerate or decelerate in the presence of electric forces [1]. As already described in section 1.1, neutral pions can decay into photons. During this decay, photons with energies in the gamma spectrum can be generated. The inverse Compton effect adds another way to gamma ray production. In this phenomenon, ultra-relativistic electrons or other charged particles scatter on photons like those from the Cosmic Microwave Background (CMB) [1]. This interaction transfers energy to the photons, resulting in the potential emission of high-energy gamma rays.

Despite these various production processes of gamma rays, the Earth's atmosphere acts as a shield against specific wavelengths of electromagnetic radiation. This leads to the development

of two distinct detection principles for gamma rays. The ground-based detection principle involves observing Cherenkov light emitted by secondary particles in the atmosphere when gamma rays interact with it. This indirect detection method allows scientists to measure the presence of gamma rays by studying the cascades of secondary particles produced during interactions. In contrast, space-based detection is employed for gamma rays in the MeV to a few GeV range. Placing detectors in space eliminates the interference and absorption effects caused by the atmosphere, enabling a more direct measurement of gamma rays [1].

1.3 Gravitational Waves

Gravitational waves, small disruptions in space-time, result from the acceleration or deformation of massive celestial bodies. These waves propagate at the speed of light. They are generated by some of the most violent and energetically intense events in the universe, such as the collision of black holes, the merging of neutron stars, or the explosive demise of supernovae. Gravitational waves serve as messengers from these cosmic events, and their weak interactions allow them to carry unimpeded information about their origins. Unlike other particles affected by electric or magnetic fields, gravitational waves provide a unique and undistorted view into the universe's most extreme phenomena [7].

As gravitational waves travel from their source through the universe, they cause disturbances in space-time, inducing squeezing and dragging effects. The historical measurement of the first space-time distortion occurred on 14 September 2015, when the Laser Interferometer Gravitational-Wave Observatory (LIGO) detected the collision of two black holes [7]. As the effects of gravitational waves on Earth are subtle, the precision of their detection requires careful consideration of systematic errors. Minor vibrations or seismic activity on Earth can potentially disturb the signals, necessitating rigorous measures to eliminate such interference. The LIGO comprises two similar setups in the United States, specifically in Livingston and Hanford. The signals detected at these sites are meticulously compared, and only coincident signals are considered possible gravitational wave events [7]. To ascertain the direction of the gravitational wave source, signal triangulation is used. This triangulation is achieved by employing a global network of detectors, including both LIGO facilities, Virgo in Italy, GEO600 in Germany, and KAGRA in Japan. Collaboration among these observatories allows scientists to pinpoint the celestial events giving rise to gravitational waves, enhancing our understanding of the universe's most energetic and cataclysmic events [8, 9, 10].

1.4 Neutrinos

Neutrinos, as exclusively weak-interacting leptonic particles, present a unique and challenging subject of study in high-energy astrophysics. Compared to cosmic rays and gamma rays, their detection proves to be a more difficult task due to their low interaction cross-section and constraints imposed by the limitations to weak interactions. Neutrinos, as electromagnetic neutral particles, remain unaffected by electric or magnetic fields, experiencing no deflections. This

property enables them to traverse vast cosmic distances unimpeded, making them ideal candidates for point source searches in the cosmos [11]. In the following, the characteristics and sources of astrophysical neutrinos are introduced.

2 Neutrino Detection

2.1 Principle of Neutrino Interaction

Neutrino interactions

As introduced above, neutrinos stand out for their unique characteristic of lacking electromagnetic charge, which renders them impervious to electromagnetic interactions. As lepton particles, they naturally steer clear of strong interactions, engaging exclusively in weak interactions [12]. The weak force, one of the four fundamental forces known to date, is mediated by gauge bosons, namely the Z^0 and $W^{\pm}$ bosons. However, the high mass ($m_{W^{\pm}} = 80.398 \pm 0.025$ GeV and $m_{Z^0} = 91.188 \pm 0.002$ GeV [12]) of these bosons limit their propagator during the exchange process, leading to the ultimate suppression of weak interactions [13]. Two distinct types of interactions when neutrinos encounter a nucleon (N) exist. The Charged-Current (CC) interaction involves the exchange of $W^{\pm}$ bosons, and the Neutral-Current (NC) interaction is facilitated by Z^0 bosons. Neutrinos exhibit different flavours corresponding to their charged lepton counterparts: electron, muon, and tau. Direct observation of the interaction of neutrinos with matter is technically not possible. Instead, detectors are used to measure charged secondary particles produced during the interaction process of neutrinos with a nucleus. The primary principle is detecting photons generated by these secondary charged particles through the Cherenkov effect.

$$\nu_l + N \rightarrow l + X \qquad \text{(CC)} \tag{2.1}$$

$$\nu_l + N \rightarrow \nu_l + X \qquad \text{(NC)} \tag{2.2}$$

Cherenkov effect

Cherenkov radiation, also known as Cherenkov light, is a phenomenon observed when a charged particle traverses a medium at a speed exceeding the phase velocity of light in that medium. The phase velocity of light in a medium, denoted as c_n, is given by the equation 2.3 [14].

$$c_n = \frac{c}{n} \tag{2.3}$$

Here, c is the speed of light in a vacuum, and n is the refractive index, which varies with the wavelength of light. As a charged particle moves through the medium, it polarises the surrounding molecules, causing the orientation of dipoles and consequent energy loss in the particle. Upon the passage of the charged particle, the dipoles return to their ground state, releasing energy in the form of electromagnetic radiation – the Cherenkov light. The interference of electromagnetic waves produces a characteristic light cone with an opening angle θ [14].

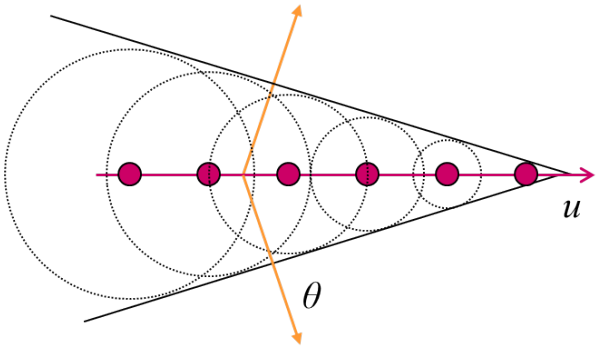

Fig. 2.1: The schematic of Cherenkov light for a moving charged particle with velocity u. [15]

The correlation between the opening angle and the velocity of the charged particle is governed by the equation 2.4.

$$\cos\theta = \frac{c}{u \cdot n} \tag{2.4}$$

Furthermore, the estimation of the number of Cherenkov photons N_C released per unit distance travelled $\mathrm{d}x$ and unit wavelength interval $\mathrm{d}\lambda$ by a charged particle with charge $q = z \cdot e$ can be expressed by the equation 2.5 [1, 16].

$$\frac{d^2 N_C}{\mathrm{d}x\mathrm{d}\lambda} = \frac{4\pi^2 q^2}{hc\lambda^2}\left(1 - \frac{c^2}{n(\lambda)^2 v^2}\right) \tag{2.5}$$

Cherenkov photons exhibit a distinctive wavelength dependency of $1/\lambda^2$ within a range of 300 nm to 600 nm. However, the photons undergo absorption and scattering within the medium. Considering these propagation effects is crucial for simulating and reconstructing events, emphasising the need for a detailed understanding of the medium's optical properties [17]. The interplay of Cherenkov radiation and the medium's optical characteristics forms the basis for diverse applications in particle and astrophysics.

2.2 Neutrino Oscillations

Neutrinos are produced and detected in a specific flavour state. The flavour of a neutrino determines the production of distinctive secondaries with different signatures at interactions. The phenomenon of neutrino oscillation allows neutrinos to change flavour as they propagate. This means a specific flavour is a quantum-mechanical superposition of mass eigenstates. Neutrinos come in three flavours: electron, muon, and tau, and correspondingly, they have three mass eigenstates. If neutrinos have a non-vanishing rest mass, these eigenstates need not be the same. However, they are intricately connected through the Pontecorvo-Maki-Nakagawa-Sakata (PMNS) matrix, defined by the equation 2.6 [1].

$$\begin{pmatrix} |\nu_e\rangle \\ |\nu_\mu\rangle \\ |\nu_\tau\rangle \end{pmatrix} = \begin{pmatrix} U_{e1} & U_{e2} & U_{e3} \\ U_{\mu 1} & U_{\mu 2} & U_{\mu 3} \\ U_{\tau 1} & U_{\tau 2} & U_{\tau 3} \end{pmatrix} \cdot \begin{pmatrix} |\nu_1\rangle \\ |\nu_2\rangle \\ |\nu_3\rangle \end{pmatrix} \tag{2.6}$$

This rotation matrix can be parametrised by the mixing angles θ_{12}, θ_{23}, θ_{13} and a CP violating phase angle δ_{CP}, revealing the coherence between flavour and mass eigenstates of neutrinos. Neutrinos produced with a flavour α at a source at $t = 0$ evolve over time according to formula 2.7 [1].

$$|\nu_j(x,t)\rangle = \sum_i U_{\alpha i} e^{-iE_i t} |\nu_i\rangle \,. \tag{2.7}$$

The relativistic energy of the mass eigenstates is defined by the formula 2.8.

$$E_i = \sqrt{m_i^2 + p_i^2} \simeq p_i + \frac{m_i^2}{2p_i} \simeq E + \frac{m_i^2}{2E} \tag{2.8}$$

with E $\approx$ p as neutrino energy and p $\gg$ $\mathrm{m_i}$. The three mass eigenstates evolve differently over time, leading to potential differences in their final measured flavour compared to the initial one.

The oscillation probability $P(\alpha \to \beta)$ for neutrinos, in compliance with the CP invariance, is defined by the formula 2.9.

$$P(\alpha \to \beta) = \mid \langle \nu_\beta \mid \nu(x,t) | \nu_\beta \mid \nu(x,t) \rangle \mid^2 = \delta_{\alpha\beta} - 4 \sum_{j>i} U_{\alpha i} U_{\alpha j} U_{\beta i} U_{\beta j} sin^2 (\frac{\Delta m_{ij}^2}{4} \frac{L}{E}) \tag{2.9}$$

Hereby it is apparent, that the oscillation probability $P(\alpha \to \beta)$ depends on the mass differences $\Delta m_{ij}^2 = m_i^2 - m_j^2$, the distance L traveled, and the neutrino energy E. Neutrino oscillations are only possible if at least one mass eigenstate is non-zero. This implies that neutrinos must have a non-vanishing rest mass, wherein current limits indicate $m_\nu < 0.8\,\mathrm{eV}$ [18]. The oscillation studies provide information about the mass hierarchy, although they cannot determine the absolute mass limit. Additionally, the transition probability depends on the fraction of the distance travelled (L) and the neutrino energy (E), a crucial aspect for neutrinos of cosmic origin travelling large distances. This means for astrophysical measurement of neutrinos, the three-flavour oscillation averages out over astronomical distances, resulting in nearly equal fractions of measured flavours, independent from the initial flavour [2].

2.3 Neutrino Signatures

As previously highlighted in section 2.1, neutrinos exhibit weak interactions in two distinct types: Charged Current and Neutral Current. The nature of the interaction type dictates the

resulting secondary particles. Astrophysical neutrinos, characterised by their high energy, are able to penetrate nucleons and scatter deep-inelastic with them, initiating hadronic cascades through strong interactions [14]. The diversity in secondary particles produced during neutrino interactions leads to different signatures, offering insights into the specifics of the interaction with matter. The secondary particle's flavour is flavour-dependent in the case of CC interactions. Each neutrino flavour corresponds to a unique secondary particle, and these particles manifest specific signatures within the medium. In contrast to that, NC interactions are flavour-independent.

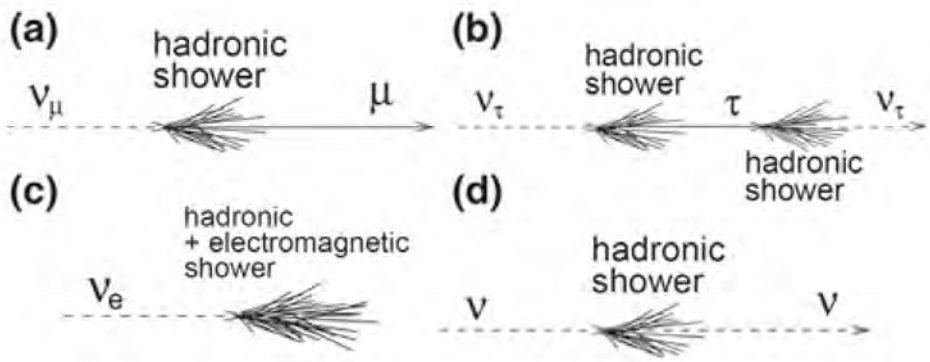

Fig. 2.2: Signature topology for neutrino interaction types with matter. (a), (b) and (c) show the flavour-dependent charged current interaction types, and (d) the flavour-independent neutral current interaction process.[1]

As shown in figure 2.2 (a) a muon neutrino ν_μ produces at the CC interaction with a nucleon a hadronic shower. During the interaction of a muon neutrino and the nucleus, a secondary muon is created. While the secondary muon propagates through the matter, it creates a track-like signature. The path length of the muon depends on its initial energy and is in water around 5 km for a 10 TeV muon. For reconstruction, it must be considered that the photons caused by the travelling muon underlie scattering and absorption within the medium. This could be done with a likelihood function comparing the time and position of the fired photosensors to the expectation of the Cherenkov signal. Therefore, for an exact reconstruction, a distinct knowledge of the optical properties in the detector is mandatory [1, 6].

The CC interaction of a tau neutrino ν_τ with matter is demonstrated in figure 2.2 schema (b). This process contains two hadronic shower events. The first is created at the first vertex, when the tau neutrino interacts with a nucleus, wherein a secondary tau and a first hardonic shower is produced. The secondary tau propagates through the matter and decays, releasing a tau neutrino by producing a second hadronic shower. The distance the secondary tau can travel depends on the energy of the tau. If the tau has enough energy and therefore can travel a distance which allows a separated detection of the first and the second hadronic shower, the signature of the charged current interaction of the tau neutrino is called double bang event [1,

14].

The electron neutrino ν_e produces at its charged current interaction with matter a secondary electron. Through this interaction, a hadronic shower is created. A secondary high-energy electron radiates a photon via bremsstrahlung after a few meters of water/ice for a 10 TeV electron. This leads to an electromagnetic shower. Due to the small distance between the interaction point of the electron neutrino with matter and the creation point of the electromagnetic shower, the production points of both events can normally not be distinguished in a detector, which leads to a low pointing accuracy [19, 1, 2].

The NC interaction is independent of the flavour of the neutrino. As shown in figure 2.2 in schema (d), no secondary charged lepton is created by the interaction. So the NC interaction of a neutrino with matter produces a hadronic shower caused by the interaction process, and after the interaction, there is still a neutrino propagating. Therefore, the hadronic shower produces secondary particles in a NC interaction, which contains most dominantly pions, wherein kaons, protons or neutrons emerge in variable fractions. Since the outgoing neutrino always carries a fraction of the interaction energy unobserved away, the error of the reconstructed energy of the primary neutrino increases accordingly [1].

2.4 Neutrino Flux

Beyond the astrophysical processes discussed earlier, a diverse array of sources contributes to the production of neutrinos. The accompanying figure 2.3 illustrates the neutrino flux, providing a visual representation of the distribution of neutrinos originating from natural diffuse sources. Artificial sources engineered by humans, such as nuclear reactors and particle accelerators, play a crucial role in neutrino research. Reactors, designed primarily for nuclear power generation, emit antineutrinos as byproducts of the fission process. Particle accelerators, on the other hand, produce neutrinos through the collision of accelerated particles. Hereafter, natural neutrino sources are expounded.

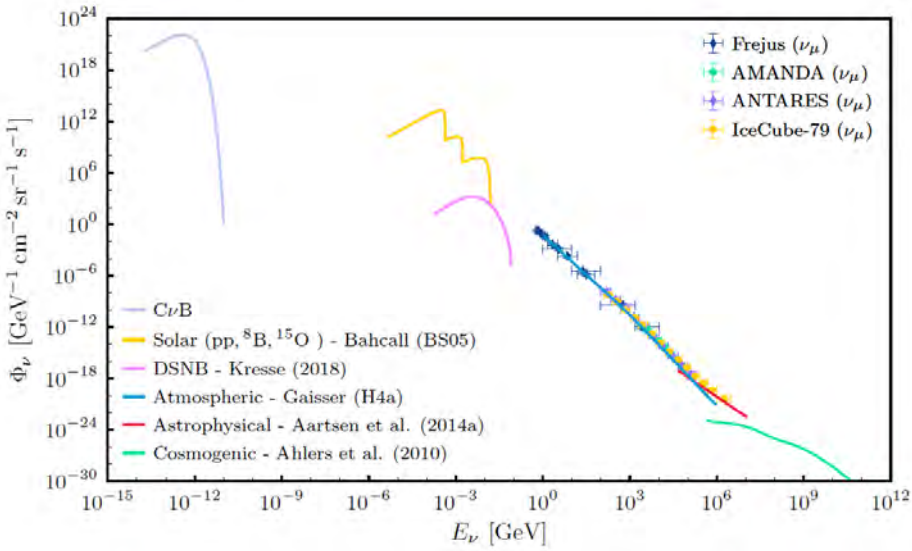

Fig. 2.3: Estimated neutrino flux origination from a variety of sources. For more information on the latter, refer to the text. Especial gratitude goes to F. Henningsen for providing the figure.

Cosmic Neutrino Background

The Cosmic Neutrino Background (CNB)) stands as a relic of the early universe, offering a unique window into the conditions prevailing shortly after the Big Bang. In the initial stages of the universe, during the epoch of neutrino decoupling approximately one second after the cosmic inception, neutrinos were in equilibrium with the primordial plasma [20, 21]. However, neutrinos decoupled from this plasma as the universe expanded and cooled, much like the CMB after 380,000 years [1, 2].

Unlike the CMB, the CNB has eluded direct detection due to the deficient energy of the neutrinos involved and is not detected directly up to date. Nevertheless, the CNB's indirect impact on the structures of the early universe provides a channel for observation. The relativistic propagation of cosmic neutrinos left a measurable imprint on the gravitational potentials of the evolving cosmos. One notable consequence is the influence of cosmic neutrinos on Baryonic Acoustic Oscillations, observable through the temperature power spectrum of the CMB. These oscillations, a product of the interplay between radiation and matter in the early universe, have been significantly affected by the nature of the cosmic neutrino background. By investigating these effects, researchers aim to indirectly get insights into the CNB, illuminating the conditions predominant during the epoch of neutrino decoupling [1]. The potential observation of the cosmic neutrino background holds the possibility of gaining a new understanding of the early universe, providing a complementary perspective to the extent of the information offered by the CMB.

Solar Neutrinos

Solar neutrinos, originating from the thermonuclear fusion processes within the sun's core, are predominantly produced through the CNO cycle or the pp chain. These neutrinos, primarily in the form of electron neutrinos with an energy around 1 MeV, are able to escape the sun almost unimpeded due to their weak interactions. This results in a substantial neutrino flux reaching Earth, approximately $6 \times 10^{10}\,\mathrm{cm}^{-2}\mathrm{s}^{-1}$ [1]. The observed solar neutrino flux raised questions as it did not align with the expected values based on solar models. This discrepancy, known as the solar neutrino problem, became a question in astrophysics. Given the known processes occurring in the sun's core, the measured flux was significantly lower than anticipated. The resolution to this problem came with the groundbreaking discovery of neutrino oscillation, which explains the measured flux of neutrinos on Earth [22, 23].

Terrestrial Neutrinos

Terrestrial neutrinos emerge due to beta decay within the Earth. These decays predominantly occur in the decay chains of terrestrial uranium and thorium, contributing to the generation of terrestrial neutrinos. The measurement and analysis of terrestrial neutrinos present an opportunity to get insights into the Earth's mantle composition. This information, in turn, enhances the understanding of the geological processes shaping the Earth's internal structure.

Atmospheric Neutrinos

When cosmic rays from space enter Earth's atmosphere, they undergo interactions with nuclei, giving rise to a cascade of secondary particles. Among these secondary particles, pions and, at higher energies, kaons play a significant role. The subsequent leptonic decays of these particles lead to the production of muons and neutrinos. Additionally, kaons can undergo semi-leptonic decays, yielding electron neutrinos and hadronic decays, generating more pions. As these particles travel through the atmosphere, in particular muons can decay before reaching the Earth's surface, producing electrons, electron neutrinos, and muon neutrinos. These neutrinos originating from cosmic-ray interactions in the atmosphere are collectively referred to as atmospheric neutrinos [1].

Atmospheric neutrinos constitute a substantial background source within neutrino detectors due to their prevalence in cosmic-ray-induced processes. Understanding the distribution and ratio between different neutrino flavours, especially at lower energies where most muons decay before reaching the ground, has been a crucial aspect of experimental neutrino research. The experimental verification of the expected flavour ratios, particularly at lower energies, proved challenging. This unexplained discrepancy paved the way for a significant discovery in neutrino physics, the observation of neutrino oscillation [22].

$$\pi^+ \to \mu^+ + \nu_\mu \qquad \pi^- \to \mu^- + \bar{\nu}_\mu \tag{2.10}$$

$$\hookrightarrow e^+ + \nu_e + \bar{\nu}_\mu \qquad \hookrightarrow e^- + \bar{\nu}_e + \nu_\mu \tag{2.11}$$

Cosmogenic Neutrinos

Cosmogenic neutrinos, a remarkable phenomenon in high-energy astrophysics, are produced when ultra-high-energy cosmic particles interact with photons from the CMB. This interaction gives rise to an interaction process involving a Δ^+ resonance. The subsequent decay of the Δ^+ resonance occurs through two possible channels, as depicted in the decay equations 2.12 below [2].

$$p + \gamma_{cmb} \rightarrow \Delta^+ \rightarrow n + \pi^+ \tag{2.12}$$

$$\rightarrow p + \pi^0 \tag{2.13}$$

In the first channel, the Δ^+ resonance decays into a neutron and a charged pion (π^+), opening up production channels for ultra-high energy neutrinos. The second channel involves the decay into a proton and a neutral pion (π^0) and results in a less energetic proton and neutral pion [2].

2.5 Astrophysical Sources of Neutrinos

Supernova Neutrinos

Supernova neutrinos arise from the cataclysmic termination of a star through a massive explosion known as a supernova. During a supernova, the stellar core undergoes compression due to gravitational pressure, leading to an explosion characterised by a luminous burst of photons and a massive outburst of neutrinos. The explosive phenomenon is initiated by the compression of the stellar core, where the rise of the electron Fermi energy enables the generation of neutrons and neutrinos from the interaction between electrons and protons [22, 12].

$$e^- + p \rightarrow n + \nu_e \tag{2.14}$$

Neutrinos, being solely weakly interacting, can escape the gravitational potential of the supernova core. This distinctive property makes them valuable probes for studying the internal processes and conditions during a supernova. One remarkable astrophysical observation of the last century provided crucial data on supernova neutrinos. The supernova SN1987A, which occurred in the Large Magellanic Cloud on 23 February 1987, yielded insights into the emission and properties of neutrinos during a stellar explosion. Beyond individual supernovae, the diffuse background radiation caused by isotropically distributed supernova neutrinos from distant supernovae across the universe contributes to our understanding of these cosmic phenomena [22, 12].

Pulsar Wind Nebulae

A Pulsar Wind Nebulae (PWN) is a Super Nova Remnant (SNR) powered by a pulsar in the centre. Pulsars are fast-rotating neutron stars with extremely high magnetic fields. The

extraordinary magnetic fields surrounding pulsars play a pivotal role in shaping the dynamics of the PWN. Charged particles, drawn into the pulsar's magnetic influence, undergo strong acceleration within these intense fields. This acceleration process generates ultra-high-energy cosmic rays. The high-energy cosmic rays produced by a PWN can, in turn, undergo decay through various processes, leading to the generation of high-energy astrophysical neutrinos as outlined in chapter 1.1 [24, 2].

Active Galactic Nuclei

Active Galactic Nuclei (AGN) are celestial phenomena situated at the heart of galaxies, standing out as highly luminous entities that surpass the radiance of the surrounding galaxy. The defining feature of an AGN is a supermassive black hole ensconced in the galactic centre, surrounded by an accretion disk, an accumulation of matter spiralling into the gravitational grasp of the black hole. As charged particles within the disk accelerate due to the intense gravitational forces, they generate a powerful electromagnetic field. This field concentrates the radiation emitted by the accelerated particles into a highly focused beam. The result spans a wide spectrum, ranging from radio emissions to high-energy gamma rays [7, 24].

Gamma Ray Bursts

While the exact origins of Gamma Ray Burst (GRB) are not fully understood, two distinct types have been identified: long GRBs, potentially stemming from the core collapse of massive stars with the formation of an accretion disk in the process of creating a black hole. Whereas short GRBs are believed to arise from more compact systems, such as the collision between a neutron star and a black hole. Both types of GRBs are accompanied by afterglow radiation, which persists longer than the initial burst itself. This afterglow can be detected across various wavelengths, providing valuable insights into the aftermath of these cataclysmic events. A particularly intriguing aspect of GRBs is their potential to produce high-energy cosmic rays through highly relativistic gas streams. These cosmic rays, once generated, can interact with photons from the CMB as introduced in chapter 2.3. This interaction gives rise to secondary particles, which, as part of a chain reaction, can ultimately decay into astrophysical neutrinos [1, 7, 24].

2.6 Neutrino Telescopes

Neutrino telescopes face unique challenges due to the low cross-section of neutrino interactions. To overcome this, large detector volumes to enhance the chances of measuring events are used. The detector medium must also be transparent, with a long attenuation length for the Cherenkov radiation. The attenuation length encompasses both scattering length and absorption length. In general, the Lambert-Beer law characterises the intensity of light over distance in a medium, with the intensity $I(r)$ governed by the equation:

$$I(r) = \frac{I_0}{4\pi r^2} \cdot exp\left[-r\left(\frac{1}{l_{abs}} + \frac{1}{l_{scat}}\right)\right] \tag{2.15}$$

Here, l_{abs} and l_{scat} represent absorption and scattering lengths, respectively. The attenuation length l_{att} denotes the average path length, after which $1/e$ of the initial intensity remains, combining both effects.

$$l_{att} = \left(\frac{1}{l_{abs}} + \frac{1}{l_{scat}}\right)^{-1} \tag{2.16}$$

Absorbed photons cease to exist, transferring their energy to the medium, while scattered photons change direction. In water and ice, scattering predominantly occurs in the forward direction, indicating a preference for photons to maintain their trajectory rather than deviate significantly from their original path. Between water and ice, differences in the interplay between absorption and scattering are observed. In water, the absorption length takes precedence, signifying that photons are more likely to be absorbed than scattered. In contrast, scattering is more influential in ice, with photons exhibiting a higher probability of changing direction rather than being absorbed.

The following table 1 provides a comprehensive overview of the different attenuation lengths, absorption lengths, and effective scattering lengths for various locations housing current and planned neutrino telescopes. The effective scattering length is used to take different distributions depeding on the scattering angle into account. It is to be mentioned that, especially for ocean water, the attenuation length can vary significantly depending on depth and location in the ocean [14, 25].

Site	$l_{abs}(m)$	l_{scat}^{eff} (m)	l_{att} (m)
Lake Baikal, 1 km depth	18-22	150-250	16-20
Ocean, > 1.5 km depth	40-70	200-300	33-56
Polar ice, 1.5-2.0 km depth	∼95	∼20	∼16
Polar ice, 2.2-2.5 km depth	> 100	30-40	>25

Tab. 1: Approximate absorption and effective scattering lengths with resulting attenuation length for different locations of neutrino telescopes. Lengths stated in water are subject to seasonal change and may differ strongly depending on location and ocean. Absorption and scattering lengths taken from [14].

The precise knowledge of the attenuation length of the medium inside a neutrino telescope is mandatory for reconstruction efforts of neutrino events. Hence, the spacing of optical modules must be within the attenuation length to ensure signal quality. Similarly, the angular resolution depends on the spacing between the optical modules, as the scattering influences the time distribution of incoming photons.

As the event rate of neutrino interaction inside the instrumented volume of the detector is relatively low, it is essential to minimise the background. Therefore, shielding the neutrino

telescope from secondary particles like atmospheric muons and neutrinos is necessary. This is achieved by locating the detectors deep in the ice or water to reduce the atmospheric background. An additional method is to use the detector as a down-looking telescope. By doing so, the Earth is used as a shield against the background, meaning that events coming from the upside are not counted as possible neutrino events. The downside of this approach is that high-energy neutrinos are shielded by the Earth as the interaction cross-section of neutrinos increases with increasing energy. Another technique of mitigating the background is introducing a veto region in the upper layers of the detector. Hence, events coming from the top and originating outside the instrumented volume of the detector can be identified and thus ignored for the analysis of neutrino events. Both factors, the opaqueness of the Earth for high-energy neutrinos and the atmospheric neutrino veto, limit the sensitivity of the neutrino telescope to astrophysical high-energy neutrinos to 20-30 degrees around the horizon of the detector [1, 2, 6].

In addition to the background sources already discussed, there are additional background sources within the detector. One such source is ^{40}K, a naturally occurring isotope undergoing β^--decay within water. The beta decay process generates a 1.4 MeV electron capable of producing Cherenkov light. Additionally, the direct capture of an electron by ^{40}K results in the emission of a photon, which, through Compton scattering, can produce an energetic electron, leading to the generation of Cherenkov light [26].

Another intrinsic source of background for water-based detectors stems from the world of deep-sea organisms. Bioluminescence, triggered by several processes, as currents around the optical module or contact with it, becomes a source of photons within the range of 440nm to 500nm, closely resembling Cherenkov radiation [26, 27].

These background processes produce light signals with longer timescales compared to neutrino signals. To effectively eliminate such background interference, a strategic approach involves the application of coincidence triggers. By requiring the simultaneous detection of a signal at multiple locations within the detector and correlating these detections within a nanosecond time window, the background signals can be distinguished from possible neutrino interactions [28].

An introduction to current and future neutrino telescopes is given in the following.

IceCube

Situated at the Amundsen-Scott South Pole Station, the IceCube detector utilises glacial ice as its detection medium. Spanning an instrumented volume of approximately one cubic kilometre, the detector features a configuration of 5160 Digital Optical Modules (DOMs) distributed across 86 strings. In each DOM a 10” Photomultiplier Tube (PMT) is located, looking downwards. The strings are deployed at depths ranging from 1450 to 2450 meters beneath the surface [29]. Within the IceCube framework, the DeepCore sub-array specifically targets low-energy neutrinos, particularly those around 100 GeV. Comprising 8 strings equipped with 60 more closely spaced DOMs, the DeepCore array enhances sensitivity to neutrino interactions at lower energy levels.

Complementing the detection capabilities of IceCube is IceTop at the surface, a component

consisting of 162 ice-filled tanks, each equipped with DOMs. IceTop primarily serves as a veto system for down-going muons, contributing to the overall detector's precision. Additionally, IceTop facilitates studies related to PeV gamma rays and explores the radiation effects of solar flares. Also at the surface is the IceCube Laboratory, which hosts server rooms, data acquisition and online filtering computers [29, 6].

KM3NeT

KM3NeT [30], a research infrastructure currently in construction, is being deployed in the deep Mediterranean Sea with sites located offshore Toulon in France and Portopalo di Capo Passero in Sicily. This initiative results in establishing a network comprising two neutrino detectors, integrating insights gained from predecessor experiments such as NESTOR [31], NEMO [32], and ANTARES [33], all conducted in the Mediteranean Sea. In contrast to IceCube's single-PMT approach, KM3NeT adopts a multi-PMT strategy, employing 31 three-inch PMTs per module, uniformly oriented outward. Each module is encapsulated within a 17" diameter glass sphere featuring a cable breakout at the top. The PMTs are encircled by a metallic reflector, referred to as the light collection rings, enhancing their photon capture area [34]. For precise calibration, acoustic emitters and receivers are integrated into each module, enabling distance measurements between individual DOMs. Compasses and accelerometers in each DOM also provide supplementary calibration data related to ocean currents [34].

Upon completion, KM3NeT will consist of two distinct detector arrays: ARCA (Astroparticle Research with Cosmics in the Abyss) and ORCA (Oscillation Research with Cosmics in the Abyss), each located at its respective site [35]. ARCA comprises 230 lines, or detection units, with 18 DOMs per line, spanning a length of 700 meters. As of September 2022, 21 lines were operational and transmitting data to shore [36]. The ARCA detection units are placed in two clusters, each approximately 500 meters in radius, targeting the search for highly energetic neutrinos, particularly those from the galactic plane [30]. On the other hand, ORCA employs the same detection units as ARCA but with 115 units distributed in a 100-meter radius, enhancing the detector's efficiency for energies in the GeV range. The primary objective of ORCA is the study of fundamental neutrino properties, including neutrino oscillations and determining the neutrino mass hierarchy. Currently, 8 ORCA detection units are operational [37].

Baikal-GVD

Nestled in Lake Baikal in Russia, approximately 1 km beneath the surface, is the Baikal Gigaton Volume Detector (Baikal-GVD). This neutrino telescope is being constructed in a clustered configuration, featuring 8 strings per cluster and 36 optical modules per string. The strings are positioned with a separation of 60 meters, and the clusters are spaced 300 meters apart [38, 39]. As of April 2022, ten such clusters have been successfully deployed and are operational. Future plans outline the deployment of a total of 16–18 clusters by 2025–2026, resulting in a detector volume exceeding 1 km^3 [38].

PLEνM

As already mentioned above in this chapter, neutrino telescopes are most sensitive to high-energy astrophysical neutrinos around their horizontal plane. This is caused by the shielding effect of the Earth for high-energy neutrinos and the high background rate of atmospheric muons and neutrinos coming from the top. In order to cover the whole sky for possible point source identification, the field of view of multiple neutrino telescopes needs to be combined [40]. Figure 2.4 illustrates the Earth with the most responsive zones of existing and prospective neutrino telescopes, accentuating a significantly expanded collective sensitivity region. Proposals for a worldwide neutrino monitoring initiative have been advanced through PLEνM [41], outlining how collaborative endeavours involving IceCube, KM3NeT, Baikal-GVD, and Pacific Ocean Neutrino Expermient (P-ONE) could enhance discovery capabilities in the northern hemisphere by up to a magnitude three times greater than that achievable by IceCube alone [41]. The latter neutrino telescope P-ONE is currently under development. A more detailed introduction and description of this new neutrino telescope is given in chapter 3.

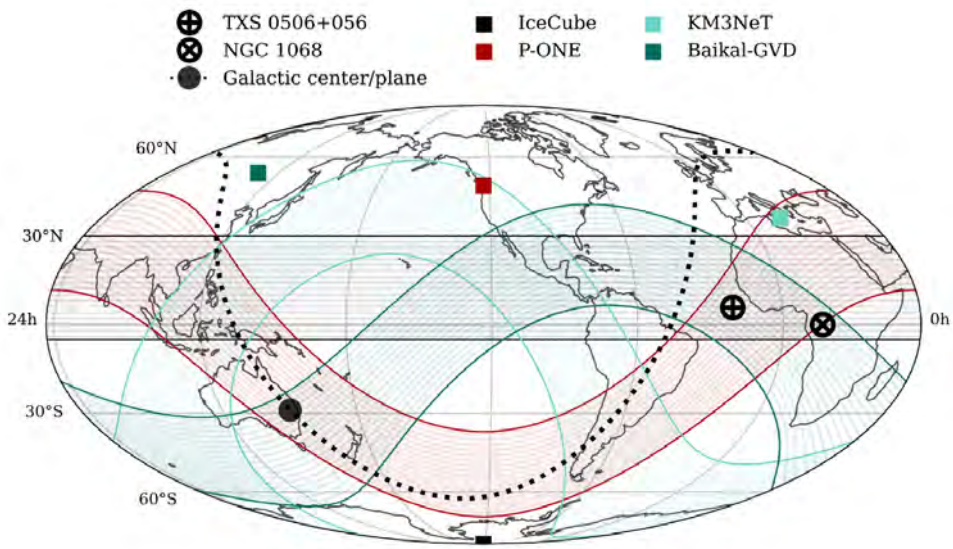

Fig. 2.4: Locations of neutrino telescopes included in PLEνM and their respective region of highest sensitivity projected on Earth. Projections of the galactic center and plane and two neutrino point sources discovered by IceCube are also pictured. Figure provided by L. Schumacher [40].

3 Pacific Ocean Neutrino Experiment (P-ONE)

The Pacific Ocean Neutrino Experiment [42] is a planned multi-cubic kilometre neutrino telescope at the Cascadia Basin, 200 km offshore Vancouver Island in the North-East Pacific. Situated at a depth of 2660 meters, the site experiences currents ranging from 3 to 7 cm/s [42], with a stable temperature around 2°C [43]. This future detector will be connected to the North East Pacific Time-series Underwater Networked Experiments (NEPTUNE) [44] observatory operated by Ocean Networks Canada (ONC). The P-ONE currently features around 70 strings, each equipped with 20 modules, although the final geometry is still undergoing optimisation [45]. Figure 3.1 shows a possible layout of the final detector. Currently, in development and construction, the first functional line, P-ONE-1, is developed to serve as a blueprint for future detector lines. The deployment of P-ONE-1 is scheduled for 2025. A detailed introduction and technical overview of P-ONE-1 is given in Chapter 3.2.

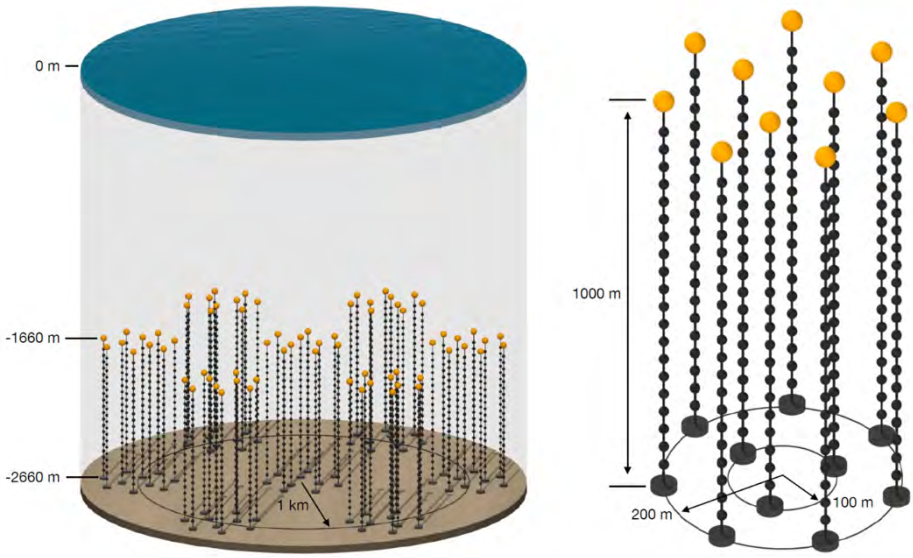

Fig. 3.1: The preliminary P-ONE detector design with the full 7 clusters (left) and one individual cluster consisting of 10 strings (right). Strings will consist of 20 modules each at a total length of one kilometre. Geometry optimisation for the entire detector is currently still ongoing [46, 40]. Figure designed by K. Holzapfel.

3.1 Pathfinder Missions

Two successful pathfinder missions, STRAW-a [47] and STRAW-b [48], were deployed at the Cascadia Basin in 2018 and 2020, respectively, and both were successfully recovered in 2023.

The STRings for Absorption length in Water (STRAW) pathfinder consist of two 120-meter

tall mooring lines, instrumented with three Precision Optical CAlibration Modules (POCAM) serving as light emitter modules and five STRAW Digital Optical Modules (sDOM) functioning as light sensor modules. The primary objective of this mission was to precisely measure light attenuation across various wavelengths (350 to 600 nm) and monitor bioluminescence and ^{40}K background at the site in Cascadia Basin. The mooring lines have been positioned such, that distances of 20 to 90 meters between emitters and sensors were covered, wherein the two strings are spaced 37 m between each other [47, 6, 19]. The results of the attenuation lengths are shown in the following figure 3.2 [26].

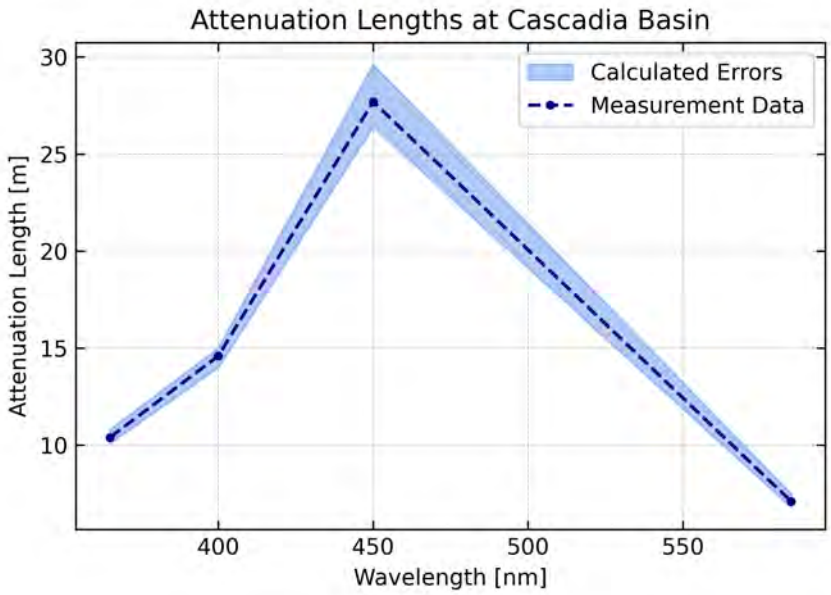

Fig. 3.2: Result for the attenuation lengths of the STRAW-a pathfinder mission at Cascadia Basin [26].

The STRAW-b pathfinder was deployed in 2020 at Cascadia Basin around 40 meters east of the position of STRAW, aiming to validate and build upon the results obtained by its predecessor. STRAW-b consists of a 450-meter-long mooring line, housing ten modules within a robust 13-inch high-pressure resistant glass sphere [48, 6].

Among these modules, two Light Detection and Ranging (LiDAR) modules are incorporated to measure scattering length precisely, providing valuable insights into the optical properties of the site. Also, a muon tracker module is integrated into STRAW-b, specifically designed to measure atmospheric muon rates, a significant source of background noise in neutrino telescopes. Additionally, two Photomultiplier Tube (PMT) spectrometer modules are dedicated to capture the spectrum of bioluminescent light, enhancing the accuracy of background analysis. A mini spectrometer module is tailored to measure high-intensity bursts of bioluminescence. Furthermore, a Wavelength Shifting Module (WOM), developed by the University of Mainz, is optimised

to measure UV photons. The remaining three modules were standard units, which built the base for the before-mentioned modules. The standard units are equipped to measure internal pressure, temperature, and humidity and also host magnetic field sensors and accelerometers [6, 48].

STRAW-a and STRAW-b were successfully recovered in July 2023. Further data analysis remains, promising further insights into the underwater environment and contributing to advancements in the development of P-ONE [48].

3.2 P-ONE-1

The first functional line of the P-ONE detector is currently under development. This line should serve as a blueprint for the following lines. Thus, it is designed for modularity and scalability. The line will be about 1000 m long, with 20 modules distributed evenly over the length. Of these 20 modules, three modules will be calibration modules; the remaining modules will be optical modules. Each module has a housing consisting of two glass hemispheres with a titanium termination assembly in the centre. The glass hemispheres are 17" in diameter and made of borosilicate. They come with a titanium flange glued to it and are produced by Nautilus. With the flange, the hemisphere can be mounted to the termination assembly. The modules are connected with an integrated backbone cable. This cable also terminates at a mooring junction box (mJB), acting as an interface to the NEPTUNE network of ONC. The line is held on the ground by the so-called deployment frame, which serves as an anchor, the line is straightened up by a subsea float mounted at the top part of the line. The backbone cable combines a load-bearing aramid braid with a hybrid electro-optical power and communication cable. A titanium termination provides the connection between the backbone cable and the module can, in which the necessary number of copper and optical strands are branched out and connected to the module. The rest of the wires are fed through to the next module. Even in the case of a failure of one module, the sealing system allows for maintaining a functioning system. So, no water can reach other modules through the backbone cable. Due to this cable-integrating approach, there is no shadow in the field of view of the PMTs. The before-mentioned deployment frame stores the whole detector line, as the line is furled up, allowing access to the individual modules and instruments; after deployment, it serves as an anchor [49].

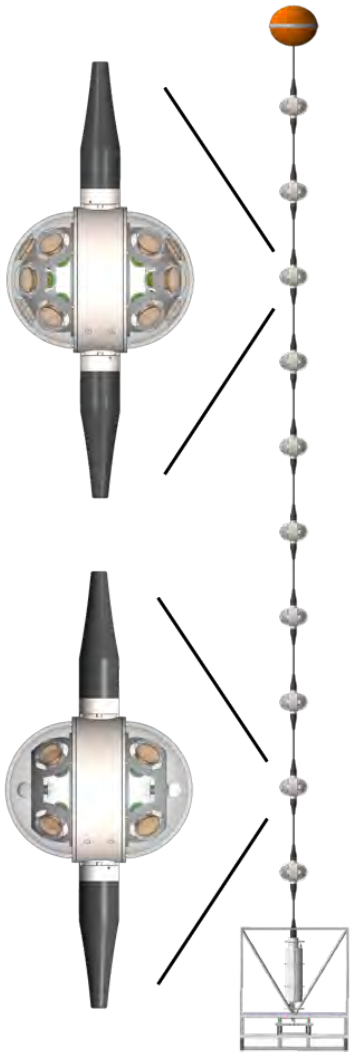

Fig. 3.3: Conceptional drawing of the P-ONE-1 line. Images provided by C. Spannfellner, according to [49].

With this design, P-ONE-1 provides a one-kilometre-high infrastructure in the deep sea, developed to last over 15 years at its position and providing a constant data stream to onshore. These benchmarking parameters empower this line and all upcoming future lines of P-ONE as a great basis for oceanographic research. Hence in chapter 7 the development of an oceanography sensor interface for P-ONE is described. Additionally, the theoretical background of oceanography is introduced in chapter 5. In chapter 6 conducted measurements for characterising Cascadia Basin are elucidated.

As already introduced, the P-ONE-1 line will host two different types of modules: the calibration module (P-CAL) and the optical module (P-OM). The P-OM will be described in detail in chapter 4.1. First, the general calibration system of the P-ONE-1 line and the P-CAL will be discussed in the following [49]. The P-ONE-1 calibration is based on two different calibration methods, the acoustic and the optical calibration. For the geometric and timing calibration, seafloor-based hydrophones will emit signals, which are then captured by acoustic receivers coupled to the glass spheres of every module. Additional geometrical, optical and timing calibration can be achieved by using directional flasher beacons in every module. The flasher beacons emit light, which then can be detected by PMTs of other neighbouring modules [50, 51]. Optical calibration is provided by the P-CAL. This module is equipped with isotropic, high-power, nanosecond light pulsers, flashing in wavelengths between 300 and 600 nm. This self-monitoring system is based on the POCAM for the IceCube experiment. In general, the design of the P-CAL is similar to the P-OM, wherein one row of PMTs is replaced by the calibration system consisting of the light pulsers and a PTFE diffuser to ensure isotropy of the emitted light. The diffuser is coupled to the glass hemisphere by optical gel. Additionally, the P-CAL holds a camera pointing upwards to study potential biofouling and bioluminescence events on and close by the modules [51, 52].

4 P-ONE Optical Module

4.1 Conceptional Design

The optical module (P-OM) housing for P-ONE-1 is the standard housing introduced in chapter 3.2. Inside each glass hemisphere, there is a mounting frame, which is screwed to the titanium flange of the hemisphere. The frame is designed to hold all devices inside the hemisphere at their designated position. Each hemisphere houses 8 PMTs with a 3.1" diameter of the type R14374-10 produced by Hamamatsu. Figure 4.1 shows a conceptional drawing of the P-OM. The PMTs are mounted via a spring-load mechanism to accommodate temperature gradients, hydrostatic compression and shock and vibrational loads during the transportation and deployment. Additionally, the PMTs are coupled optical via silicon-based optical gel pads. This increases the effective photocathode area by utilising total internal reflection at the lateral surface of the gel pad. Another advantage of using gel pads for optical coupling is the ability to detect photons with low incident angles missing the primary PMT with an adjacent PMT. Furthermore, this mounting scheme with the easily removable gel pads offers the possibility to swap PMTs during production and testing, wherein the processes of production and testing of the gel pads and PMTs are discussed in the following chapters 4.2 and 4.3 [49, 40].

Fig. 4.1: Conceptional drawing of the P-OM. Image provided by C. Spannfellner, according to [49].

The PMTs are supplied with high voltage by the so-called μBase, which was developed from the IceCube Upgrade and offers a versatile low-power high voltage supply for the PMTs [53]. Also, a digital module in Geant4 was developed by using the construction files of the module. This was used for simulation, allowing investigations of the optics of the instruments, attributions of optical effects and design optimisation [40]. As shown in figure 3.3 additional spaces are available in the frame between the PMTs, which are used for other devices for calibration purposes, such as the flasher beacons, axicons for light collimation and acoustic receivers. Also, the oceanographic sensor interface can be placed at this spot, which will be introduced in chapter 7. Additionally, readout and communication electronics must be placed in the module. In each hemisphere, an Interposer Board is located and connected to the module's mainboard, which will be located in one hemisphere per module. The Interposer Board manages communication to the μBases and the other devices mentioned before. Moreover, one Silicon Muon Tracker (SMUT) is placed inside each P-OM, located at the mainboard's position in the module's other hemisphere. The mainboard and the SMUT are placed in the centre of the hemisphere parallel to the plane of the titanium flange of the hemisphere [49, 40].

4.2 PMTs and μBase

PMTs are high-sensitive detectors for weak light signals ranging from near-infrared to near-ultraviolet spectrum. They are designed to convert incoming photons to an electrical signal using the photo-electric effect and, subsequently, multiplication of the excited electrons. Therefore, they are very well suited for detecting Cherenkov radiation and thus for the operation inside neutrino detectors. In figure 4.2 the schematic structure of a PMT is shown.

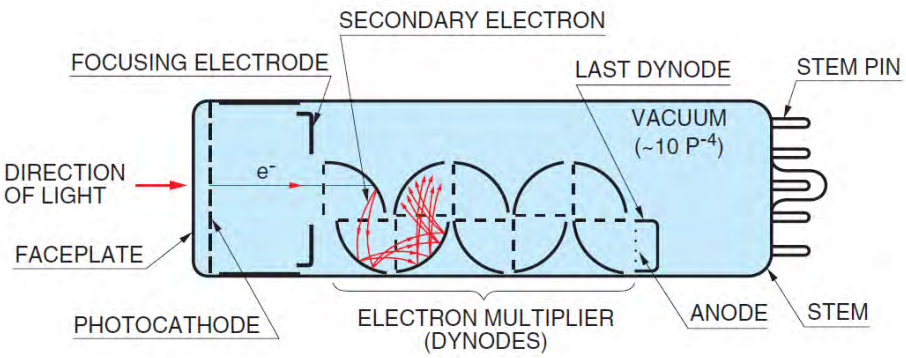

Fig. 4.2: Schematic structure of a PMT. A photon is absorbed in the photocathode, and the subsequent excited electron is multiplicated in the dynode setup [40]. Figure from [54].

The incoming photon excites an electron in the photocathode from the valence band to the conduction band through the photoelectric effect. This excited electron must then overcome the energy barrier to reach the PMT's vacuum chamber. After the excited electron is out of the photocathode, the electron is accelerated towards the first dynode by the electric field of the focusing electrode. After passing the focusing electrode, the electron enters the dynode structure, in which secondary electrons are produced by a multiplication process. Therefore, the dynodes are covered by a secondary emissive surface, and after an impact of an electron on the surface, a number of secondary electrons are released. The dynode structure contains several stages of multiplication of the signal, and after passing the structure, a high number of electrons reaches the anode, and a readable signal is caused. The parameter of the quantum efficiency of a PMT strongly depends on the wavelength of the incoming light and the material parameter of the photocathode. For P-ONE-1, the selected PMT is the R14374 from Hamamatsu, which has a bialkali photocathode with a spectral response of 300 to 650 nm [40].

The time of travel for electrons in the dynode structure underlies fluctuations depending on the position of the initial photons. For multiple detections, there is a spread over the travel time of the charge deposited at the anode, which causes a characteristic distribution of the signal. The transit time is defined as the time between the laser trigger and the peak of the waveform. The transit time spread (TTS) is the width of a distribution of transit times. PMTs have exceptionally fast transit times in the order of few nanoseconds, depending on the dynode structure, their type and the supply voltage. The TTS is in case of the PMTs used for P-ONE-1

around 1.5 ns. The PMT needs high voltage for the dynode system to establish a high electric field to accelerate and direct the electrons. This required voltage is provided by the μBase for P-ONE-1. The μBase was initially developed by C. Wendt for the Hamamatsu R15458-02 used in the IceCube Update experiment [53]. The selection of the μBase was considered early in the design process and the compatibility of the μBase with the R14374 PMT used in P-ONE-1 was proven by tests in the Optical Module Calibration Unit (OMCU) setup by N. Retza [40] and an additional measurement at the testing facility at the RWTH Aachen [55].

During discussions with the development team of KM3NeT and investigations performed by V. Gously-Leblanc, it was found out that for the usage of negative voltage for PMTs, there is a risk of accumulating electrons on the surface of the PMT. These electrons could be attracted to the glass bulb of the PMT and create electronic noise or potentially produce scintillation light. It is also suggested that if metal parts around the photocathode are grounded, the conductivity of the glass will generate a small current between the ground and the cathode [56, 57, 58]. These effects could potentially damage the photocathode and the PMT themselves. Hamamatsu recommends using formal HA coating which is black conductive paint connected to the cathode with an insulated material surrounding it for safety [54]. As the PMTs for P-ONE-1 were ordered and received without any coating applied to them, the decision was made to coat 380 PMTs retrospectively. For this purpose, it was decided to coat the PMTs with Plastic 70 Super [59], wherein the liquid was diluted with the according Thinner [60] in a 1:1 ratio. The Plastic 70 Super was selected based on the experiences made with this product by the KM3NeT experiment. The KM3NeT collaboration was able to correct problems that occurred in the context of uncoated PMTs thus resulting in high dark rate measurements by using this insulating coating. In measurements conducted for P-ONE-1, it was not possible to observe a negative impact of not-coated PMTs on the dark rate. Nevertheless, as most other large-scale neutrino telescopes, such as IceCube and KM3NeT, used coated PMTs, the decision was made to coat the PMTs for P-ONE-1 as well. The detailed procedure of the coating process is shown in the appendix in section A.1. The goal was to apply the coating homogenously from the upper part of the neck to the bottom of the PMT. This was done by dipping the entire PMT into the coating and holding it at the edge of the photocathode. After the coating was cured, the pins of the PMT needed to be cleaned to avoid any problems during the soldering

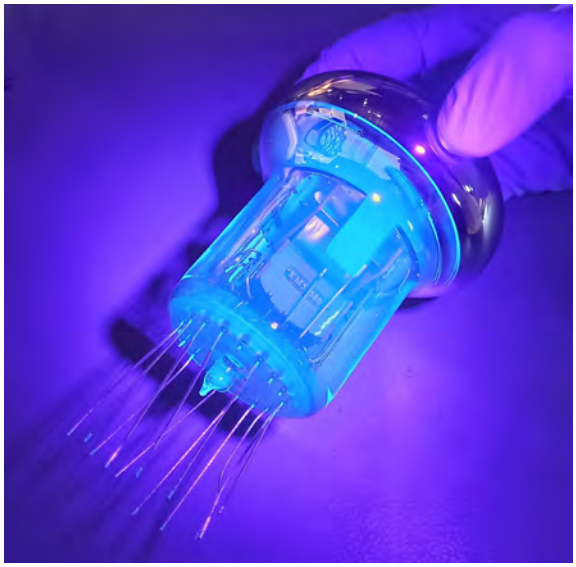

Fig. 4.3: Picture of a coated PMT under UV-light. The coating is fluorescent under UV light and, hence, glows blue. The photocathode and the pins of the PMT are free of coating, the rest is covered homogenously.

of the μBase to the PMT. This was performed by dipping the pins into the thinner. After this process, a quality test was performed to guarantee the complete coating of the PMT without covering the photocathode or the pins. A coated PMT is pictured in figure 4.3. It is visible that the coating is fluorescent to UV light and glows blue here. It is also apparent that the photocathode and the pins are coating-free.

After the coating was applied to all 380 PMTs and they all passed the quality control, the PMTs and the μBases were soldered together. Past the soldering process, all attached μBases were cleaned to remove any remnants of soldering flux on the PCB. In the following, the PMTs and μBases were ready for baseline testing to ensure everything worked as expected. The testing setup at the RWTH Aachen was used to perform these tests. The setup is capable of testing 88 PMTs simultaneously per day at temperatures down to $-20\,°\mathrm{C}$ [55]. Hence, it was possible to test all PMTs for P-ONE-1 within one week at $3\,°\mathrm{C}$, which is the expected operating temperature of the PMTs in the deep sea.

Characterisation Test in Aachen for P-ONE-1

The testing setup in Aachen is based on a modified refrigerator container, which can hold a temperature from -40 to $25\,°\mathrm{C}$. The room in the container is completely light and airtight to guarantee good measurement results and avoid problems during data taking at low temperatures. Inside the room, a rack carries eight slide-in bars, each holding 12 PMTs. Thus, 96 PMTs can be arranged inside the setup, of which 4 channels are used for triggering and 4 channels are used for reference PMTs. The PMTs can be mounted to the slide-in outside the room and the positions of the PMTs are marked with unique barcodes, enabling direct association of the PMT serial number and the readout channel in the database. Each PMT is connected to one of four mDOM mainboards of the IceCube Upgrade experiment. Each mainboard controls and reads out 24 PMTs. All the measurements are then stored in a local database at the RWTH Aachen [55].

Over five days of testing at the setup, it was possible to test 373 PMTs at $3\,°\mathrm{C}$. During the tests, measurements of the SPE spectrum, including a gain calibration, peak-to-valley measurement and a spe resolution, the dark rate, the TTS and the photon detection efficiency, were performed for all PMTs. The data are currently stored at the RWTH Aachen as well as at the TUM. The measurements were conducted to verify the requirements set for the PMTs for P-ONE-1 which are listed in table 2.

High Voltage for μBase	950 to 1350 V
Quantum Efficiency Measurement	$> 26\%$ for $\lambda = 400\,\mathrm{nm}$
Transit Time Spread	$< 2\,\mathrm{ns}$
SPE Peak to Valley ratio	> 2
Dark Rate	not defined

Tab. 2: List of requirements for the PMTs of P-ONE-1.

As the measurements were conducted shortly before finishing this thesis, the analysis of the

data is still running and not completed yet. The evaluation and analysis of the data is mainly performed by V. Gousy-Leblanc based on analysis scripts developed by L. Halve. In the following section, the conducted measurements are introduced.

SPE Spectrum

By measuring the single photo-electron (SPE) spectrum of a PMT several characteristic parameters can be tested. The SPE spectrum is composed of the superposition of multiple peaks. The first peak at 0 pC represents all undetected photons, which means that the light source emitted a light pulse, but the PMT did not detect it. The second peak features the event of one electron getting emitted per light emission, giving the spectrum its name: single photo-electron. The other peaks with higher charges represent the emission of more electrons per emitted light signal, caused by more photons hitting the photocathode. By performing SPE spectrum measurements for different high-voltages, a gain calibration can be performed. This needs to be done for each measurement with different environmental parameters. Gain calibration means, that the amplification of the signal of the PMT is set to a pre-selected value. For all measurements the gain was set to the value of 5×10^6, resulting in a charge of around 0.8 pC for the single photo-electron peak. To achieve this gain the high-voltage at each μBase needs to be adjusted in the correct way.Additionally, the SPE spectrum gives the peak-to-valley ratio, which characterises the capability to distinguish a signal from the background. The higher the ratio, the better the distinction can be made.

Transit Time

Precise timing in neutrino telescopes is vital for the reconstruction of events.. Therefore an arrival time measurement was conducted. For P-ONE-1, the relative timing is of interest. Thus, not the absolute arrival times are relevant, but the transit time spread (TTS). The TTS is the FWHM of the main peak of the arrival time spectrum. In the conducted measurements two different TTS are given, one uncorrected and one corrected one. Hereby, the corrected one considers the light source's distribution and the data acquisition system. In arrival time measurements also late pulses are detected, which can be explained by scattering effects in the dynode system of the PMT resulting in delayed signals.

Dark Rate

Another characteristic parameter of PMTs is the so-called dark rate. The dark rate can be caused by the photocathode's thermionic emission, resulting in an emitted signal even though there was no photon from a light source. Hence, the dark rate is one contributor to the background signal in a neutrino telescope. In these tests, the dark rate was measured by setting up the discriminator and counting how many events were seen over the measurement time of one hour. For these measurements, the events were counted over 10 seconds, and a rate was calculated for this period. Between each period, there is a dead time of 100 ns.

Effect of Uncoated PMTs

During one measurement run, an unexpected behaviour in the dark rate of some PMTs was observed. The results of the mean dark rate as well as the standard deviation of it are shown in figure 4.4. It is apparent that some of the PMTs show very high dark rates, wherein the positions of the PMTs don't show any logical pattern. It was recognised that during this measurement run, two PMTs were tested, which are not coated. These PMTs are marked with a blue ellipse.

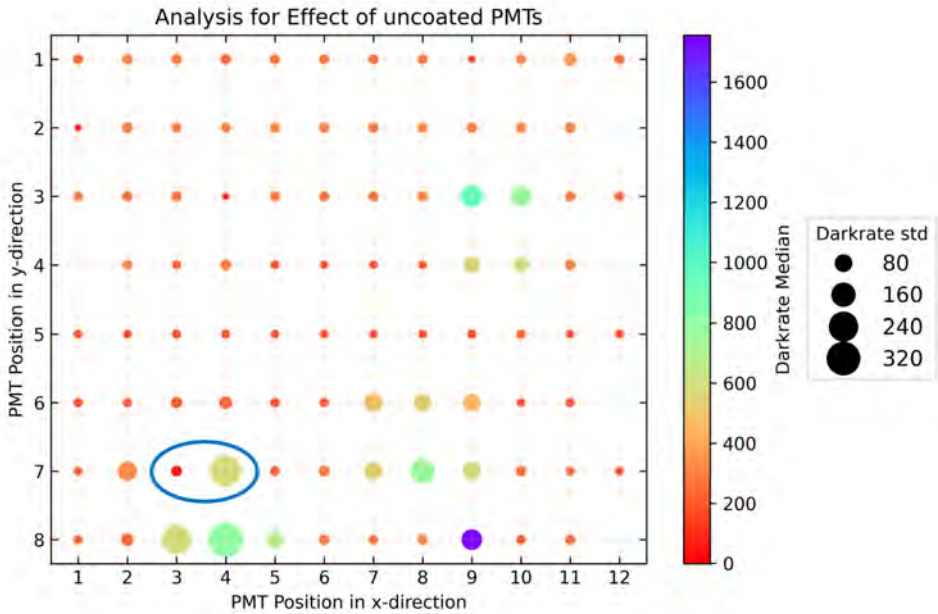

Fig. 4.4: Dark rate median and its standard deviation plotted against the position of the PMTs in the setup.

In order to get applicable data for the PMTs with high dark rates they were retested in a second measurement run in which the uncoated PMTs were not included. The comparison of the results of both measurement are shown in figure 4.5. Here the first run and the second run are compared regarding the median dark rate and its standard deviation. It is apparent that for most of the PMTs the dark rate and standard deviation are in a normal regime for the second run. For the PMT with sample number 12 the median dark rate does not reduce. The PMT has the serial number P-ONE-1_KM55842_291 and had also at measurement conducted by Hamamatsu a high dark rate of 930 Hz. For the rest of the retested PMTs a significant drop regarding the median dark rate could be observed [56, 57, 58]. This leads to the assumption that the uncoated PMTs could have an effect on other PMTs resulting in a higher dark rate for the affected PMTs. As the testing time at the RWTH Aachen was limited further investigation regarding this deviation could not be conducted. Still, it can be stated that the decision to coat the PMTs for P-ONE-1 had no negative effects on the PMTs during the characterisation tests and may avoid negative impacts among the PMTs themselves.

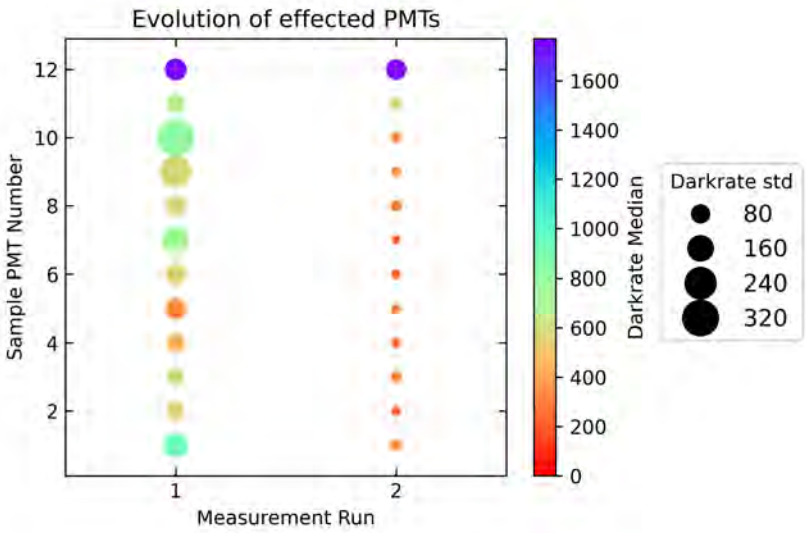

Fig. 4.5: Comparison of the median dark rate and its standard deviation of the effected PMTs. For run 1, uncoated PMTs were in the setup, whereas in run 2, all tested PMTs were coated.

Outlook

The measurement needs to be analysed and, accordingly, the PMTs characterised. So far, it seems that all PMTs have met the set requirements. Based on the results the favored PMTs can be selected and used for P-ONE-1.

4.3 Production of the Optical Module

Parallel to the testing and characterisation of the PMTs, the production of the P-OM was planned and prepared. The main focus of the production of the P-OM lies so far on the production of the gel pads of the PMTs and the integration of the PMTs with gel pad into the hemisphere of the module. In the following, the method of gel pad production is introduced, and afterwards, the technique of integration of the PMTs into the hemisphere. Subsequently, the possibilities of scaling this production up to match the requirements for P-ONE-1 are illustrated, as well as a quality control plan to ensure consistent results of good quality.

To be able to produce the hemispheres of the P-OM in a clean and controlled environment, a clean tent was ordered and constructed in a lab at the Technical University Munich (TUM) [40]. Additional equipment for the gel pad production and integration was ordered and arranged inside the clean tent [61]. Hereby two areas in the clean tent have been defined, one for the gel pad production on one side of the tent. On the opposite side, tables were constructed to host the hemispheres for the integration process, as shown in figures 4.6 and 4.7.

Fig. 4.6: Picture of the gel pad production site in the clean tent.

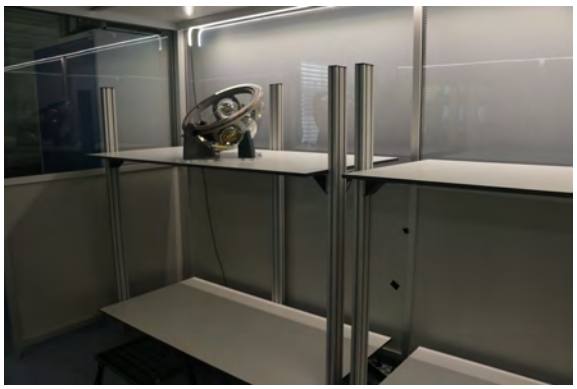

Fig. 4.7: Picture of the self-constructed tables for the integration of the hemisphere of the P-OM.

Gel Pad Production

Good optical coupling between the glass of the hemisphere and the PMTs is crucial for a high detection efficiency. Thus, gel pads are used to couple the PMTs to the hemisphere. The gel has a refractive index similar to the glass, and hence incoming photons experience a smooth transition between the glass and the gel pad, respectively the PMT. For the gel pad, a two-component gel from Wacker is used. The optimal consistency of the gel pads is reached at a mixing ratio of 3:2 of the constituents Silgel 612 A and Silgel 612 B. The gel pad gets formed and attached to the PMT by using a mold, which is designed for this purpose. A detailed procedure for the gel pad production is elucidated next.

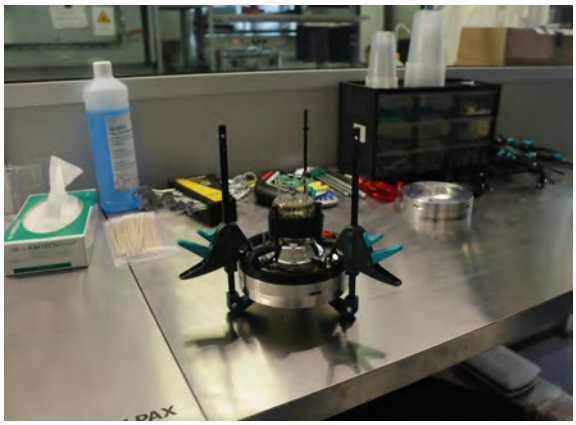

Fig. 4.8: Picture of an assembled mold. The PMT is fixed in position by taping the neck of the PMT to the alignment tool on the mold. The clamps press the upper and lower part of the mold together.

In the first step, coating gel needs to be produced. This coating gel is used to coat the part of the molds, which are later in contact with the gel pad. This ensures a good removal of the gel pad out of the mold without damaging the gel pad or the PMT. The coating gel is composed of Elastosil 601A and Elastosil 601B from Wacker in a mixing ratio of 9:1. Per mold, a volume of less than 10 g of the coating gel is needed. After mixing the components and applying the coating gel onto the mold, in the next step the main optical gel for the gel pad has to be prepared. As already introduced above, the

main optical gel is made of Silgel 612 from Wacker, wherein the variants A and B are mixed in a ratio of 3:2. For one gel pad, a minimum mass of 70 g of main optical gel is needed. After the main optical gel components are mixed, it needs to be degassed to get a bubble-free gel pad. Next, the PMT gets aligned in the mold with the aid of a developed alignment tool and a distance ring. When the PMT is in the correct position it gets fixed by using tape. Afterwards, the mold gets assembled, meaning that the upper part of the mold and the lower part of the mold are put together by using alignment pins and clamps. The assembled mold with a PMT attached is shown in figure 4.8. The mixed and degassed main optical gel can now be injected into the assembled mold with a syringe. The mold needs to be filled up with gel until the gel is at the same level as the upper edge of the mold, just before the gel overruns. Important during the whole production process is the cleaning of the working place as the gel is difficult to clean up after curing. The gel has to cure 24 hours in the mold before the disassembly of the mold is possible. For this the tape around the PMT and the alignment tool needs to be removed and the alignment tool has to be unscrewed from the mold. Afterwards, the mold can be opened and the gel pad removed. Then, a gel pad is produced, attached to a PMT, and can be used for integration in a P-OM hemisphere. The detailed procedure of the gel pad production is shown in chapter A.2.

PMT Integration in Hemisphere

For the integration of the PMT with gel pad into the hemisphere of the P-OM, several requirements have to be fulfilled. The gel pad needs to be coupled optically to the glass of the hemisphere. This can be implemented by using an interface gel, which is the same as the coating gel, namely Elastosil 601 from Wacker in a ratio of 9:1 regarding components A and B. By coupling the gel pad to the hemisphere the modular design of the P-OM is satisfied, as a damaged gel pad could be removed from the hemisphere and exchanged even after the integration is performed. Also, the position of the gel pad and the PMT inside the hemisphere is defined and, therefore, needs to be satisfied.

This is achieved by an alignment tool for the integration, which can be attached to the frame inside the hemisphere and hence guarantees a good alignment of the PMT inside the hemisphere. Additionally, the location at which the PMT should be integrated needs to be parallel to the horizontal plane as the integration needs to be perpendicular to the surface of the glass to assure good coupling of the gel pad and the hemisphere with the interface gel. A hemisphere stand was developed to fix the hemisphere in position, which can hold the hemisphere in two different planes, one for the integration of the higher and one for the lower row of the PMTs in the hemisphere. Supplementary, the orientation of the hemisphere can be fine-tuned by two screws so that the position of interest is horizontal. In the following the procedure of integration is discussed in

Fig. 4.9: Picture of an integrated PMT with the alignment tool still in position.

detail.

In the start, the interface gel needs to be mixed in a ratio of 9:1 regarding the components Elastosil 601A and Elastosil 601B. A minimum mass of 7 g is required per integrated PMT. After the gel is mixed, it gets degassed until no bubbles are left. Then, the hemisphere needs to be prepared. This means that the position of integration needs to be horizontal, and the surface of the glass has to be cleaned. For the orientation of the hemisphere a bubble level was designed, which fits in the position of the PMT in the frame. When the hemisphere is in the right position and ready for integration, 7 g of interface gel can be applied with a syringe in the centre of the designated position. Then, the PMT can be put into place with the alignment tool for the integration. As soon as the PMT is at the correct place, it can be dropped the last few millimetres and should not be touched anymore afterwards. Gravity applies enough force to ensure a good coupling between the glass and the PMT by pushing the interface gel towards the rim of the gel pad. The interface gel needs 24 hours of curing before the hemisphere can be moved and the next PMT can be integrated at a different position in the frame. By attaching the locking mechanism, additional security is gained and the PMT gets safeguarded from getting loose. In figure 4.9, a PMT during the integration process is shown, and in figures 4.10 and 4.11, a hemisphere with eight integrated PMTs on the hemisphere stand is pictured. The detailed procedure of the PMT integration is shown in chapter A.3.

Fig. 4.10: Picture of a prototype hemisphere of a P-OM with eight integrated PMTs from the inside. The hemisphere is placed on the hemisphere stand.

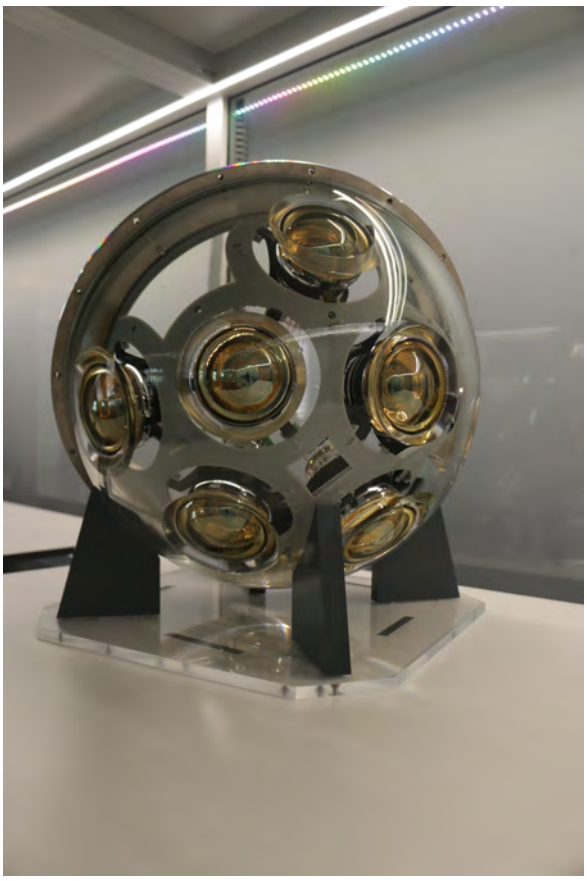

Fig. 4.11: Picture of a prototype hemisphere of a P-OM with eight integrated PMTs from the outside. The hemisphere is placed on the hemisphere stand.

Scaling up the Production Line

P-ONE-1 consists of 17 P-OMs and 3 P-CALs, as introduced in the P-ONE-1 design in chapter 3.2. As each P-OM contains two hemispheres, at least 36 hemispheres must be manufactured. Additionally, spare hemispheres for on-shore testing and backup prior the deployment are required. Scaling up the production and integration is essential to achieve this. The processes should be as easy as possible and a high level of quality needs to be ensured. As all processes of production and integration need to take place inside the clean tent, the space is limited, and procedures need to be optimised. The maximal capacity is the production and integration of 12 gel pads, respectively 12 PMTs, per working day.

Fig. 4.12: Picture of the integration table with two levels. On the upper level three hemispheres are pictured, wherein the picture is modified to show the up-scaling effect of three hemispheres.

Integration of 12 PMTs each working day requires to work on 12 hemispheres in parallel, as each integrated PMT has to cure for roughly 24 hours until the hemisphere can be moved. Two integration tables inside the clean tent with two levels each allow the necessary space management. On each level, three hemispheres can be integrated as shown in figure 4.12. Despite, also 12 gel pads need to be produced every working day. However as the curing of the gel pads also takes 24 hours, in total 24 molds are required. With 24 molds it is possible to produce 12 gel pads per working day and let them cure for 24 hours on the first day and use the other set of 12 molds on the next day for the gel pad production. This would result in an alternating system of 12 molds in each group. This production system is illustrated in figure 4.13.

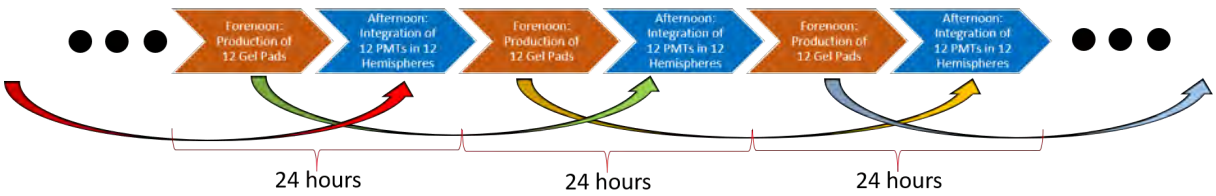

Fig. 4.13: Schematic of the planned shift system for the gel pad production and PMT integration.

Since the production and integration are manufactured processes, it's imperative to adequately train personnel for these procedures to ensure high quality. To ease this training process, two specialised groups will be formed, one of which focuses on gel pad production, while the other one on PMT integration. Thus, not all people need to be trained in all processes. Hence, in the forenoon, the gel pad production team can manufacture 12 gel pads, and in the afternoon, the integration team can integrate 12 PMTs with gel pads, which were produced the working

day before. Each team should consist of two people. This system was tested, and it was figured out that for the production and integration processes, 4 hours each time is sufficient to accomplish the required work. Hence, the shift system can be implemented in the production line of the hemispheres for the P-OM. All necessary parts like the hemisphere stands, the molds and other supplements are already ordered or currently in the ordering process. In total, the production of the P-OM hemisphere is estimated to take around three months of working, which is compatible with the timeline of the project. The start of production is currently terminated for the beginning of May 2024.

Quality Control

Constant checks will be mandatory to guarantee consistently good quality of the optical module components during production. Currently, the quality control protocols for the different steps are under development. The focus of quality control within this thesis is on the quality of the gel pad and its integration in the hemisphere. For the gel pad, qualitative visual inspections to detect impurities like dust grains or bubbles have to be performed. Similar parameters will be laid upon the integration, here, additionally the even gel outflow and orientation of the PMT and μBase need to be checked. These quality checks will be performed by experienced personnel who can evaluate the result by inspection of the gel pad. Additionally, a golden sample of a gel pad and integrated PMT with approved quality could be provided for comparison. While possible by design, adjustments will be time-intensive. Best practise in terms of quality control is to invest in proactive measures and provide good and extensive training for the personnel working on the production.

4.4 Evaluation of Assembled Hemispheres

A first assembly test was performed to check the P-OM's design and structure. This test examined if all components of the P-OM fit inside the hemisphere and all mounting holes are at the correct positions. Therefore all components planned to be placed inside the hemispheres were sent from the collaboration partners to the TUM. It is mentioned that several parts were still in the development phase, leading to the fact that nearly all parts were in a preliminary realisation. For testing, a hemisphere with 8 integrated PMTs was used, and then, step by step, several components were assembled inside the hemisphere. The tested parts were the flasher beacons for optical calibration and the acoustic receiver for the acoustic calibration which are located in the cutouts of the frame between the PMT positions. Also tested were the interposer board, mounted to a specialised holding structure, and the SMUT and main board, both placed in the plane of the hemisphere flange.

The first assembly of one hemisphere of the P-OM reveals several findings. Firstly, the mounting of the cutouts requires optimisation to facilitate easier assembly of the parts. Furthermore, the positioning of the interposer board is too close to the PMTs, resulting in contact with the μBases of the PMTs located near the pole of the hemisphere. This necessitates adjustments to both the mounting of the interposer board and the soldering of the μBases closer to the PMT neck.

The SMUT was not fitting in the foreseen position, and the mounting needs to be reworked to guarantee a safe mounting. The main board must be designed to be mounted on the same mounting structure developed for the SMUT.

4.5 Outlook

Based on the findings of the first P-OM assembly, a second assembly was scheduled for the end of February 2024, combined with a shock and vibration test of the hemisphere to check the conceptional design of the module. The preparations for the second assembly are currently ongoing. Parallel to the hardware testing of the components of the P-OM, the OMCU setup at TUM gets updated to be able to test a hemisphere with integrated PMTs. Hence, it would be possible to test a produced hemisphere in the setup while checking the functionality of the PMTs integrated in the hemisphere. Also, this would allow a comparison of the testing results with the measurement results obtained during the Aachen characterisation tests. Additionally, the working schedule for the production of the P-OMs is set up and people are hired and prepared.

5 Oceanphysics Introduction

P-ONE will be located in the deep sea in the Pacific and could act as a platform for long-term research in the scope of oceanography. Therefore, the following chapter focuses on the characteristics of the ocean and the underlying physical properties and mechanisms.
Oceans cover 70.8% of the Earth's surface, and only 29.2% is capped by land. This gives a surface area of $361 \times 10^6\,\mathrm{km}^2$ and a volume of $1.37 \times 10^9\,\mathrm{km}^3$ of seawater on the Earth. 97% of the Earth's water is stored in the oceans. The water masses are not evenly distributed over the earth; in the northern hemisphere, only 61% of the surface is covered with water, whereas in the southern hemisphere, 81% of the area is capped by water [62, 25]. Officially, the water masses on Earth are divided into three oceans: the Pacific, the Atlantic, and the Indian Ocean [25]. However, two additional oceans can be inducted: the Arctic Ocean and the Southern Ocean, the latter being the southern extension of the three main oceans and surrounding Antarctica. The average depth of the oceans is 3800 m, which can be measured in two ways. The first is by using acoustic echosounders mounted on ships measuring the depth by detecting the echo of a transmitted sound signal, and the second is by using satellite-based altimeters to scan the ocean surface and reconstruct the topography of the sea floor [25]. Of all these oceans, the Pacific is the largest and deepest, with a surface of $166\,\mathrm{km}^2$ and an average depth of 4282 m. In general, the oceanic province is divided into several depth zones, of which only one zone is relevant for P-ONE. This zone ranges from 1000 m to 4000 metres in depth and is called the bathypelagic zone. It is characterised by the absence of any light and thus is an aphotic zone. Approximately 75% of the ocean's volume lies at these depths [62, 25].
P-ONE will be located, as already introduced, at the Cascadia Basin. It is situated close to the border of the Pacific and the North American plate, on the Juan de Fuca plate enclosed by these two. This location is characterised by the transform plate boundary of the Pacific and North American plates, meaning that the tectonic plates are sliding past each other. Additionally, this region is labelled as a subduction zone, wherein the Pacific plate is slowly sliding under the North American, resulting in a high risk of earthquakes [62, 63].

5.1 Properties of Water

Water is a unique molecule, as it is a polar molecule, existing naturally in solid, liquid and gaseous form under a normal range of temperatures and pressure on Earth. Water has a high heat capacity, meaning that a high amount of energy is needed to raise the temperature. Therefore, it can absorb large amounts of heat without increasing its temperature. This is caused by the hydrogen bonds between the molecules, which first have to be broken before the free movement of the water molecules is possible, and hence, the temperature rises. The characteristic also results in a high latent heat of water, as a high amount of heat is required to undergo a phase change of water. The high heat capacity of the oceans is one important point in stabilising and regulating the global climate, as it prevents rapid changes in water temperature and, thus, also slows changes in the atmosphere. This is also a crucial property for aquatic organisms [62].

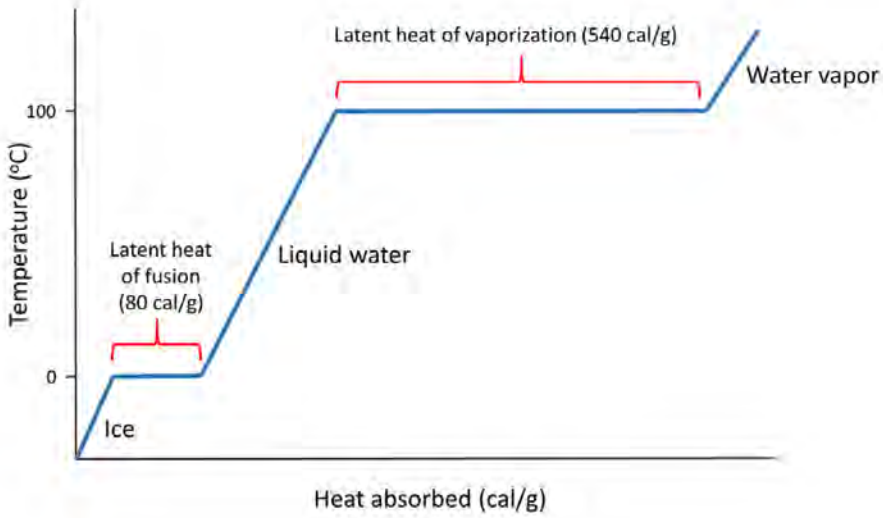

Fig. 5.1: Required latent heat for phase changes in water. Latent heat of fusion is the heat required to melt ice, and latent heat of vaporisation is the heat required to turn liquid water into water vapour [62].

Water acts as a "universal solvent". This implies that water dissolves more substances than any other liquid. Especially ionic salts are dissolved very well, as the polarity of water can weaken the bonds of the ions and, therefore, dissolve them. Another characteristic of water is that the solid phase of water is less dense than the liquid phase. As the crystal structure of water requires more space due to the hydrogen bonds than liquid water, the density of ice is less, resulting in ice floating on liquid water. This property has again effects on the behaviour of oceans and the global climate. The higher albedo effect of ice reflects more sun radiation than the darker liquid water, reducing the amount of energy absorbed by the Earth. Also caused by this density anomaly is the stable temperature for deep sea water between 0 °C and 4 °C, as sea water around these temperatures has the highest density. For saltwater, the dissolved salts impede the formation of the crystal lattice, lowering the freezing point of seawater at around −2 °C, depending on the salinity of the water [62].

5.2 Salinity

The simplest and most broad definition of salinity is: the mass of all solved material in grams in one kilogram of seawater. Salinity itself has no unit. However, the abovementioned definition is practically hard to measure or verify. Other definitions were made to allow easier measurement principles, on of the latest ones is measuring the conductivity of sea water [62]. Regarding salinity, oceans are in a steady state. The residence time for constituents is high and ranges from a few hundred years to 100×10^6 years for chloride. All salts and ions dissolved in seawater contribute to the overall salinity. On average, there are 34.7 g salt per kilogram of seawater,

resulting in 34.7 parts per thousand [25]. Of these dissolved ions, 99.4% are chloride, sodium, sulfate, magnesium, calcium and potassium. The remaining 0.6% are radio nucleotides, organic compounds, metals and others at small concentrations from part per million to parts per billion [62]. The absolute salinity may differ for different locations, but the relative proportions of the major six ions, which were listed before, are always constant. This is called rule of constant proportions. This results in the ability to measure only the concentration of one of the main ions and calculate from that the absolute salinity. The rule of constant proportions for salinity is not valid for coastal regions and closed seas like the Dead Sea [62]. The absolute salinity varies depending on the latitude. Hereby, for the North East Pacific, it is lower than the average and ranges from around 31 to 33 ppt [62]. Next to geographical variations in the salinity, it also changes in dependence of depth. As deeper water stays unaffected by surface processes like evaporation, precipitation, runoff and ice cover, the salinity in greater depths remains relatively uniform. Also, for the depth between 10 to 200 metres, a mixing layer leading to a quite uniform salinity as the water gets mixed by wind, waves and surface currents is formed [25]. The depth of this mixing layer changes daily as it depends on the heat flux and turbulences [62]. Below the mixing layer forms a so-called halocline, which describes a rapid change in salinity over a small change in depth. This is the transition between the mixing layer and the deep ocean. Below the halocline, there are, as mentioned before, only little variations in salinity down to the seafloor [62]. The theoretical profile of salinity for two different hypothetical sites in the open ocean is shown in figure 5.2.

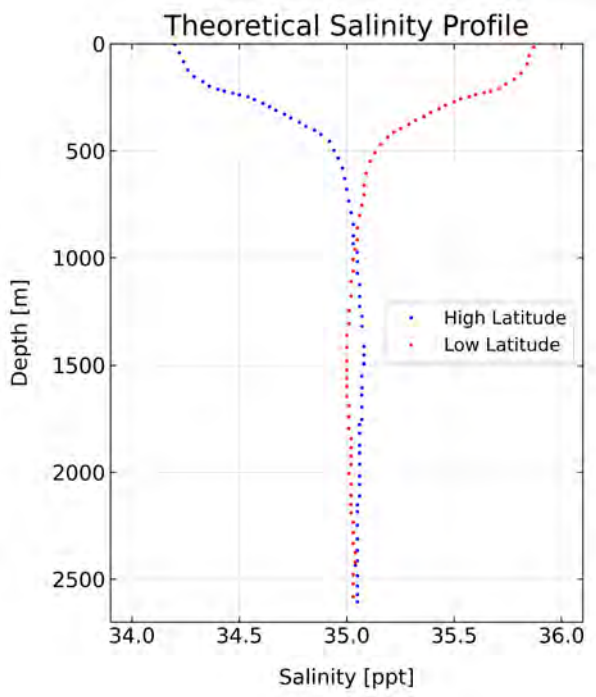

Fig. 5.2: Theoretical salinity profiles of two different hypothetical locations in the open ocean with different latitudes. Data extracted from [62].

5.3 Dissolved Gases in Oceans

Next to ions and other particles, gases are also dissolved in the water of the oceans. Such gases are oxygen, carbon dioxide and nitrogen. The percentages of the total gas in each compartment are shown in the picture 5.3.

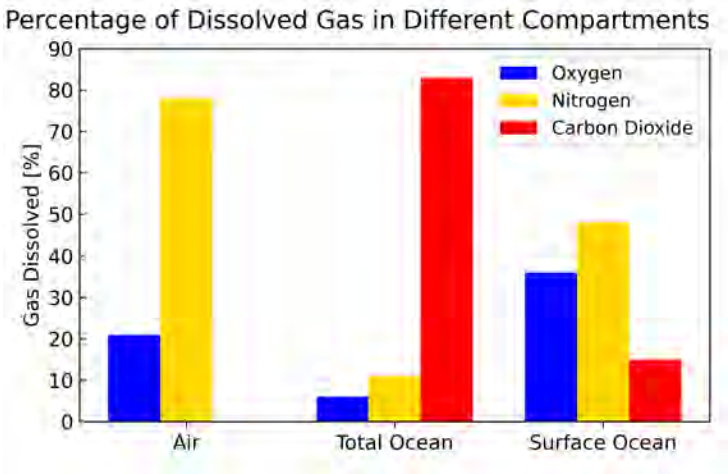

Fig. 5.3: The percentages of dissolved gasses in the different compartments on Earth [62]. In the air the concentration of CO_2 is at 0.04%.

For seawater, the amount of gas in the water depends on the solubility and saturation of the gas in water. The solubility describes the amount of dissolved gas in water under certain conditions, normally at 0 °C and a pressure of 1 bar. Saturation is defined by the amount of gas currently dissolved in the water relative to the maximum. In the ocean, most gases are saturated excluding O_2 and CO_2 as they are used by living organisms and under go constant turn over. In the following, the properties and influences of these two gases on the ocean are discussed in more detail [62].

Oxygen

A typical profile of dissolved oxygen is shown in figure 5.4. The concentration is highest at the surface, as the oxygen from the atmosphere dissolves in the water and phytoplankton produces oxygen through photosynthesis. In this layer, the respiration by organisms is smaller than the oxygen-producing processes. With increasing depth, the dissolved oxygen declines, reaching a minimum at the so-called oxygen minimum layer. This layer is located at around a few hundred to 1000 metres of depth. At this depth, no atmospheric exchange is possible, and no light for photosynthesis is available. Thus there is no addition of oxygen, but respiration occurs due to deep water organisms and the decomposition of organic material by bacteria as the material sinks to depth [62].

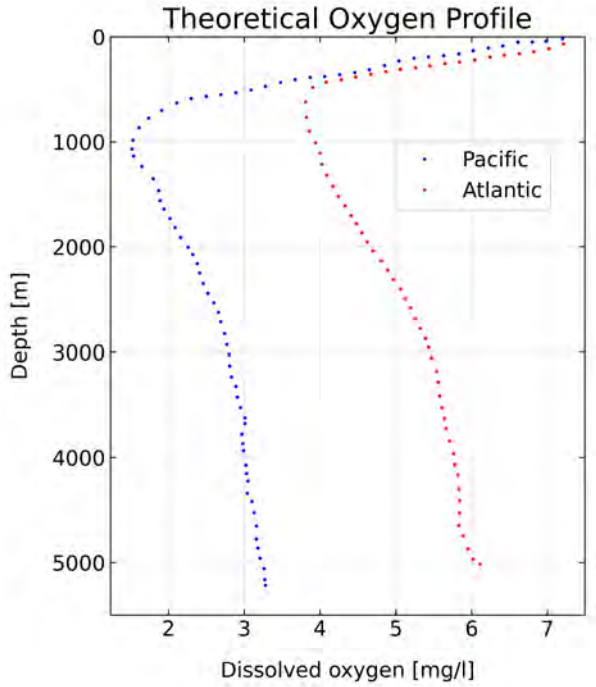

Fig. 5.4: Theoretical dissolved oxygen profiles for the Pacific and Atlantic Ocean. Data extracted from [62].

Below the oxygen minimum layer, an increase of oxygen at greatest depths is often observed as the water is usually colder and the pressure is higher. This leads to an increased solubility of dissolved gases. Next to that the thermohaline circulation brings at the polar regions cold, oxygen-rich water to the bottom. This causes a higher level of dissolved oxygen in the Atlantic than in the Pacific, due to the Atlantic Meridional Overturning Circulation (AMOC) [62].

Carbon Dioxide

For carbon dioxide, the profile with respect to depth looks essentially the opposite of one of dissolved oxygen as both gases are involved in the same biological processes, in which they work the opposite ways. Close to the surface low concentrations of dissolved CO_2 are observerd due to photosynthesis and the utilisation of carbonate for shells of organisms. In deeper water, the CO_2 concentration rises as respiration exceeds photosynthesis, and organic material decomposition adds additional CO_2 to the water. As for O_2, colder water and higher pressure result in a higher solubility, and therefore, more CO_2 can be dissolved in deep water.

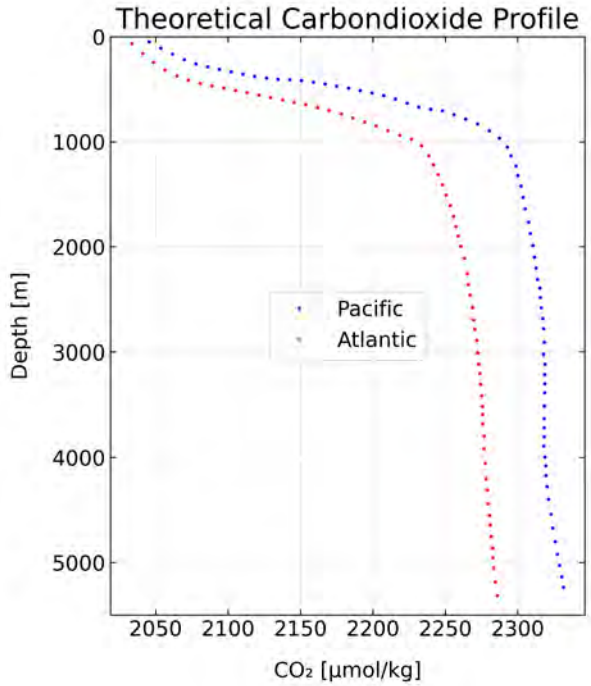

Fig. 5.5: Theoretical dissolved carbon dioxide profiles for the Pacific and Atlantic Ocean. Data extracted from [62].

As pictured in figure 5.5, the deep Pacific contains more CO_2 than the Atlantic, as the Pacific water is older due to the slower thermohaline circulation and hence accumulated more CO_2 from the respiration of organisms over time. But with respect to O_2, the behaviour of CO_2 in the ocean is more complex. When CO_2 dissolves in water, a number of different compounds can be produced by interacting with water, shown in the reaction formula 5.1 [62].

$$CO_2 + H_2O \leftrightarrow H_2CO_3 \leftrightarrow H^+ + HCO_3^- \leftrightarrow 2H^+ + CO_3^{2-} \tag{5.1}$$

Most of the CO_2 dissolved in the oceans is converted to bicarbonate (HCO_3^-), and thus CO_2 is prevented from reaching equilibrium with the atmosphere. Hence, seawater can hold 50 to 60 times as much CO_2 as stored in the atmosphere. CO_2, by being in equilibrium with its compounds, acts as a buffer for the pH value of the ocean. As the pH value is the negative logarithm of the concentration of the H^+ ions, a higher concentration of H^+ ions leads to a lower pH value. The current pH value of the oceans is 8.1, resulting in a slightly basic environment in the seawater [62]. The pH value of the ocean is regulated by shuttling H^+ ions back and forth between the various compounds of CO_2, as shown in formula 5.1. Hence the conditions stay favourable for life in the seawater. But this balance can get disturbed and could lead to ocean acidification. One possible cause is adding CO_2 to the seawater, as the atmospheric concentration increased due to anthropogenic sources since the industrial revolution. The oceans

absorb therefore an increasing amount of CO_2, leading to a decreasing pH value and ocean acidification. A decline of the pH value from 8.2 to 8.1 was detected in the last century, in other words the ocean got 30% more acidic over this time period. That effects the creation of shells of organisms strongly as they are built of calcium carbonate, which dissolves faster in a more acidic environment. Additionally, it gets harder for shell formation in general as the amount of free carbonate ions in the seawater decreases [62]. This has impacts on the whole ecosystem of the oceans and hence can also affect the food chain, including humankind [64].

5.4 Physical Oceanography

Pressure

Pressure in the context of Oceanography means usually the hydrostatic pressure, caused by the weight of the water column pressing down on an object due to gravity. The deeper, the higher the pressure gets as the weight of water above an object increases. At the water surface, there is a pressure of 1 atm, and the pressure increases nearly linearly with depth at a rate of 1 atm every 10 metres [62].

Temperature

In the oceans the temperature ranges from $-2\,°C$ to $30\,°C$. This great range is only valid for surface water, as most of the water is located in the deep sea, where the average temperature lies at around $3.5\,°C$ [25, 62].

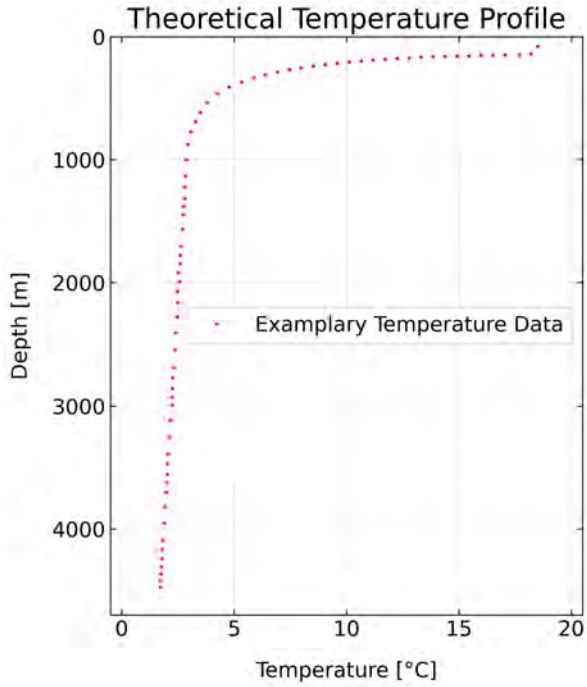

Fig. 5.6: Theoretical temperature profile for a typical open ocean location in a mid-latitude region. Data extracted from [62].

As shown in figure 5.6, for mid-latitude locations the temperature is the highest at the surface, as the water gets heated by the sun. For the first 100 to 200 metres the temperature stays fairly constant, as here the mixing layer is located. In this layer a mixing of water occurs forced by wind, waves and currents. Below the mixing layer a thermocline is present, where the temperature drops rapidly over a narrow increase of depth. Below the thermocline, the temperature is fairly constant at about 2 °C down to the seafloor. The temperature fluctuations in the deep ocean are mostly less than 0.5 °C. The temperature profile depends strongly on the latitude, where mostly the thermocline is impacted, leading to different depths and inclines [62].

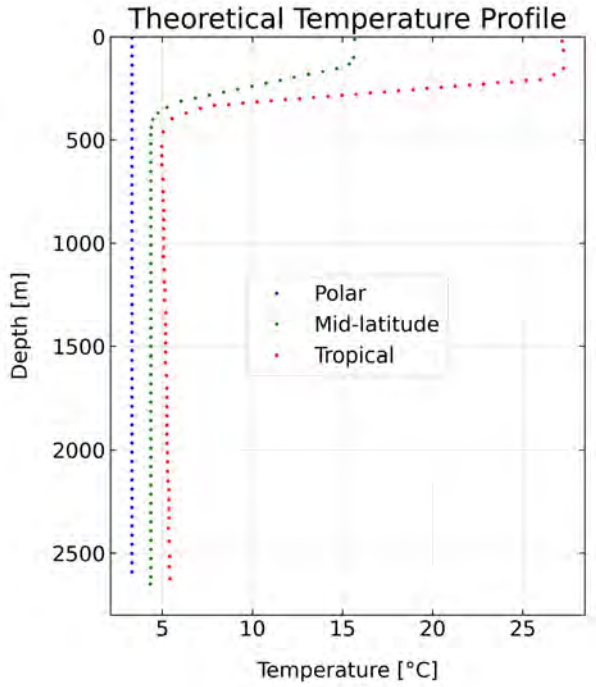

Fig. 5.7: Examplary temperature profiles for three different locations at varying latitudes. Data extracted from [62].

Density

Density is defined as the mass per unit volume. For freshwater, it is $1\,\mathrm{g/cm^3}$ at a temperature of $4\,°\mathrm{C}$. Due to the dissolved salts and substances in seawater, the density at the surface is at 1.02 to $1.03\,\mathrm{g/cm^3}$. Often the density is not given in absolute values, but in $\sigma(S,T,p)$, describing the offset of the density from the density of freshwater, given by formula 5.2 [62]:

$$\sigma(S,T,p) = \rho(S,T,p) - 1000\,\mathrm{kg/m^3} \tag{5.2}$$

Herein S stands for the salinity, T for the temperature and p for the pressure. Thus, it is apparent that the density depends on all the parameters, wherein the pressure has the least impact, as water is nearly incompressible except for extreme depths. In contrast, temperature has the greatest impact on the density of seawater, leading to a shape of the density profile, which is in comparison to temperature profiles mirrored [62].

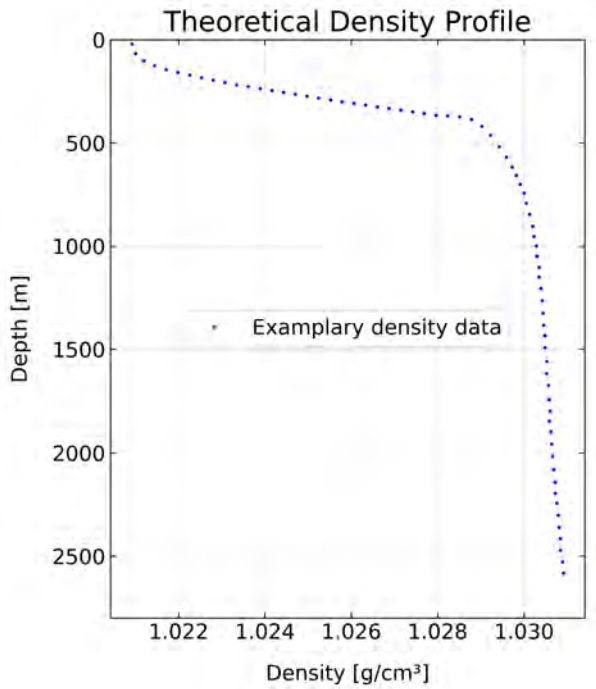

Fig. 5.8: Theoretical density profile for the open ocean at a mid-latitude location. Data extracted from [62].

As shown in figure 5.8, at the surface the density is the lowest as the temperature is the highest. With increasing depth, the density rapidly increases. This range of depth is called pycnocline and coincides with the thermocline of the temperature profile. Below the pycnocline the density stays quite constant or may continue to increase slightly with the depth to the bottom [62]. This shape of density profile is the case for a stable state. But if denser water forms at the surface due to cooling down close to the poles, for example, the water masses get unstable, and a vertical movement starts. This movement is called thermohaline circulation, which is based on the density of the water. The density is dependent on the temperature and the salinity, which gives the name for the circulation [62].

Light

The sunlight and hence the radiant energy of the sun is one of the major drivers of atmospheric processes, i.e. winds as well as global ocean currents and the climate in general. Also, it warms the surface water of the oceans and provides the light for photosynthesis. On the other hand, water absorbs light very effectively, only 1% of the original intensity reaches 100 metres in depth. Beyond 1000 metres of depth, there is no light left. The absorption is wavelength dependent, wherein blue and green light have the highest transmission [25]. Also the transparency of the ocean water depends strongly on the location, i.e. close to the coast or in the open ocean. Additionally, the ocean can be divided into depth layers. For the first 200 metres, there is the

photic, respectively, the euphotic zone where enough light is available for photosynthesis. Until 1000 meters the dysphotic zone is located. Here is still light available, but there is not enough for photosynthesis. Below the 1000 meters, there is no light left, and complete darkness prevails. Hence the zone is called aphotic zone [62].

As already introduced in chapter 2.6, the optical properties of the water are important to know to allow proper event reconstruction of possible neutrino events. In chapter 6, the environmental properties of the Cascadia Basin are probed.

6 Water Characterization in Cascadia Basin

The water of the Pacific Ocean will be used as a Cherenkov medium for the neutrino telescope. The optical and ambient properties of the water are crucial to reconstruct the direction and energy of incoming neutrinos. In the following chapters, environmental properties are investigated based on CTD (Conductivity and Temperature over Depth) measurements and seawater samples from the Cascadia Basin.

6.1 Analysis of CTD data at Cascadia Basin

CTD measurements were taken on an exploration cruise by the *R/V Thompson*, which took place from 31st of July to 8th of August 2023 with the cruise number TN-421. Data were taken at two sites, located close to the site of the pathfinder missions, which is also anticipated for P-ONE-1. The first site is drill hole U1362A, located at 47.761389 N and 127.760833 W, and the measurement was done on 1st of August. The second site is drill hole U1362B at 47.761666N and 127.760555 W, where the data were taken on 6th of August. The distance between both drill holes is 38 m. At each site, data were collected during the rosette's descent and on the way to the surface.

A CTD measurement describes a measurement of environmental parameters in the ocean, concrete conductivity and temperature over depth (CTD), where the parameters of interest are monitored over a height profile in the water. This measurement was performed with the CTD Niskin rosette sampler of the University of Washington using a custom-built SBE 9plus Seabird instrument package and executed by the R/V Thompson's Shipboard Scientific Services Group and the crew. At this rosette, several measurement devices are mounted to quantify the environmental parameters. The following parameters have been measured:

- Depth [m]
- Pressure [db]
- Salinity [PSU]
- Temperature [$^{\circ}C$]
- Oxygen [ml/l]
- Beam Attenuation [1/m]
- Beam Transmissivity [%]
- Fluorescence [mg/m^3]
- Density [kg/m^3]
- Sound Velocity [m/s]

Only the parameters of pressure, conductivity, temperature, oxygen, beam attenuation and transmissivity, fluorescence and sound velocity are detected directly. The remaining values are calculated by the direct data. The pressure derives the depth, the data of the conductivity are calculated with the salinity, temperature and pressure. The density is derived by the salinity and the temperature.

In figures 6.1 and 6.2, a standard CTD-diagram for the two different sites are shown. In these diagrams, the temperature, oxygen and density are pictured over a depth profile, wherein the data of the descent and the ascent are displayed. The data of each parameter are similar for both locations, which was expected as the distance between the two drill holes is 38 m. Also, there is no difference in the data visible regarding the data taken on the descent and the ascent.

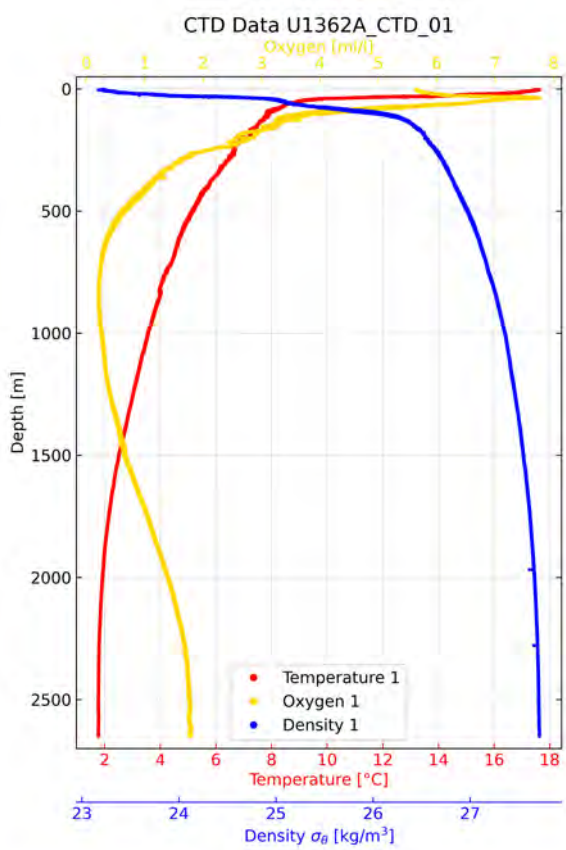

Fig. 6.1: Measurement for temperature, oxygen and density over depth at location U1362A.

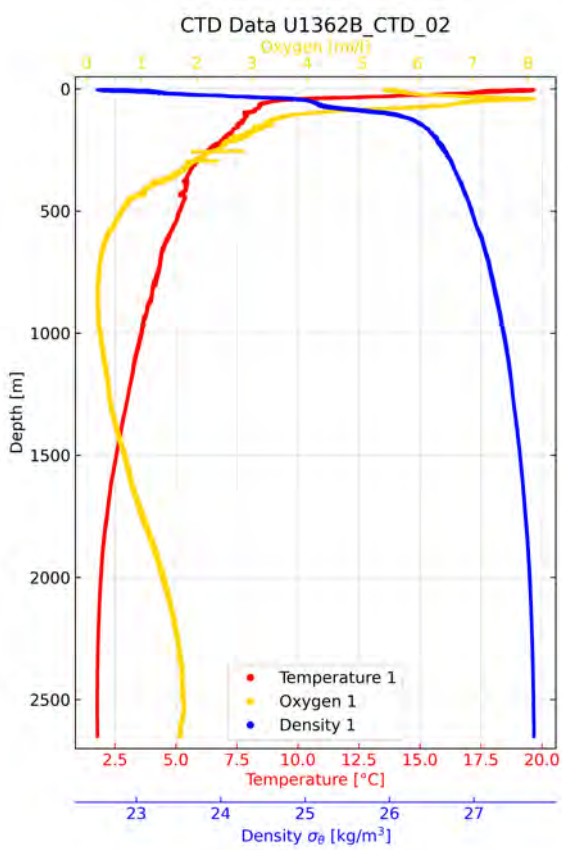

Fig. 6.2: Measurement for temperature, oxygen and density over depth at location U1362B.

The extract of 0 to 500 metres of depth is shown in figures 6.3 and 6.4. For the oxygen, the data show a maximum concentration at a depth of around 50 metres. Below 50 metres until 100 m,

the concentration decreases rapidly, whereas below 100 m, the concentration declines nearly constant till 500 m and reaches its minimum at around 1000 metres. Below 1000 m, the oxygen concentration increases slowly down to the bottom. This behaviour matches the expected profile introduced in chapter 5.3. An interesting feature is the peak of oxygen concentration at around 50 m depth, which can be explained by the peak of oxygen production in this depth as there is still enough light for photosynthesis, but no exchange with the atmosphere is occurring.

The temperature profile of the measurements shows the anticipated pattern as introduced in chapter 5.4, wherein the mixed layer and the thermocline are very narrow. The rapid decrease in temperature stops at a depth of 50 m and, drops continuously at a moderate rate until the sea floor is reached. Also, the density shows a similar profile as already introduced in chapter 5.4. For these measurements, the pycnocline is also over a short range of depth, and the dependence of the density from the temperature is apparent as the slower decrease starts at nearly the same depth at around 50 m.

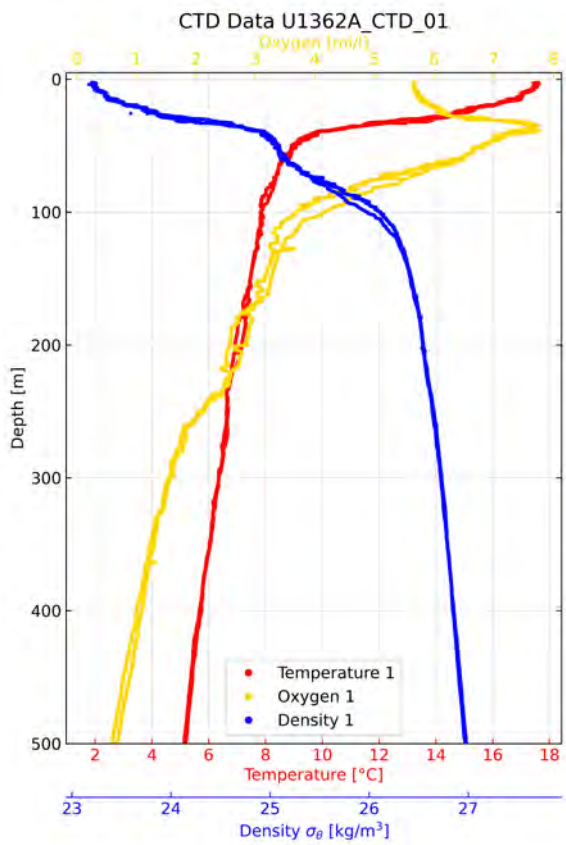

Fig. 6.3: Measurement for temperature, oxygen and density over a depth from 0 to 500 metres at location U1362A.

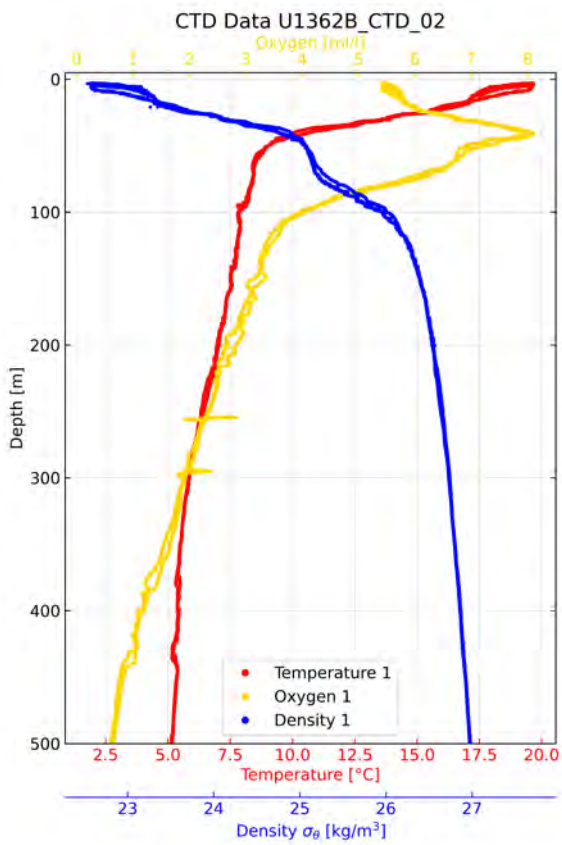

Fig. 6.4: Measurement for temperature, oxygen and density over a depth from 0 to 500 metres at location U1362B.

The measurements of the salinity and the sound velocity are shown in figures 6.5 and 6.6. The data of both measurement runs at the different sites are shown in one graphic. It is visible that the data do not differ depending on the location they were taken. For the salinity, only small aberrations from the theoretical profile introduced in chapter 5.2 are visible. Standing out is that the mixed layer is nearly nonexistent. The halocline is narrow and very close to the surface as it ends at around 200 m of depth. Below this depth, the manner of the salinity profile behaves as expected. Also, the absolute value of salinity at the sea floor matches the expected average merits roughly. The sound velocity is important to characterise as P-ONE is also planned to implement an acoustic calibration system, as introduced in chapter 3.2. The depth dependency of the sound velocity needs to be taken into account for the geometry reconstruction. Figure 6.6 shows that for depths below 1000 metres, the sound velocity behaves very predictably, and no deviations or disturbances occur.

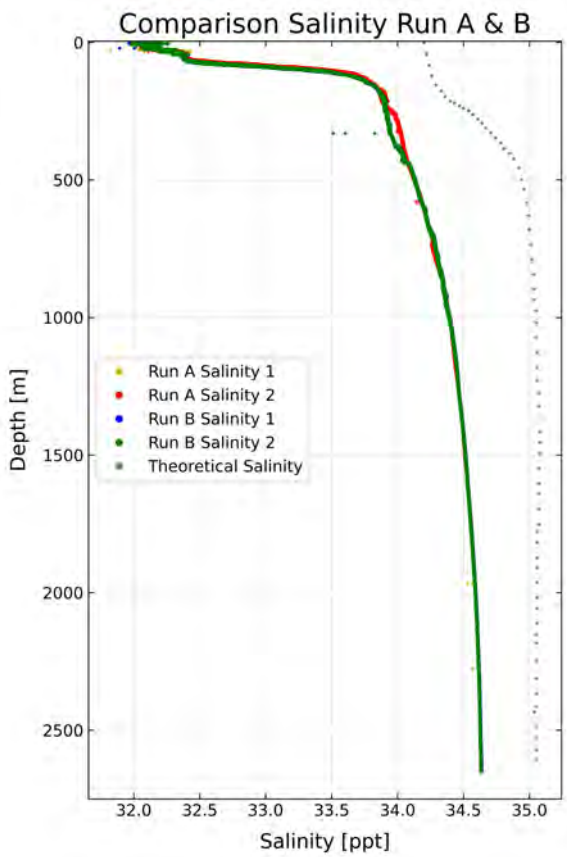

Fig. 6.5: Measurement of the salinity over depth at the locations U1362A and U1362B. The theoretical salinity values for high latitudes are pictured in grey [62].

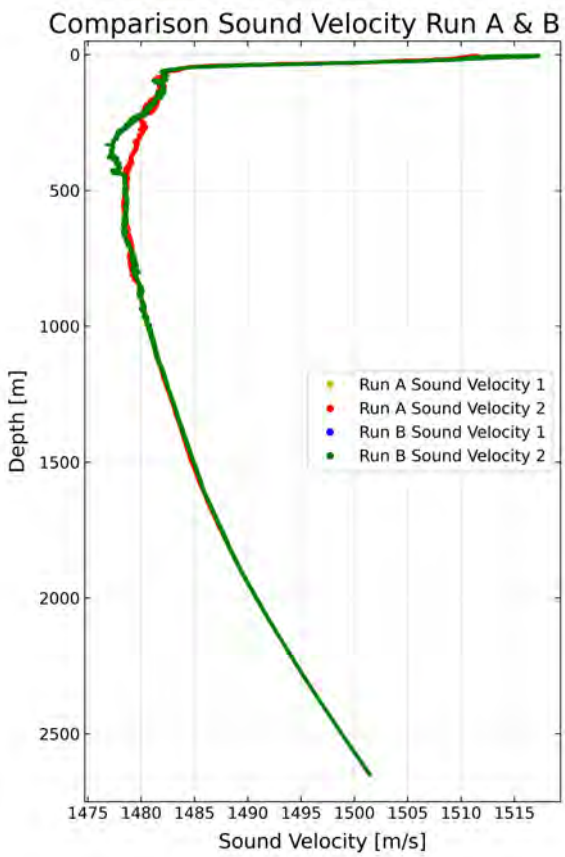

Fig. 6.6: Measurement of the sound velocity over depth at the locations U1362A and U1362B.

During the CTD measurements, it was also possible to test the attenuation and transmissivity of a beam in situ with a WET Labs C-Star Transmissometer. The transmissometer has a path length of 0.25 m and can measure at a wavelength of 470, 530, 650, or 715 nm [65]. The measurements of both locations for the attenuation and the transmissivity are shown in figure 6.7. It can be seen from the measurement that, especially for great depths, the transmissivity of light is very high, and the attenuation of the beam is very small. This leads to the conclusion that the water is very clear and few photons get absorbed or scattered in the water.

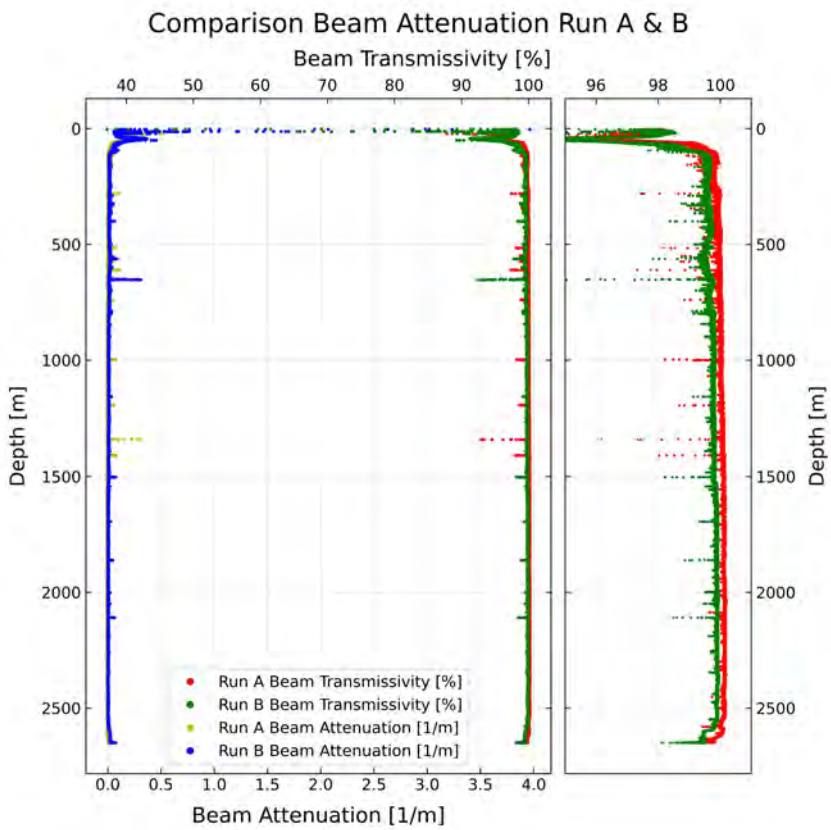

Fig. 6.7: Measurement of the attenuation and transmissivity of a beam over depth at the sites U1362A and U1362B.

6.2 Optical Characterisation of Water Samples from Cascadia Basin

The water samples were taken by ONC with a Remotely Operated Vehicle (ROV) during the recovery operation of the pathfinder mission STRAW-b in 2023. During an ROV dive samples were taken in a height of 50 m above ground (a.G.), 500 m a.G. and 1000 m a.G.. For each height, a volume of 3 litre was sampled and they were stored dark and cool (below 4 °C). After the end of the cruise, the samples were sent in a cooled box by express to Munich for analysis

and testing.

One of the most relevant parameter for neutrino telescopes is the attenuation length. As introduced in chapter 2.6, this value is defined by the distance it takes to reduce the intensity of a light beam by the factor $1/e$. The chair E15 of the physics department at TUM has an experimental setup for measuring the attenuation length of different types of scintillators for the JUNO experiment [66]. They kindly provided their infrastructure so that the setup could be adapted to analyse seawater. This required changing all components in the setup that could come in contact with the water since they could contaminate the material used.

6.2.1 Experimental Setup at TUM

The experimental setup consists of a Thorlabs SLS301 halogen lamp [67], which provides a time-consistent intensity of light, a Thorlabs PM16-121 powermeter to check the power emitted by the lamp [68], a monochromator, an OceanOptics Maya2000Pro spectrometer to analyse the spectrum given by the monochromator [69], a collimator, a mirror, a horizontal sample pipe containing the tested liquid, and an Atik Apx 60 camera [70] at the top of the sample pipe. Parallel to the measurement, a height scale and a movable water tank are located, with which the water height inside the sample pipe can be adapted. Figure 6.8 shows a schematic of the setup. The water tank is connected to the bottom of the sample pipe with a tube, granting that the water level in the tank is always the same height as the water line in the sample pipe. By reading the height of the water level in the water tank using the height scale mounted next to it, the height of the water line inside the sample pipe can be determined. By adapting the water tank's height, the water line inside the sample pipe can be changed, and the intensity of different fill heights can be measured. For this, the beam of the halogen lamp, which provides a wide spectrum, gets filtered by the monochromator to select a specific wavelength. A peak wavelength of $\lambda = 430\,\mathrm{nm}$ was selected in all tests. After the monochromator, the beam is focused by the collimator and reflected into the bottom of the sample pipe. For this, a mirror is located under the sample pipe and adjusted so that the beam goes rectangularly upwards and enters the sample pipe through a glass window at the bottom side. From there, the beam goes parallel to the walls inside the pipe until it hits the camera at the top of the pipe. By varying the height of the water line inside the sample pipe, the attenuation of intensity created by the water changes. By adapting the height of the water line inside the sample pipe and measuring the incoming intensity of the light beam by the camera for these adjusted heights, the intensity variation can be measured as a function of the fill height inside the pipe. An attenuation length can be calculated by applying a Beer-Lambert fit for the data analysis.

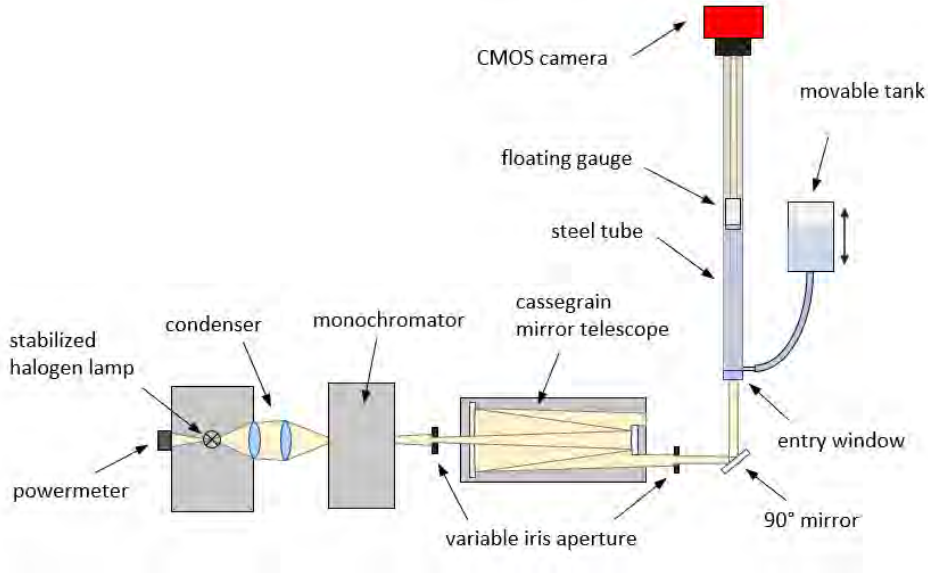

Fig. 6.8: Schematic of the experimental setup for measuring the attenuation length of water. Figure provided by V. Rompel.

As mentioned above, the setup needed to be adapted for analysing seawater to avoid any contamination of the salt water on the setup. All components that come in contact with the seawater had to be changed. In the original setup, a sample pipe of a length of around 3 m, which is painted inside with a non-reflective coating to avoid reflections inside the pipe, was used. This pipe was exchanged by a new sample pipe of 3 m length, 29 mm outer diameter and 1.5 mm wall thickness made of stainless steel EN 1.4435, produced by Dockweiler [71]. To use the pipe for the setup, two adapters needed to be welded to the pipe. An adapter for the glass window is needed at the bottom end of the sample pipe. At the top part, an adapter for holding the camera is necessary. After placing the adapters, the new sample pipe was cleaned with Isopropanol and Acetone to remove all remaining dust and impurities inside the pipe. Also, the water tank for adapting the height of the water stand in the pipe was exchanged, and the connecting pipe between the tank and the sample pipe was replaced by a Teflon tube of 8 mm inner diameter. The experimental setup is shown in the figures 6.9 and 6.10.

Fig. 6.9: Front view of the experimental setup for analysing water samples. The camera is attached to the holding structure on top. The height scale is located right, parallel to the sample pipe.

Fig. 6.10: Top view of the box containing the halogen lamp, powermeter, monochromator, spectrometer, collimator, mirror and lower holding structure for the sample pipe.

6.2.2 Optical Properties of Water Samples

General Measurement Procedure

All measurements of the attenuation length of the water samples followed the same general procedure. This procedure is described in the following. Deviations of this procedure in the individual measurements of the samples are noted and described in the corresponding sections.

In the first step, the setup gets prepared for a new measurement. This includes switching on the halogen lamp and the camera. Firstly, the camera is powered on to guarantee a constant intensity. The lamp is often operated constantly to avoid warm-up time. In the second step, the monochromator is set to the required wavelength and the spectrum is validated with the powermeter, in all measurements, the wavelength was set to 430 nm. The third step is to check if the pipe, the tubes and the tank are water-free. Afterwards, the sample gets filled in the system either by filling water at the top of the sample pipe or by filling up the tank. After enough water is in the system (about 2.5 l), the tank gets lifted to the highest possible position so that the sample pipe is nearly filled with the sample. After the lab is dark for the measurement, the beam will be focused on the camera without reflections on the pipe wall. Afterwards, the camera settings were adjusted to ensure the intensity measurement worked properly. To take data, the tank gets set to a specific height, the water line height gets measured with the scale next to the tank, and the system gets some time so that any oscillations and vibrations in the water can break off. Then, multiple intensity measurements are taken with the camera for the adjusted height. When a minimum of 5 measurements are made for this height, the tank gets lowered by a defined distance, and the same data-taking process occurs again. This is done for as many different heights as possible until the beam is not identifiable on the camera image. Then, the mirror is adjusted so that the beam is again focused on the camera. Then, the data-taking process could be continued. However, below a certain height, it is impossible to get a precise measurement of the beam by the camera, and the measurement procedure is finished.

Since there are issues with the measurement results and hence they are not usable, no uncertainties were assumed and calculated for the following analysis.

First measurements of Water Samples

The first measurement was performed with the water sample taken from 500 m a.G. Before the measurements, ice was seen in one of the three bottles, but the water still appeared very clear and seemingly did not change due to transport or storage. As shown in figure 6.11 it is observed that the first data for the highest heights are compared with the data of lower heights not in the expected scope. One hypothesis is that at the measurement's beginning, small ice pieces inside the water created measurable absorption and scattering effects.

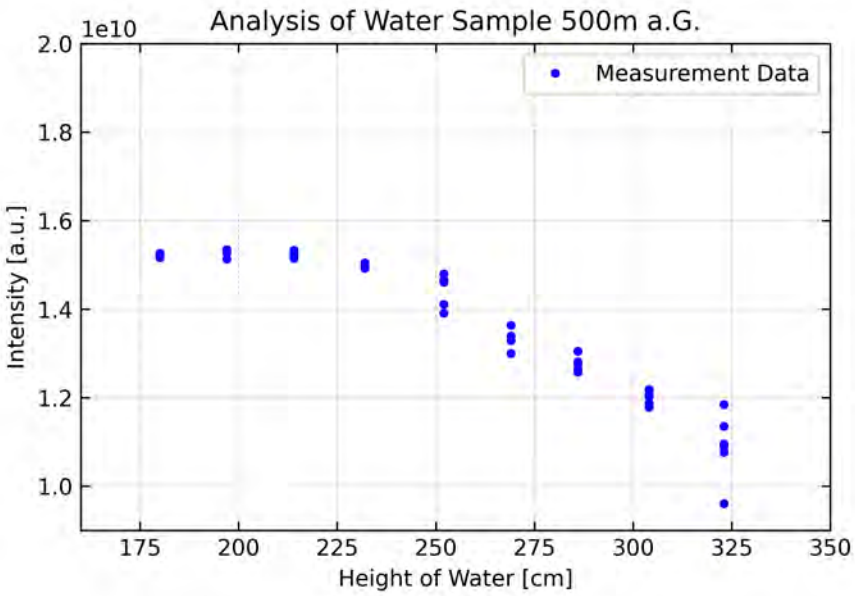

Fig. 6.11: Measurement of the first testing of the water sample from 500 m a.G.

The second tested sample is from a depth of 1000 m a.G. This sample was ice-free and had no noticeable difference to the 500 m a.G. sample in terms of transparency. It is also clear, and no changes due to transport or storage were visible. As shown from figure 6.12, there is no kink for high water levels in the data, but there are no data taken for low water levels. This is due to a bad image of the beam on the camera for these low heights, which might be explained by condensed water on the camera lens, as the camera is cooled to $-20\,°\mathrm{C}$.

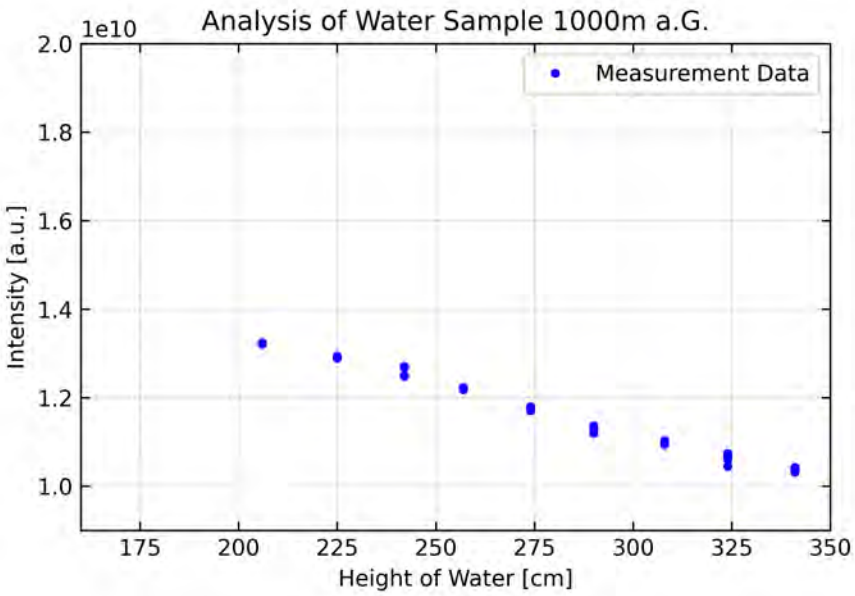

Fig. 6.12: Measurement of the first testing of the water sample from 1000 m a.G.

The next tested sample is from the depth 50 m a.G. and showed also no ice inside the container. Like the other samples from the deep sea, it showed no visible changes due to transport or storage. As a result of the condensed water on the camera lens in the measurement for the 1000 m a.G. sample, it was decided to clean the camera lens for each measurement height. Consequently, no observable interference was seen on the camera due to condensed water. The measurement is shown in figure 6.13 and show similar behaviour as the results for the 1000 m a.G. sample shown in figure 6.12.

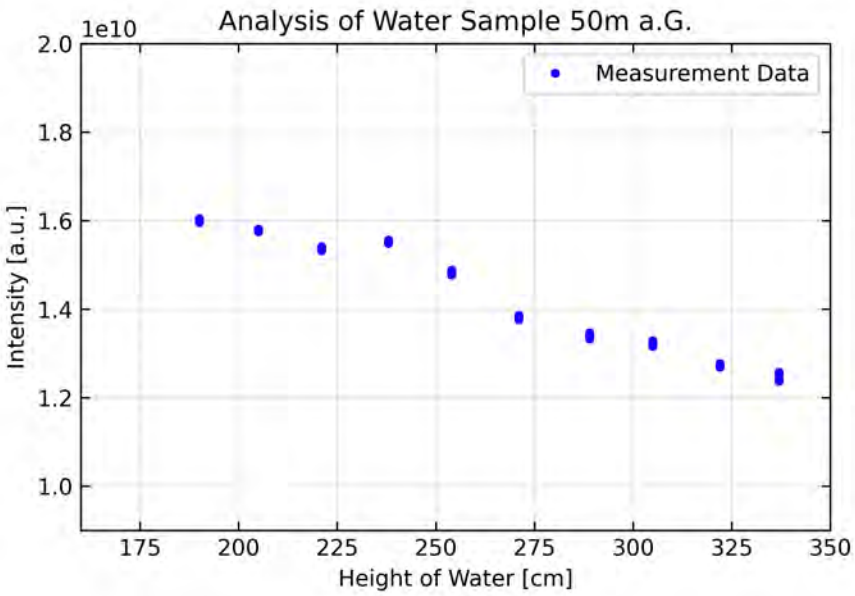

Fig. 6.13: Measurement of the first test of the water sample from 50 m a.G..

These measurements can be analysed with a Beer-Lambert fit, as introduced in chapter 2.6, to extract the attenuation length out of the measurement. As shown in the following figures 6.14, 6.15 and 6.16, the attenuation lengths are in the low meter scale. The values extracted by the Beer-Lambert fit are listed in table 3.

Sample	**Attenuation Length**
500 m a.G.	2.816 m
1000 m a.G.	5.215 m
50 m a.G.	5.522 m

Tab. 3: Listing of the attenuation lengths resulting out of the Beer-Lambert fit for the different samples. The sample from a depth of 500 m a.G. shows a signficantly lower attenuation length than the other samples. For more information refer to the text.

As apparent from the table 3 and figures 6.14, 6.15 and 6.16 the obtained attenuation lengths are in the low meter scale. These values can be compared to in-situ measured values of the attenuation length by the pathfinder line STRAW-a. As introduced in chapter 3.1, the attenuation length was measured at $27.7^{+1.9}_{-1.3}$ m for a wavelength of 450 nm and shows a significant difference to the measured value for the water samples [26].

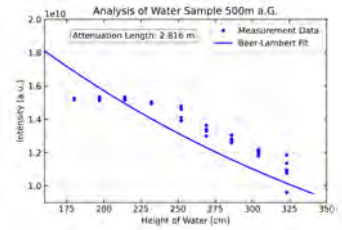

Fig. 6.14: The Beer-Lambert fit with the measurement of the 500 m a.G. sample.

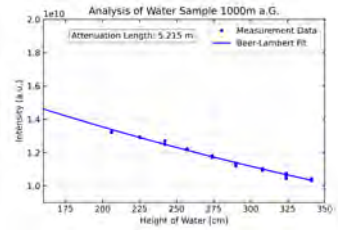

Fig. 6.15: The Beer-Lambert fit with the measurement of the 1000 m a.G. sample.

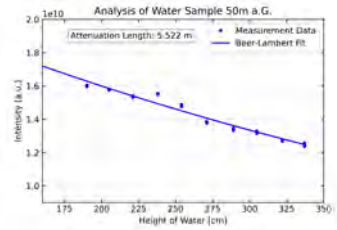

Fig. 6.16: The Beer-Lambert fit with the measurement of the 50 m a.G. sample.

The data of 1000 m and 50 m a.G. can be fitted quite well, whereas for the 500 m a.G. samples shown in the figure 6.14 the fit does not match the measurement accurately. As mentioned above, ice was identified in this sample, which could have caused a much higher absorption and scattering of the light beam inside the water in the sample pipe due to small ice crystals. To investigate such a possible effect, the data for high water levels in the sample pipe were excluded from the Beer-Lambert fit. The results for a selection of data points are shown in the figures 6.17, 6.18 and 6.19.

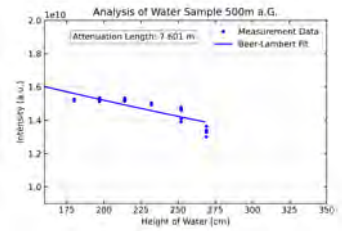

Fig. 6.17: The pre-selected measurement of the 500 m a.G. sample, wherein the heights above 269 cm were excluded.

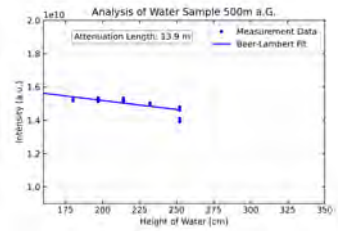

Fig. 6.18: The pre-selected measurement of the 500 m a.G. sample, wherein the heights above 252 cm were excluded.

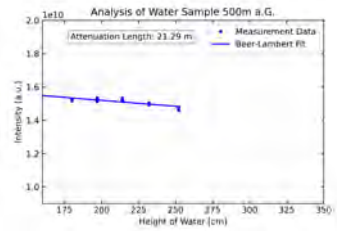

Fig. 6.19: The pre-selected measurement of the 500 m a.G. sample, wherein the heights above 252 cm were excluded as well as to measurement points at 252 cm.

The resulting attenuation lengths due to the exclusion of specific heights in the measurement of the 500 m a.G. samples are shown in the tabular 4.

Analyzed Data	**Attenuation Length**
500 m a.G. all measurement	2.816 m
500 m a.G.: 180 cm to 269 cm	7.601 m
500 m a.G.: 180 cm to 252 cm	13.9 m
500 m a.G.: 180 cm to partly 252 cm	21.29 m

Tab. 4: Listing of the attenuation lengths resulting out of the Beer-Lambert fit for the different selected data of the 500 m a.G. sample.

This difference in the obtained attenuation lengths depending on the selection of data shows the inconsistency of the measurement of the 500 m a.G. sample. Even though the attenuation length of the latest analysed pre-selected data seems expectable with a value of 21.29 m, this value can not be used as a result as the selection of the data is biased by the expectation of such a high value. Especially in comparison to the results of the other 1000 m a.G. and 50 m a.G. samples, it seems unlikely that this sample gives such higher attenuation length than the others.

Due to the inconsistent and unexpected results of the attenuation length of this first measurement of the deep-sea water samples, it was decided to test the setup with distilled water to investigate the capabilities of the experimental setup.

First Measurements of Distilled Water

To use the experimental setup for distilled water, the setup had to be cleaned after using the deep-sea samples. Therefore, the tank was cleaned properly, and the setup was flushed multiple times with distilled water before any measurements were made. The measurement procedure for distilled water does not change compared to the process for deep-sea water samples. Highly distilled water was used for the measurements, produced by an Elix Reference 5 [72]. The attenuation length of distilled water is expected to be very high at around one hundred meters [73].

The first measurement of distilled water is shown in figure 6.20 and consists only of three heights. This is caused by problems during the measurement, as for lower heights, the intensity became very low and oscillated. This may be caused by vibrations from unknown sources in the lab broadcasted to the measurement setup by mounting the setup on the ground and ceiling. Several lower heights were tried, as well as heights between the already measured heights, however, no usable data could be taken. The resulting attenuation length of the measurement is 23.348 m and is lower than expected compared to the value of around 100 metres [73].

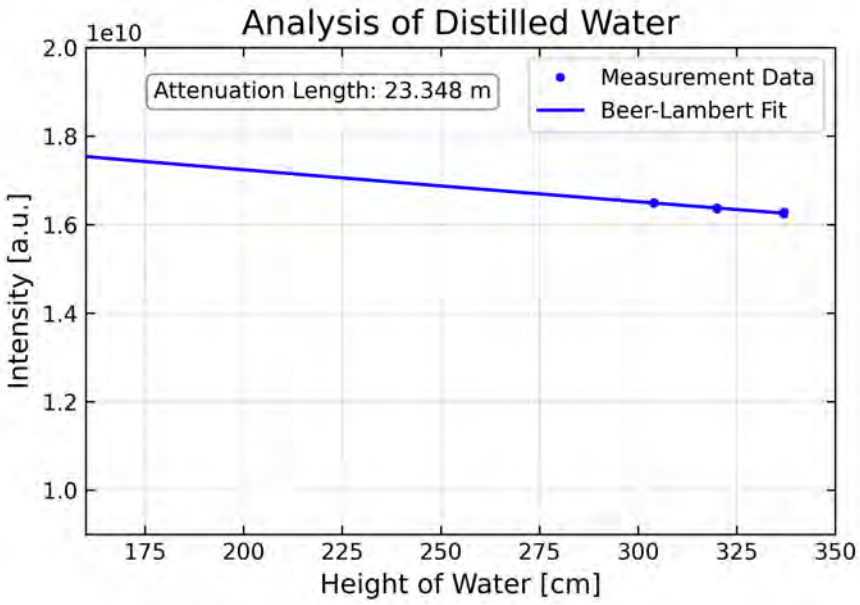

Fig. 6.20: Measurement of the first testing of distilled water.

Based on the first problematic measurement of distilled water, a second measurement was executed. The measurement and Beer-Lambert fit are shown in figure 6.21. In this measurement, no vibrations and oscillations in the intensity were identified. However, similar to the measurement of the deep-sea water sample from 500 m a.G. the data for high heights seem to be inconsistent in comparison to the data for lower heights. Due to this inconsistency, an analysis of selected data of this measurement was performed and is shown in figure 6.22.

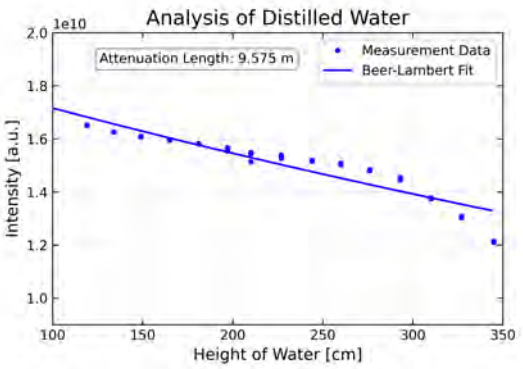

Fig. 6.21: The Beer-Lambert fit of the data of the second measurement of distilled water.

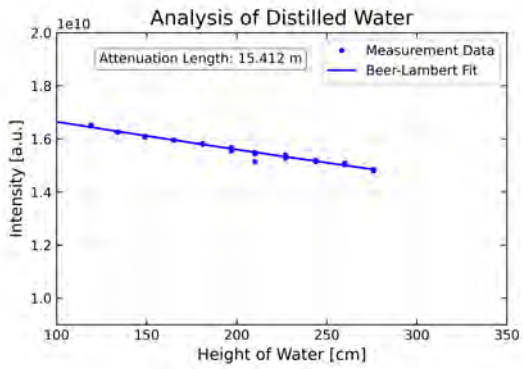

Fig. 6.22: The Beer-Lambert fit of the pre-selected data of the second measurement of distilled water. Data above 276 cm was excluded.

As visible in figures 6.21 and 6.22, the Beer-Lambert fit is more consistent with the measurement when data of higher water levels are excluded from the analysis. Still, the resulting attenuation lengths of 9.575 m and 15.412 m for the pre-selected data are far below the expected value of 100 m. This inconsistency also holds for the attenuation length 23.348 m (figure 6.20) of the first measurement of distilled water.

To get better statistics, more measurements of distilled water were performed. The third measurement is pictured in figure 6.23, and the resulting attenuation length is 43.15 m. As shown in figure 6.24, the fourth measurement of distilled water results in an attenuation length of 16.739 m.

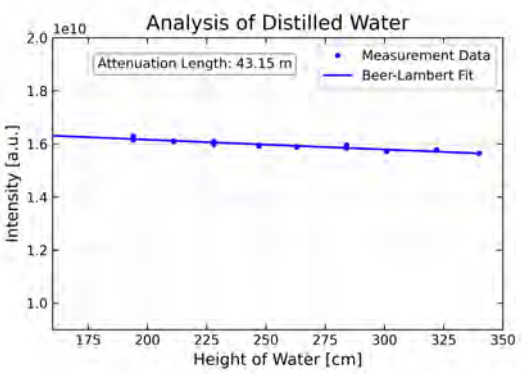

Fig. 6.23: The Beer-Lambert fit of the data of the third measurement of distilled water.

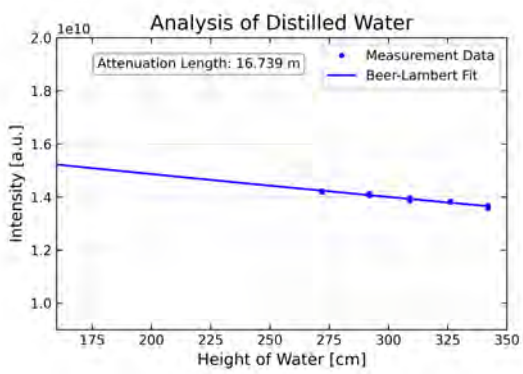

Fig. 6.24: The Beer-Lambert fit of the data of the fourth measurement of distilled water.

The results of the third and fourth measurements of distilled water are in the same order of magnitude as those of the previous measurements of distilled water. Since the results vary a lot and no trend in either direction is obvious, the reliability of the results is questionable. In table 5 the results of the measurement of distilled water are summed up.

Test Run	**Attenuation Length**
1	23.348 m
2	9.575 m
3	15.412 m
4	16.739 m

Tab. 5: Listing of the attenuation lengths resulting out of the Beer-Lambert fit for measurements of distilled water.

Since the measurements of distilled water were not performing as expected, the decision was made to test again the deep-sea water sample from 500 m a.G.. This sample was selected as the results of the first measurement were the worst by taking all data but looked promising after selecting a subsample.

Second Measurement of Water Sample (500 m a.G.)

During this measurement, again, massive fluctuations in the measured intensity were observed. These oscillations were so strong that, in the interim, no measurement was taken for one hour. The fluctuation acts in a way that the intensity varies for each taken picture between 10 % and 100 % of the roughly expected value, making any uncertainty calculations impossible. Such oscillations were most likely caused by some vibrations in the lab caused by other experimental setups. The measurements and the resulting Beer-Lambert fit are shown in figure 6.25.

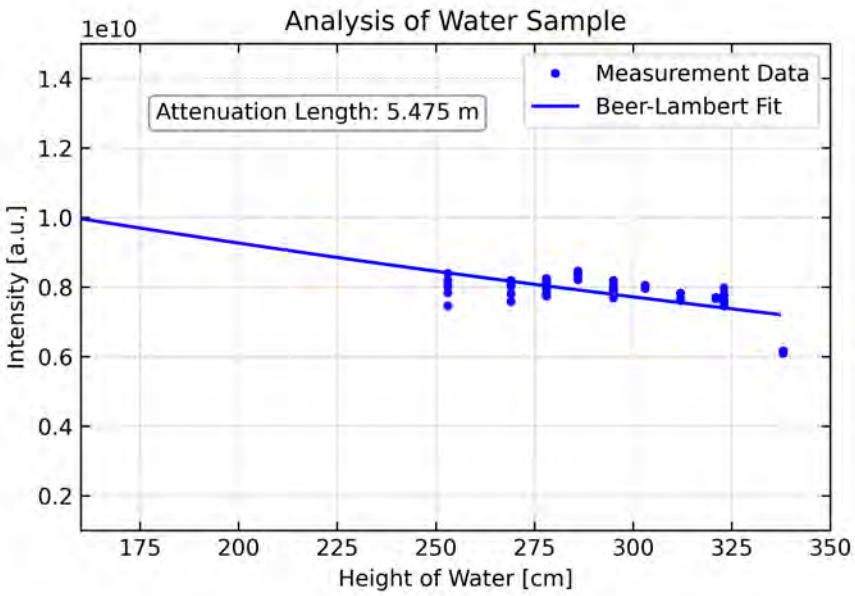

Fig. 6.25: The Beer-Lambert fit with the second measurement of the 500 m a.G. sample.

As seen on figure 6.25 the resulting attenuation length is 5.475 m. This value is in the same regime as the results of the first measurement from the other deep-sea samples and thus far lower than expected. Moreover, it can be seen in figure 6.25 that for the highest water levels, the measured intensity does not behave as the other measurement for lower water levels. Therefore, in figure 6.26, the measurement and the Beer-Lambert fit for excluding this maximal height are shown. The fitted attenuation length is 14.418 m, which is closer to the expected value of 28 m for 450 nm [26]. Still, it remains unclear why the measurement for the highest height needs to be excluded. Additionally, the fact that during the measurement period, no useful data could be taken for a while, introduces a human bias.

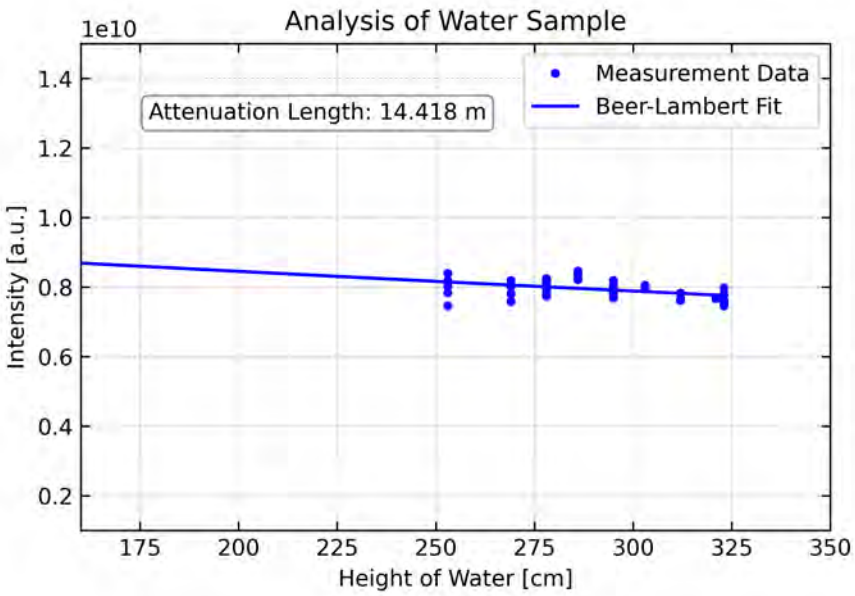

Fig. 6.26: The Beer-Lambert fit with the second measurement of the 500 m a.G. sample. Here, the measurement for the highest water level are excluded.

Based on the difficult measurements of the water samples and the distilled water, it was decided to investigate if any instrument could introduce the variations and inconsistencies seen in the measurements.

Characterisation Tests of the Experimental Setup

To exclude issues induced by the halogen lamp, the monochromator, the collimator or the mirror, a run with only the before-mentioned components was conducted. The sample pipe is only filled with air in this test. In figure 6.27, the intensity measured with the camera is shown over time.

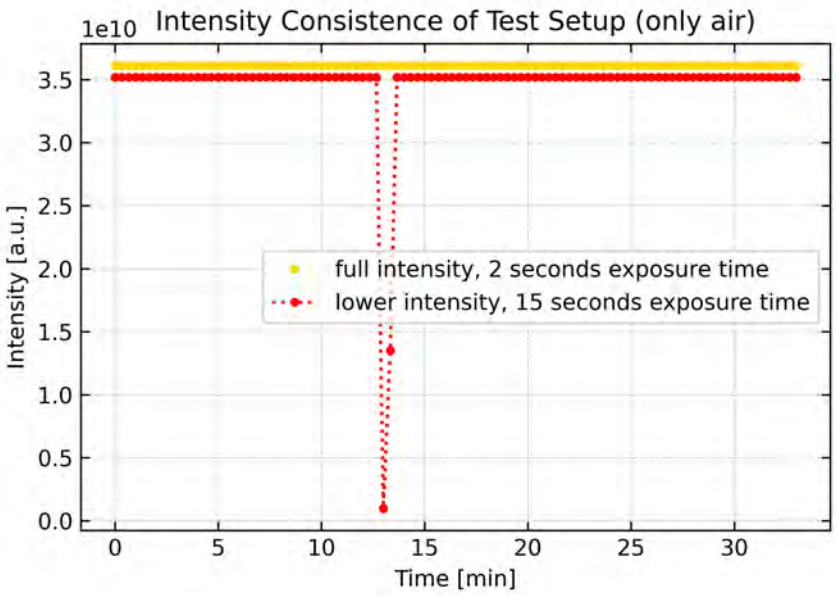

Fig. 6.27: The intensity over time for two different camera settings with only air in the setup. In yellow, the set intensity of the lamp is maximal, and the camera's exposure time is 2 s. In red, the intensity of the lamp is reduced to avoid camera saturation, which is set to 15 s of exposure time.

As displayed in figure 6.27, the intensity of the setup is constant over time. A readout error of the camera causes the drop in intensity for 15 seconds at minute 13. This camera error can not be identified as responsible for the strong oscillations measured in the previous measurements as it just occurred once within one hour, whereas the fluctuations were observed over a period of up to one hour. Thus, based on the previous measurements, it seems no components created these intensity variations.

Since the measurement of an empty sample pipe did not give any hints on the cause of the fluctuation in the measured intensity, in the next measurement, the sample pipe was filled with distilled water again to reattempt a long time measurement of the intensity over time. In figure 6.28, the measurements of the empty sample pipe and the filled one are depicted. The sample pipe is filled with water to the height of 338 cm.

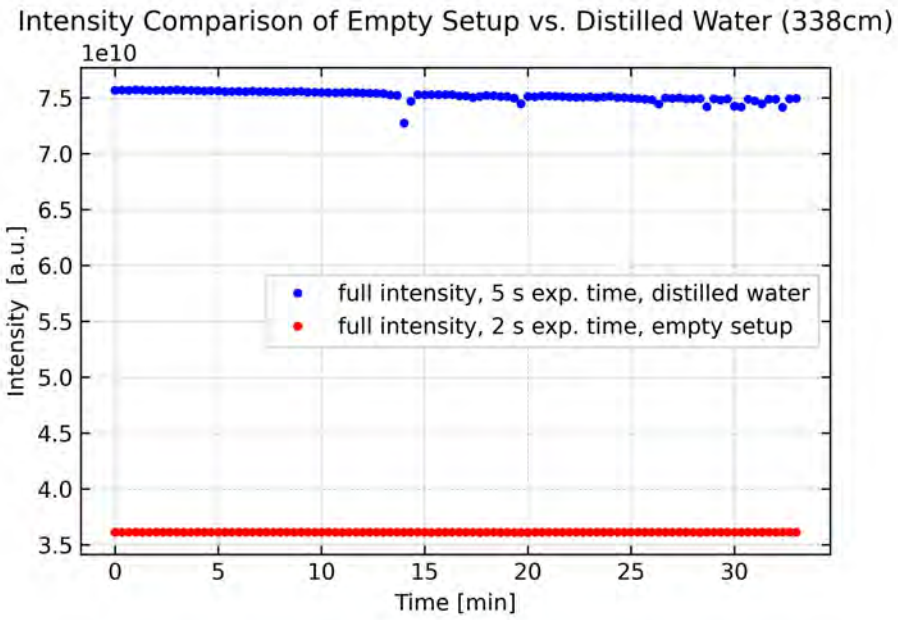

Fig. 6.28: The intensity over time for two different experimental settings. In blue, the data of the measurement with distilled water in the sample pipe (height of 338 cm) is shown, and the exposure time of the camera is 5 s. In red, the data of the empty sample pipe is pictured, wherein the exposure time is set to 2 s.

As seen from figure 6.28, the intensity for the measurement with the distilled water varies more than the run with the empty setup. Still, there were no intensity fluctuations similar to the previous measurements. Thus, it would appear that the setup doesn't have a component creating these fluctuations. Nevertheless, further investigations with distilled water have been performed to identify systematic errors.

Second Measurements of Distilled Water

During the second distilled water measurements, the execution of the measurements was adopted. To investigate the response and behaviour of the experimental setup, the intensity was measured while decreasing the height of the water level. Afterwards, the measurement was redone with the water level increasing. Additionally, the water was not released and exchanged with new water after the measurement. Instead, it was kept in the setup and tested multiple times over different days.

In the first measurement run, the water level was first decreased and then increased, and afterwards decreased again. As shown in figure 6.29, the resulting attenuation lengths vary depending on whether the water level was decreased or increased during the measurement. The attenuation lengths of the downwards measurements are 4.012 m and 4.475 m and thus are on the same level. In contrast, the attenuation length of the upward measurement is 1.363 m, which is significantly

below the values of the downward measurements. The intensity of the second downward measurement is clearly lower than for the first downward measurement, even though the setup and environmental parameters have not changed. One hypothesis to explain this difference is that impurities and pollution in the experimental setup swirled up during the upward measurement and then affected the intensity for the second downward measurement inside the sample pipe.

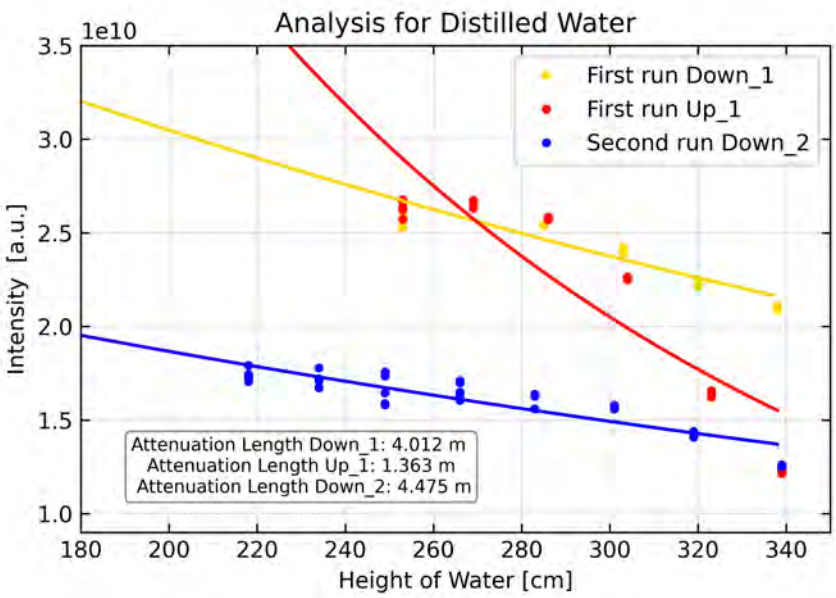

Fig. 6.29: The first measurement run of distilled water with adopted execution. The clear differences between the intensities of the first downward measurement (yellow) and the second downward measurement (blue) could be explained by impurities and pollution in the setup.

Based on the results of the previous measurement, a second measurement with new, fresh water was performed. As seen in figure 6.30, the measurements follow a similar behaviour as in the measurement before. Also, here, the intensity of the second run is lower than in the first run. Overall, the resulting attenuation lengths are lower than in the first measurement, as shown in table 6.

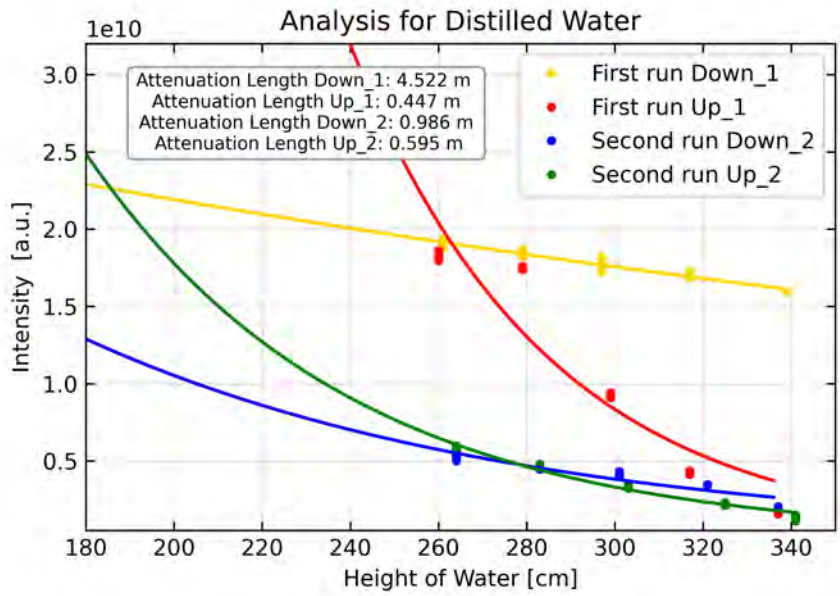

Fig. 6.30: The second measurement of distilled water with adopted execution.

Analysed Data	**Attenuation Length**
First Run Down	4.522 m
First Run Up	0.447 m
Second Run Down	0.986 m
Second Run Up	0.595 m

Tab. 6: Listing of the attenuation lengths resulting out of the Beer-Lambert fit for the different runs of measurement of distilled water.

To identify the source of the impurities and pollution in the setup, a third measurement the next day was performed. As pictured in figure 6.31, only downward data were taken in this measurement. It is visible that the attenuation lengths of this measurement got shorter than the measured attenuation lengths from the day before. For this measurement the attenuation lengths are 1.336 m and 0.602 m. The decrease in attenuation length indicates that the impurities and pollution in the pipe get worse over time, contaminating the measurement. The reactive behaviour of distilled water could cause this. So, it can be assumed that the distilled water is reacting with the pipe and tube materials of the setup, resulting in dissolving small particles, which leads to higher absorption and scattering inside the sample pipe over time.

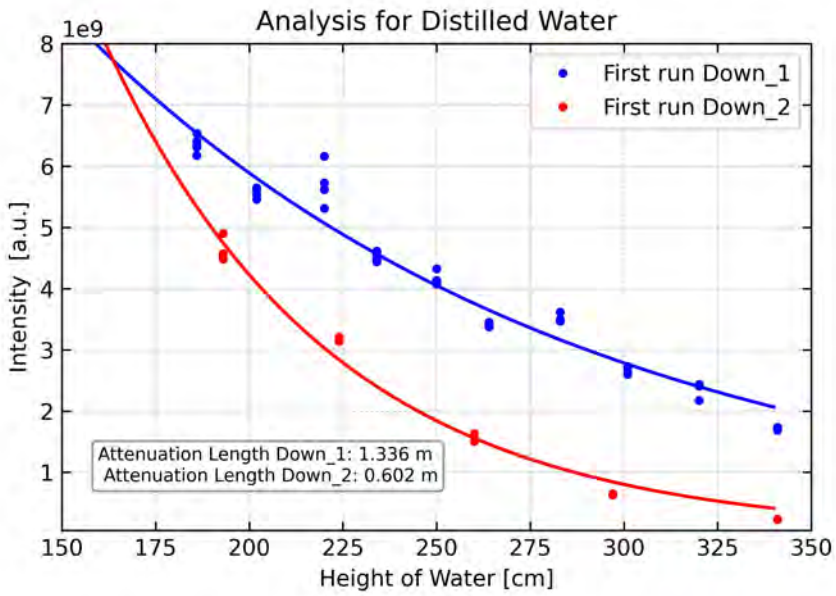

Fig. 6.31: The third measurement of distilled water with adopted execution.

To verify this hypothesis, a fourth measurement was executed two days after the third measurement. The resulting data is shown on figure 6.32 and confirms the hypothesis. The resulting attenuation length is 0.458 m, which is again lower than the measurement before.

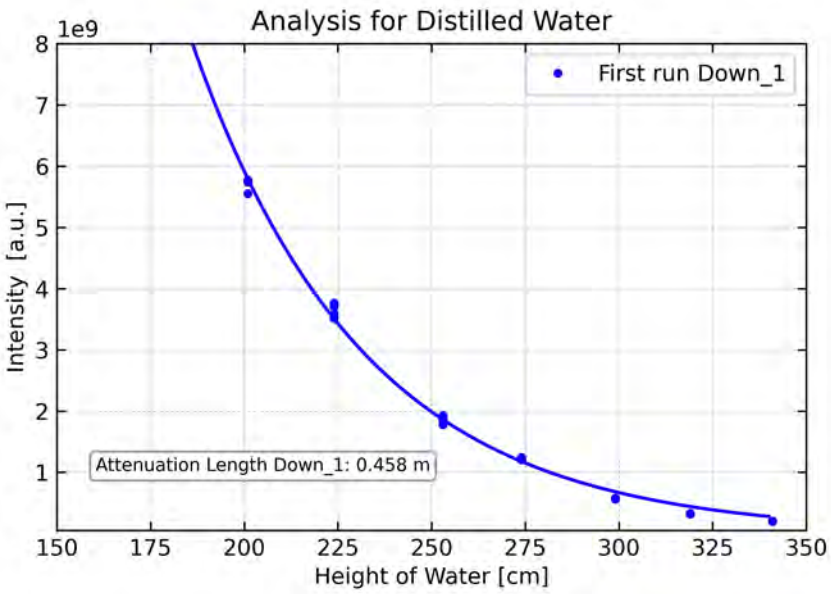

Fig. 6.32: The fourth measurement of distilled water with adopted execution.

Additional to the measurements, during inspections by the eye of the tank, the water in the tank showed deposits.

Conclusion about the Attenuation Length Measurements

During measurements, vibrations and oscillations within the experimental setup caused major obstacles, and efforts to mitigate and understand the source of these disturbances proved unsuccessful. Despite several attempts, the specific source responsible for these effects could not be identified, complicating the resolution of these issues. As the results are inconsistent within themselves and with comparable values no error estimation was performed.

The resulting attenuation lengths obtained from the measurements differed from the anticipated values, which were initially determined in situ at Cascadia Basin. Consequently, no measurements of the attenuation length of the water samples could be performed. To check the capability of the setup, it was attempted to measure the attenuation length of distilled water. This proved as unsucessfull as the transparency of the setup was observed to decrease over time when distilled water was retained within it. Unfortunately, the root cause of this behaviour remains elusive, wherein it is assumed that some components within the setup dissolve due to reaction with the distilled water.

Conversely, the measurements conducted for the JUNO experiment yielded consistent results that aligned closely with the anticipated values of the analysed scintillator. This outcome suggests that the experimental setup design is limited to analysing scintillators and cannot measure the attenuation length of water. Some preliminary results of measuring the scintillator

attenuation length are shown in figures 6.33 and 6.34. In these measurements, the scintillator Sasol LAB was tested at a wavelength of 430 nm, wherein the expected value of the attenuation length is at 17 m.

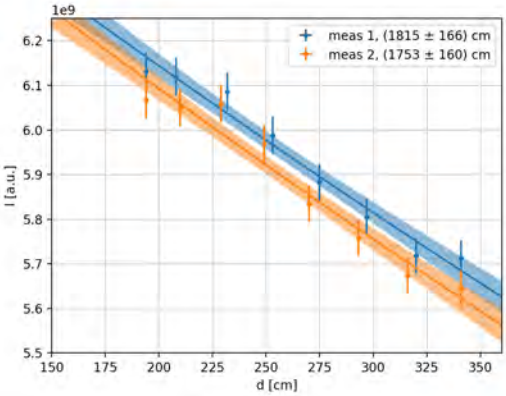

Fig. 6.33: Data and Beer-Lambert Fit of first preliminary measurement of the scintillator Sasol LAB at a wavelength 430 nm. Data taken and analysed by V. Rompel.

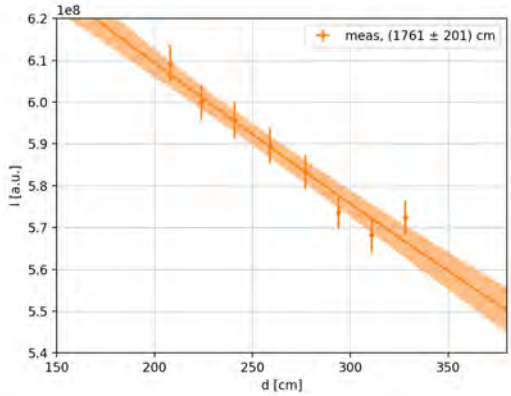

Fig. 6.34: Data and Beer-Lambert Fit of second preliminary measurement of the scintillator Sasol LAB at a wavelength 430 nm. Data taken and analysed by V. Rompel.

7 Oceanography Sensor Interface

As introduced in chapter 2.6, precise knowledge of the optical properties of the detector medium are key for event reconstruction and detector optimisation. Additionally, the ocean plays a crucial role in the climate and the atmospheric behaviour of the Earth. For the optical properties of the seawater at Cascadia Basin, several measurements have been conducted, some in situ and some in the lab, as it can be seen in chapters 3.1 and 6.2. Supplementary nanosecond light emitters will be hosted in the P-OMs and P-CALs to measure the attenuation in-situ. Environmental parameters at Cascadia Basin have been assessed by multiple CTD measurements as well as seafloor-based instrumentation. These measurements are designed to take data for a short duration and can not measure long-term developments over a height profile. Here, the P-ONE detector could provide a good opportunity.

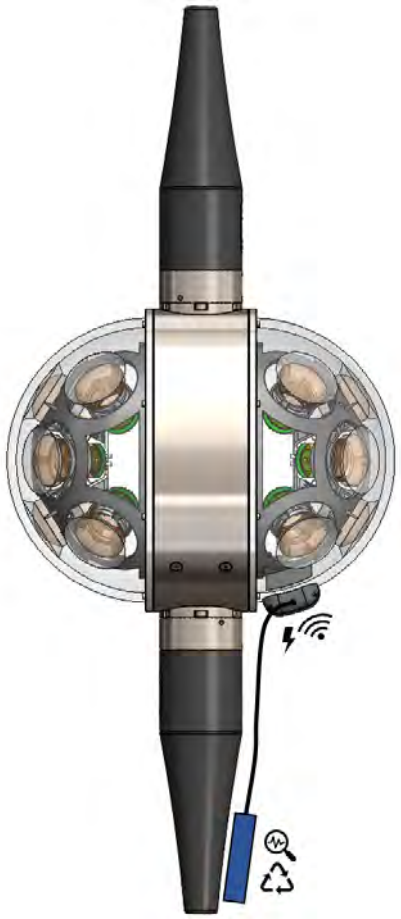

Fig. 7.1: Schematic sketch of the functionality and positioning of the Oceanography Sensor Interface.

As established in chapter 3 and 3.2, the neutrino telescope will provide a huge infrastructure which ranges from the seafloor one kilometre upwards and roughly covers the depths between 1600 m and 2600 m. The conceptional idea is to use the infrastructure of P-ONE to monitor environmental parameters over this height profile while receiving live data from the sensors. Thus, data like temperature, oxygen concentration, pH value and several other parameters could be monitored over a long period. The idea of this project is then to provide an interface capable of transmitting power and communication to the sensor and receiving data from the sensor. This interface should be designed as generic as possible to be usable for a wide range of environmental sensors. As shown in figure 7.1, the current design of the oceanography sensor interface is arranged in a P-OM using a free space between two PMTs. At this location inside the module, the devices for power transfer and communication are positioned, whereas, at the same location outside the P-OM receiver, devices for power transfer and communication are attached. The power transfer and communication from inside the module to the outside has to be done wirelessly. This design was chosen to avoid cable apertures through the module housing, as a failure of those would risk the integrity of the module. The Oceanography Sensor Interface should provide a wireless power and communication interface between two bidirectional devices, one located inside the P-OM and one attached to the outside of the glass hemisphere of the module. A cable connection to the environmental sensor is planned from the outside device. The sensor can then be positioned where the measurement is uneffected by

the P-OM and the mechanical stress during the deployment is minimal to avoid any damage or snapping off of the sensor or the outer device.

Potential sensors for the usage with the Oceanography Sensor Interface are the Oxygen Optode 4831/4831F [74], which is an oxygen sensor, the SBE 38 Digital Oceanographic Thermometer temperature sensor [75] or the DST CTD online sensor [76], which is capable of measuring conductivity and temperature. All these sensors have a low power consumption and are designed for operation in the deep sea. In the following chapters, the individual systems of the Oceanography Sensor Interface, like wireless power transfer and wireless communication, are introduced. Also, the current design for integrating the Oceanography Sensor Interface in the P-OM is elucidated, as well as a conceptional draft for a pressure housing for the outside devices. In the end, an outlook on the upcoming steps regarding development and testing is given.

7.1 Wireless Power Transfer

In general, there are two different types of wireless power transfer: coupling and radiative. The latter comprises methods like microwave, electromagnetic wave, and laser transmission. The coupling transmission type includes the magnetic field coupling as well as the electric field coupling. For the wireless power transfer system for the Oceanography Sensor Interface it was decided to used the magnetic field coupling. This transmission method fits the requirements of high efficiency transfer over a distance of a few centimetres best. The magnetic field coupling can be divided into two kinds of coupling, the electromagnetic inductive coupling and the magnetic resonance coupling. The simplified schematics of both methods are shown in figure 7.2 [77].

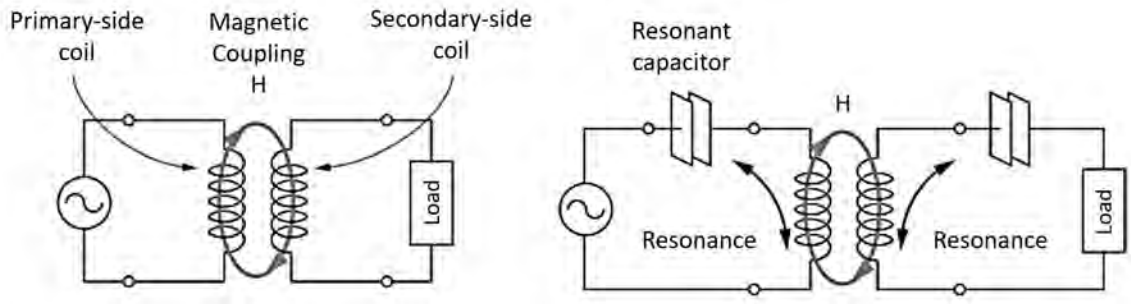

Fig. 7.2: Simplified schematics of a inductive coupling circuit and a magnetic resonance coupling circuit. Figure from [77].

The basic principle of both schematics is to couple both coils over a certain distance via the induced magnetic field. For the inductive coupling, the transmitter coil needs to be supplied with an alternating current, thus creating an alternating magnetic field. The receiver coil registers this alternating magnetic field, and the field induces an alternating current in the receiver coil. This current can then be used for the load on the receiver side and the wireless power transfer is accomplished. This principle also works for magnetic resonance coupling, but in this case, the circuit also contains a resonant capacitor. Hereby, the objective is to match the resonant

capacitor and coil on the transmitter side as well as on the receiver side in a way that a resonance between the capacitor and the coil is generated. Moreover, for this circuit to work as expected, the transmitter circuit and the receiver circuit need to be tuned so that the resonance frequencies match. For this, the load on the receiver side has to be selected and tuned very carefully, as already small changes on the receiver side can cause losses in efficiency and coupling stability [77]. Hence, the magnetic resonance coupling is more complex than the inductive coupling, but it can also transmit higher power with higher efficiency over distance than the inductive coupling system. A comparison of efficiency and transferred power between the two techniques is shown in figure 7.3 [77].

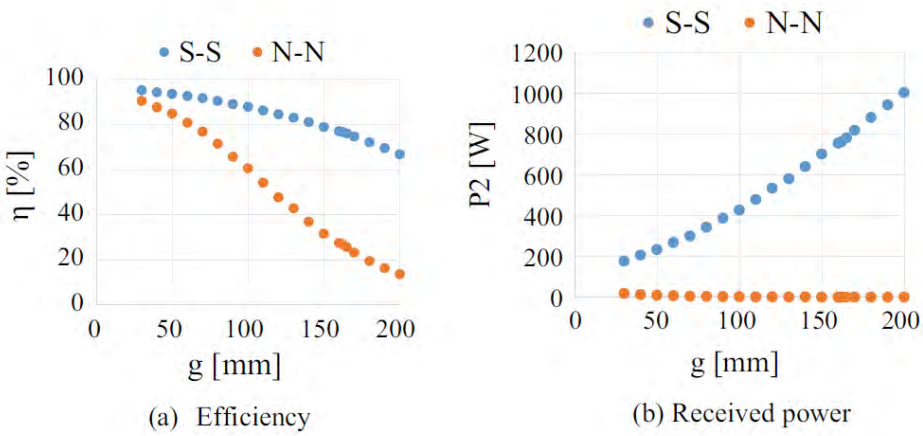

Fig. 7.3: Comparison of efficiency and transmitted power over distance of inductive coupling (N-N) versus magnetic resonance coupling (S-S). Figure from [77].

The values for distances between the coils and the transmitted power shown on figure 7.3 are higher than the requirements for the Oceanography Sensor Interface, but they illustrate the potential of magnetic resonance coupling in comparison to inductive coupling. Furthermore, lab tests were conducted with off-the-shelf coils designed for inductive charging. The coils were coupled via induction as well as magnetic resonance coupling. The results are shown in figure 7.4. The magnetic resonance coupling is more promising over distance than the inductive coupling. This coincides with the indications provided by figure 7.3.

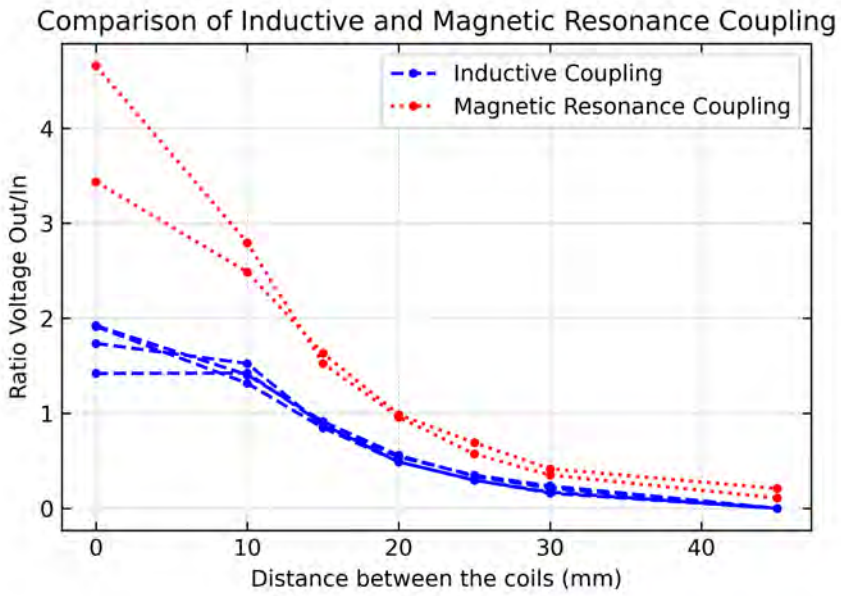

Fig. 7.4: Comparison of coupling ability for inductive and magnetic resonance coupling. Tested coils are off-the-shelf coils IWTX55R0DZEB8R9KF1 and IWTX5555DEEB100KF1.

As visible in figure 7.4, the coupling between the transmitter and receiver coil decreases strongly for higher distances, independent of whether the coupling is inductive or based on magnetic resonance. Different coil shapes and sizes have been tested to find promising candidates for this use-case. As a result of this, the focus went for printed circuit board (PCB) coils. Figure 7.5 shows the evaluation kit of different PCB coils used. In figure 7.6, the results for the coupling of the coils are displayed. It is apparent that the coils with the largest area can provide the best results in terms of coupling over distance. This is expected as the range of wireless power transfer depends on the effective surface of the coils, which is explained by the Neumann formula 7.1 [77].

$$L_m = \frac{\mu_0}{4\pi} \oint_{C1} \oint_{C2} \frac{\mathrm{d}l_1 \mathrm{d}l_2}{D} \tag{7.1}$$

Here L_m is the mutual inductance describing the coupling between the two coils. $\mathrm{d}l_1$ and $\mathrm{d}l_2$ express the line integrals of the winding of the corresponding coils and D is the distance between the two coils. As the PCB coils showed a better coupling performance than the coils tested before, in the following investigations, PCB coils were primarily used and analysed.

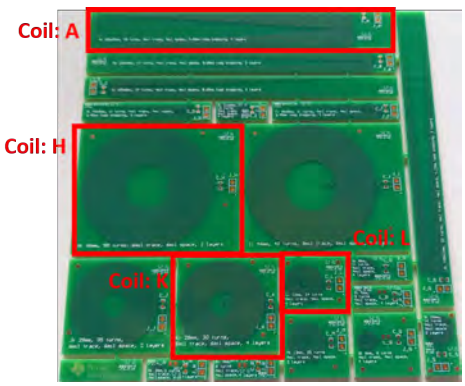

Fig. 7.5: Picture of the PCB coils. The tested coils are highlighted.

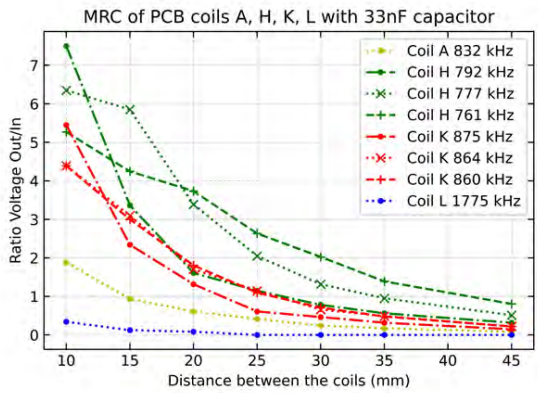

Fig. 7.6: Maximal coupling efficiency of PCB coils over distance.

One main requirement for the Oceanography Sensor Interface is that it should not affect the functionality of the PMTs in the P-OM. Especially it should be guaranteed that the PMTs are not affected by the power transfer. For this purpose effects of shielding on the coupling between the coils were investigated. To do so, mu-metal was used to shield the coils in several different configurations. For the different configurations, the distances between the correspondent coil and the shielding were changed. The results are shown in figure 7.7. The data indicates that shielding has a strong effect on the coupling between the coils, but more importantly, shielding should not be placed directly at the receiver coil. For the other shielding configurations in which the shielding is distanced to the receiver coil, the reduction in coupling is manageable.

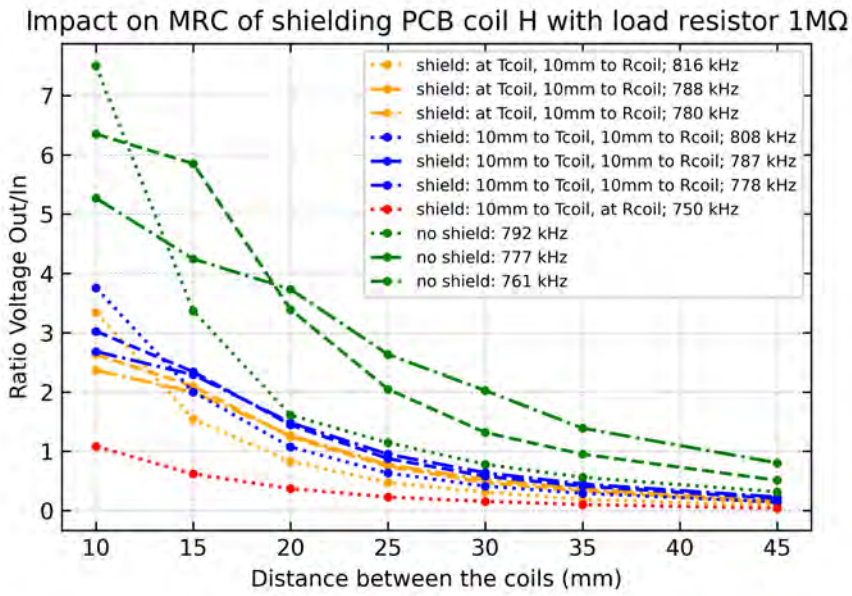

Fig. 7.7: Comparison of coupling ability for shielded and not-shielded coils. For the green data no shielding was applied, for the yellow data the shielding was placed in contact with the transmitter coil and with 10 mm distance to the receiver coil, for the red data the shielding was applied the other way around. For the blue data the shielding was placed in 10 mm distance to both coils.

In the next step the effect of the wireless power transfer on a PMT was measured. For this purpose a small testing setup was created, which is shown in figure 7.8. The goal of the set up was to investigate the impact of the wireless power transfer on the signal of the PMT depending on the distance of the power transmission system, orientation of the PMT regarding the power system and the frequency of the power transfer. The main findings of these tests are that the impact is mainly influenced by the excitation frequency of the coils, as pictured in figure 7.9. Also, the orientation of the PMT regarding the position of the coils has a minor impact on the PMT signal. The distance of the coils to the PMT has nearly no effect on the response of the PMT, at least for the range reasonable for the Oceanography Sensor Interface. The most important result of this test is that the frequency for the power transmission should not exceed a frequency of f = 7 MHz. Up this frequency, there was no effect on the PMT signal observable, wherein above the 7 MHz, a modulation of the signal of the PMT was visible. In figure 7.9, the maximal measured effect on the PMT signal is shown for a frequency of 16 MHz of the power system.

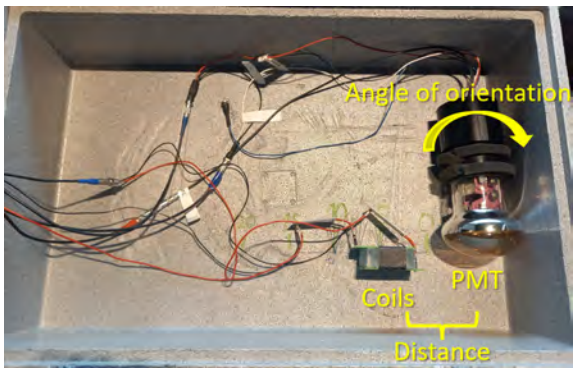

Fig. 7.8: Setup for testing the impact of wireless power transfer on a PMT signal, depending on distance, orientation of the PMT and frequency of the power system.

Fig. 7.9: Screenshot of the Oscilloscope measuring the frequency of the power system (pictured in yellow) and the signal of the PMT (pictured in orange).

The intial measurements and investigations indicated that developing a wireless power system with a high efficiency based on magnetic resonance coupling will require additional resources. Thus a partnership with the Fraunhofer Institute for Electrical Nanosystems (ENAS) was built up. This department is one of the highly experienced experts in the area of wireless power transfer and already developed several systems for industrial and research projects. Thus a cooperation between the TUM and the Fraunhofer ENAS was started and a framework was set up. It was settled that the Fraunhofer ENAS start simulation fo coils to match the following requirements, including simulations about the Q factor and the coupling factor. Moreover, they would provide electronics input for the power transmission system. The key parameters for the power system are listed in the following:

- Spacing between the coils is between 20 to 40 mm
- The transferred power should be between 2 to 5 Watt
- The overall efficiency of the system should be 60% minimum
- The frequency of the power transmission system has to be below 7 MHz
- On the receiver side an output voltage of 12 VDC respectively 5 VDC is required
- On transmitter side a voltage of 5 VDC respectively 24 VDC can be provided by the P-OM

Additional to the work mentioned above, the Fraunhofer ENAS sent an evaluation device. This device worked on 13.56 MHz and has an output power of around 2 watts. It was tested at TUM with a glass hemisphere of the P-OM to prove the conceptional idea of the Oceanography Sensor Interface. For this test, the boards were placed at the most probable position for the Oceanography Sensor Interface. The testing setup is shown in figure 7.10. The power transmission was successful and the coupling between the coils was stable. The voltage measured on the receiver

side is shown in figure 7.11. Also, the evaluation device was tested together with a PMT, and as expected, the power transmission system had a strong impact on the signal of the PMT, since it had a frequency above 7 MHz. Based on this knowledge the current development of the power transmission systems aims for an operating frequency of 6.78 MHz. At this frequency, it is expected to have no impact on the response of the PMTs. However, this will be confirmed once the first functional prototype is available.

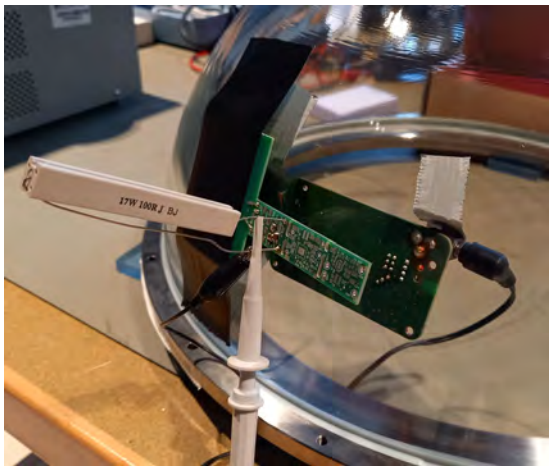

Fig. 7.10: Setup for testing the conceptional idea of the Oceanography Sensor Interface at the hemisphere of a P-OM with the evaluation device of the Fraunhofer ENAS.

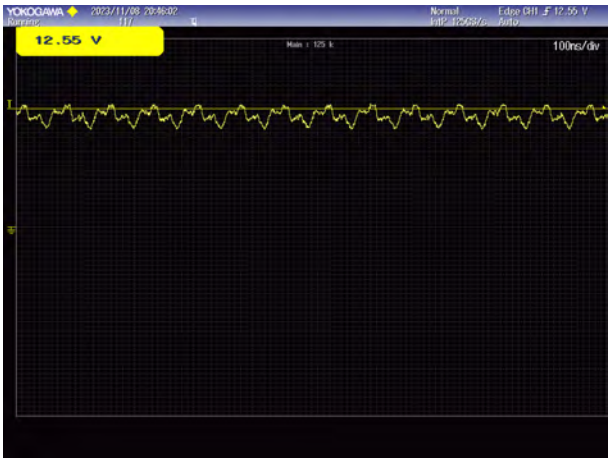

Fig. 7.11: Screenshot of the Oscilloscope measuring voltage of the power transmitted by the evaluation device from Fraunhofer ENAS.

The simulation results from the Fraunhofer ENAS show that a coil with bending diameter of 361 mm should contain 5 windings with a 2 mm width of trace and a 1.65 mm spacing between the single traces. This results in a Q factor of 255 and a coupling factor of $k = 0.25$ for a distance of 25 mm between the coils. Hereby the outer coil is bent with a diameter of 411 mm. These simulation results lead to a theoretical efficiency of the power transfer of around 96.9% under the assumption that the load on the receiver side is perfectly adapted. The efficiency can be calculated with the following formulas: 7.2 and 7.3. Hereby α is the adapted load factor.

$$\alpha_{\text{opt,eff}} = \sqrt{1 + k^2 \cdot Q_{1,1} \cdot Q_{1,2}} \tag{7.2}$$

$$\eta_T = \frac{\alpha}{1 + \alpha + \frac{(1+\alpha)^2}{k^2 \cdot Q_{1,1} \cdot Q_{1,2}}} \tag{7.3}$$

Additionally, the efficiency of the electronics on the transmitter and receiver side has to be considered to get the overall efficiency. For this type of electronics, schematics were provided by the Fraunhofer ENAS, and a PCB based on this information will be developed in the next step.

7.2 Wireless Communication System

Next to the wireless power transfer system, a system for a wireless communication system is necessary for the Oceanography Sensor Interface. The mandatory requirement for this system is the ability to transmit the data of the sensor outside the P-OM to a receiver device inside of the module. Additionally, the capability of sending commands to the sensor to adjust, for example, the sampling rate, would be a nice feature. Furthermore, the energy consumption of the communication system should be low to be able to provide as much power as possible to the sensor if necessary.

Based on investigations already performed by ONC, the systems Bluetooth Low Energy (BLE) and WiFi seem to be good candidates to satisfy the requirements set. Such systems can be used as there will be no water between the transmitter and receiver devices and hence no disturbances are expected caused by the deep sea environment. For the first conceptional tests, two evaluation boards from Arduino were ordered. The MKR WIFI 1010 [78] and UNO WIFI REV2 [79] are both capable of communicating via BLE and WIFI. Both boards can be programmed via the IDE Arduino software [80]. In the first testing phase, a TMP117 temperature sensor was connected to an evaluation board, and the communication between the board and a smartphone, which is capable of BLE and WIFI communication, was setup. It was achieved to implement communication between the board and the smartphone via BLE, where the data of the TMP117 sensor were sent automatically from the board to the smartphone. Also, communication could be set up via WiFi, but the system turned out to be more complicated due to the communication protocol in this state of investigation.

The development of the wireless communication system was aided by an expert in electronics at the physics department at TUM. C. Seifert from the central technology lab (ZTL) was able to set up a first functional communication system. The system is running on BLE, wherein the transmitter and receiver device are able to communicate and transmit sensor data. The next step is now to merge the communication system with the wireless power system and develop the first version of a PCB containing all the electronics required for the system.

7.3 Integration in Optical Module

Both systems, for power transfer and communication, need to be implemented in the design of the P-OM. For all parts located inside the P-OM an inner mounting is under development and will be introduced in the following. For the components outside the P-OM a outer housing will be designed, wherein the requirements for this housing and a preliminary design is shown in the following.

Inner Mounting

The inner mounting should be designed to fix the positions of all parts of the Oceanography Sensor Interface, which are located inside the P-OM. The components are the transmitter coil for the power system, the antenna of the BLE communication system and the PCB carrying all electronics required for the system. Hereby, the transmitter coil needs to be positioned as close to the glass hemisphere as possible to minimise the distance between the coils of the power transmission system and optimise the transfer. Also, the antenna for the communication system should be arranged close to the glass for the same reasons. The PCB should be mounted in a way that it is still accessible after integration of the housing so that the cable connection to the mainboard can be easily linked during the assembly of the whole P-OM. Additively the PCB could be mounted to the housing after it was screwed into position and also exchanged if any problems occur during the test before deployment. In general, the design has to take into account that all components need to withstand a shock and vibration test to make sure no parts get loose during shipment and deployment of the P-ONE-1 line and damage any other components in the module. As already introduced in chapter 7 the place of the Oceanography Sensor Interface inside the module would be one of the cutouts in the frame of the modules. Hence the shape of the housing will be predefined by this. A first prototype of the inner mounting is shown in figures 7.12 and 7.13. It can be seen that the housing has mounting bars at the side which can be screwed to the mounting holes in the frame. Additionally, the mounting bars are designed to fix the housing spring loaded to the frame so that the power transmission coil gets pushed towards the glass hemisphere to minimise the distance of the coils and fix the coil in the correct position. This is achieved by the frame-like structure on the outwards-looking side of the housing, which is adjusted to the size of the coil as visible in figure 7.12. Supplementary, the transmitter coil will be glued to the glass to ensure exact positioning of the coil. On the inner side of the housing, there are screw slots for mounting the PCB with the electronics to the housing. On the side of the housing there is a cable notch to connect the coil with the PCB on the inner side.

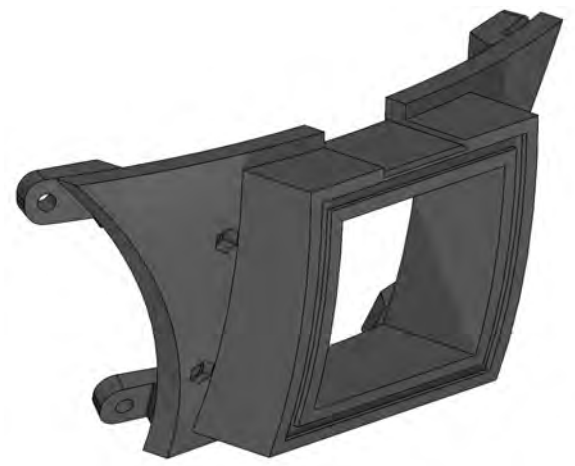

Fig. 7.12: Technical drawing of the outside of the inner mounting of the Oceanography Sensor Interface.

Fig. 7.13: Technical drawing of the inside of the inner mounting of the Oceanography Sensor Interface. Design provided by C. Spannfellner.

Outer Housing

For the outer housing, the requirements are more complex, as it will be arranged outside the P-OM and, therefore, must be resistant against the hydrostatic pressure of up to 270 bar in the deep sea. The outer housing has to comprise the receiving coil of the power system as well as an antenna of the BLE communication system. Additionally, it has to include the electronics of both systems and a sealed cable outlet, which enables the cable connection to the sensor as it will be attached to the backbone cable of the mooring line. Also, for this housing, a requirement is that both the coil and the antenna for the wireless systems are placed as close as possible to the glass hemisphere to guarantee a good transmission as discussed previously. The development of the outer housing is currently ongoing, and figures 7.14 and 7.15 show the first stage of development shown. This design is not the final version since it hasn't been tested to withstand the environment of the deep sea. The concept provides a main part of the housing, which is designed to host the coil, the antenna and the PCB inside. As shown in figure 7.15, the components can be slotted in the designated notches. Once all components are mounted in place, the main part of the housing gets sealed with a closure part of the housing, which can be screwed to the main part and has a cable breakthrough for the cable connection to the sensor.

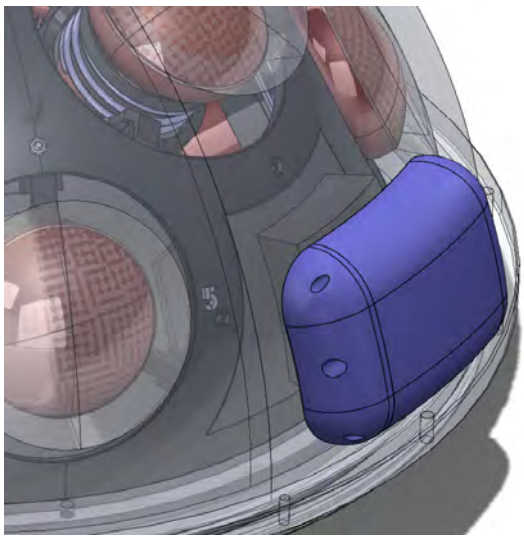

Fig. 7.14: Conceptional design of the outer housing attached to the P-OM. The housing pictured in blue colour.

Fig. 7.15: Conceptional design of the outer housing with its main part and the closure.

7.4 Outlook for the Oceanography Sensor Interface

One of the major next steps for the Oceanography Sensor Interface is the design of the PCBs for the electronics combining both the input from Fraunhofer ENAS and the BLE communication system. Parallel the coils for the power transfer have to be ordered. After all components are available a first testing phase should be started to test the general concept and design of the Oceanography Sensor Interface. After the functionality of the systems is proved, a second test can be performed to test the impact of the Barnacle on the PMTs in the module. Therefore the adapted OMCU setup at TUM will be used to test a whole integrated hemisphere with the Oceanography Sensor Interface.

A Appendix

A.1 Coating Procedure of PMTs

	Description	Settings	Pictures
1	Prepare the PMTs for coating: Short the Pins of the PMTs to 4 cm. Put all PMTs in the "Drying Station for finished PMTs". Make sure all PMTs are clean at the neck where the coating is applied on.	For cutting the Pin use a side cutter For cleaning the PMTs use Isopropanol	 Shorten the pins to a length of 4 cm
2	Prepare the coating: Pour the components for the coating from the 5 liter storage container in the "Bath container for coating"	Use Plastic 70 Super & Thinner 70 Ratio 1:1 = 350ml : 350 ml In total 700 ml of coating	
3	Coat the PMTs: Take a PMTs by grapping it at the fotocathode from the "Drying Station for finished PMTs". Dip the PMT into the coating with the Pins looking downwards until the neck of the PMT is completly in the coating. Dip the PMT for 5 to 10 seconds. Then get the PMT out of the coating and drip of the coating over the "Bath container for coating" for 5 to 10 seconds and put the PMT in a hole of the "Drying Station for coated PMTs".	Watch out that no coating gets on the fotocathode Dip for 5 to 10 seconds Drip of for 5 to 10 seconds	 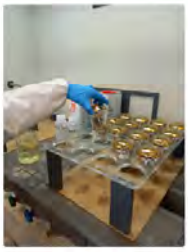

Fig. A.1: Coating Procedure first part.

4	Drying of the coated PMTs: Let the coated PMTs dry 20 minutes until they are ready for the removement of the coating from the Pins.	Close the Ventilation Hub for the drying process, but keep a small slot open, so that the air can ventilate. Drying duration: 20 minutes	
5	Control coating of the PMTs: The coating is fluoresence to UV-light. Control the coating by using a UV-flashlight. The complete neck of the PMT needs to be covered, also the fotocathode must be free of coating		
6	Prepare solvent for cleaning the Pins: Fill the Thinner 70 in the "Bath container for pin cleaning".	Use pure Thinner 70 Fill in 500 ml	
7	Clean the Pins from coating: For soldering the uBase on the PMTs the Pins must be free of coating. Take a PMT from the "Drying Station for coated PMTs" and dip it with the Pins in the "Bath container for pin cleaning". Watch out that only the pins are dipped in the Thinner. Keep the PMT for 15 seconds in the Thinner, while swinging the PMT careful to make sure the coating is removed properly. Then put the PMT in the "Drying Station for finished PMTs".	Grap the PMT at the top at the fotocathode Don´t dip any part of the glass of the PMT in the Thinner	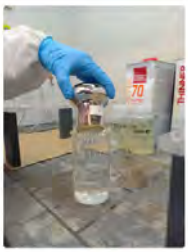 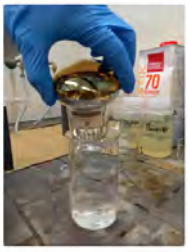

Fig. A.2: Coating Procedure second part.

8	Drying of cleaned pins: Let the cleaned pins dry out for 30 minutes. After that the finished PMTs can be removed from the Ventilation Hub.	Drying duration: 30 minutes	
9	Control removement of coating on pins: Check the removement of the coating from the pins by using the UV-flashlight. There should be no fluoresence on the pins, but on the neck of the PMT.		
10	Storage of coated PMTs: After removing the finished PMTs out of the Ventilation Hub they can be stored the way they were stored before. Make sure the PMTs are only touched with gloves after coating. Mark the box of the PMTs with "coated".	Use gloves for touching the coated PMTs	
11	Quality Control of coated PMTs: Check the coated PMTs according to the Quality Control protocol. If all PMTs passed the Quality Control, mark the Box with "QC ✅".	Use gloves for touching the coated PMTs	
12	Marking coated PMTs: After the quality control the PMT should be marked by painting the bottom part of the PMT-neck with black Edding.	Mark PMT with black Edding	

Fig. A.3: Coating Procedure third part.

A.2 Procedure of Gel Pad Production

	Description	Additional Information	Pictures
1	Cleaning: Use Isopropanol to clean the table, both mold parts, the precision scale, the stainless steel spoon/spatula, the stirring device, and the PMT.		
2	Preparation of the coating gel: Pour the exact amount of the A and B components into one small plastic cup. You can also use a spoon for a more precise measurement. Mix them for ~2min with a clean spoon/ spatula.	use **Elastosil RT 601** ratio A:B = 9:1 **9 g** of the **A**- and **1 g** of the **B**-component (= 10 g in total) *Your lab partner can do step 5 parallel.*	
3	Preparation of the main optical gel: Pour the exact amount of the A and B components into one large plastic cup. You can also use a spoon for a more precise measurement. Mix them for ~2min with a clean spoon/ spatula.	use **Silgel 612** ratio A:B = 3:2 **114 g** of the **A**- and **76 g** of the **B**-component (= 190 g in total) *Your lab partner can do step 6-8 parallel.*	

Fig. A.4: Procedure of Gel Pad Production first part.

4	Degassing the main optical gel: Place an electric stirring device in the cup of gel, switch it on and put the cup into a vacuum chamber. Leave it for ~3min until the gel looks more transparent, then switch of the vacuum pump and slowly let air into the vacuum chamber. Repeat this step if the gel still contains bubbles. During degassing the gel never gets as transparent as depicted in the last picture. Only after turning it off and letting the air into the chamber you can see such a result.	*You can help your partner with step 6-8 while you wait for the gel to degas.*	 degassing set up gel starts to bubble during degassing gel becomes more and more transparent after ~3min the gel is transparent bubble free gel after degassing process

Fig. A.5: Procedure of Gel Pad Production second part.

5	Preparation of the mold: Screw the filling tube and the PMT holding device to the upper part of the mold.		
6	Coating of the mold: Apply a **thin layer** of coating gel onto the inner surfaces of the mold using your fingers. Use less gel at the beginning and build the gel layer up. Make sure **no bubbles** appear on the mold surface.	Wear a second layer of gloves over your first layer during this process; throw the second layer away after you are finished with this step.	
7	Alignment of the PMT in the mold: Place the PMT into the holding device and upper mold part. Align it using a spacing ring between the table and the upper mold part. Push the PMT down to the table and secure its neck with a tape. Help each other to make sure it doesn't slip.		
8	Mold assembly: Put the two mold parts together and **align** them with the two long alignment screws. Seal it with three clamps. Make sure the clamps are set as tight as possible and **leave some space next to the filler tube**.		

Fig. A.6: Procedure of Gel Pad Production third part.

9	Gel injection: Suck up the gel from the plastic cup with a 100 ml syringe. Do this carefully without haste to avoid inducing bubbles. Tuck the tip of the syringe into the filling tube and hold it **vertical**. **Slowly** push the gel out of the syringe and ensure the gel fills up evenly from the bottom to the top of the mold. Once the gel comes up and becomes visible around the PMT, stop pushing gel into the mold. The gel must not overflow. Remove the syringe by pushing the red ring of the filler tube down and pull the syringe out **carefully**.	Suck up approximately 90 ml. 60 ml of gel can be filled in any case. Take a closer look on the gel level once you exceed the 60 ml. *Include your lab partner in this step!*	 filling the gel into the mold
10	Cleaning: Clean the syringe and all used devices and store them properly.	You can use a piece of the wipes and a cotton swap to clean the tip of the syringe.	
11	Curing: Let the freshly poured gel pads rest for **24h** at room temperature.		

Fig. A.7: Procedure of Gel Pad Production fourth part.

12	Disassembling the mold: After curing, remove the three clamps and holding device. Take the end of a spoon or a screwdriver, place it one after the other between the upper and lower mold part. Carefully lever the upper part of the mold upwards. Remove the upper mold part and leave the alignment tool on the upper part of the mold.	*Disassemble two molds simultaniously with your lab partner.*	
13	Removing the gel pad: Take the cutting wheel and place it on the lower mold part, be sure that the three feet of the wheel really sit on the sides of the mold. Cut off the gel rim by pushing the wheel down and turning it around. Lift and loosen the edge of the gel pad with your fingers and carfully remove the gel pad by levering the PMT out of the mold.	*Remove two gel pads simultaniously with your lab partner.*	

Fig. A.8: Procedure of Gel Pad Production fifth part.

14	Storage: Wrap the PMT-gel pad assembly with plastic wrap to prevent dust from settling on the gel pad.		
15	Cleaning: Clean the mold parts, clamps, screws and table from any gel residuals and store them properly.		

Fig. A.9: Procedure of Gel Pad Production sixth part.

A.3 Procedure of PMT Integration

	Description	additional Information	Pictures
1	Cleaning: Use Isopropanol to clean the table, the precision scale, the stainless steel spoon/ spatula, the stirring device, and the glass of the hemisphere right where the gel pad will be placed.		
2	Preparation of the interface gel: Pour the exact amount of the A and B components into one small plastic cup. You can also use a spoon for a more precise measurement. Mix them for ~2min with a clean spoon/ spatula.	use **Elastosil RT 601** ratio A:B = 9:1 **13.5 g** of the **A**- and **1.5 g** ot the **B**-component (= 15 g in total) *Your lab partner can do step 4 parallel.*	
3	Degassing the interface gel: Place an electric stirring device in the cup of gel, switch it on and put the cup into a vacuum chamber. Leave it for ~3min until the gel looks more transparent, then slowly let air into the vacuum chamber. Repeat this step if the gel still contains bubbles. To open the chamber, pull the red mat upwards carefully to avoid knocking over the gel cup. Some bubbles may still remain on the surface of the gel. Pop them with the end of the cotton swabs.	Sometimes it can be useful to repeat degassing without the stirring device.	 gel starts to bubble during degassing after ~3min the gel becomes more transparent

Fig. A.10: Procedure of PMT integration first part.

4	Preparation of the Hemisphere: Clean the spot where the Gel Pad will be placed with Isopropanol. Align the hemisphere on the stand with a spirit level. Insert the small plastic plate between the ring and the hesmisphere stand to align the hemisphere by turning the screw.	Make sure the spirit level sits properly on the frame.	
5	Applying the interface gel: Draw up a small syringe **slowly** and **carefully** to **prevent inducing any bubbles** and inject 7 g gel onto the center of the glass surface equally careful. Read the amount of gel from the gel level in the syringe and hold it **perpendicular**. If there still appear some bubbles: remove them by popping the bubbles with the other end of a cotton swab.	Suck up approximately 10 ml. Inject **7 ml** onto the glass surface. *In the mass production scenario your can split step 5 and 6. One person injects the gel and one integrates the PMTs.*	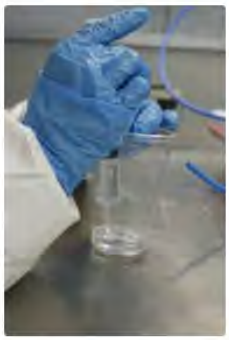

Fig. A.11: Procedure of PMT integration second part.

6	Integration of the PMT: Place the PMT with gel pad into the alignment device and hold the PMT upside down on its neck. **Carefully** insert the PMT and gel pad with the holding structure in the frame. After all three feet of the holding structure rest in the frame, lower the PMT slowly until it touches the gel. Do **not add additional pressure** other than the PMTs own gravitational force! ⚠ If you integrate a PMT with uBase, pay attention to the orientation of the uBase. The connectors of the uBase have to face towards you.	Make sure you hold the PMT and holding structure both in your hand, it can easily slip out. The PMT must be held **perpendicular** to the glass of the hemisphere already while inserting it.	
7	Cleaning: Clean the syringe and all used devices and store them properly.	You can use a piece of the wipes and a cotton swap to clean the tip of the syringe.	
8	Storage: Place a plastic wrap over the hemisphere.		
9	Curing and Applying the Lock-Mechanism: Let the interface gel cure for 24h. Remove the alignment tool and place the collar, spring, and lock of the holding structure on the neck of the PMT. Lock it in place by pushing the lock down and turning it until it is placed under the extensions in the frame.		

Fig. A.12: Procedure of PMT integration third part.

List of abbreviations

CMB Cosmic Microwave Background 2

LIGO Laser Interferometer Gravitational-Wave Observatory 3

CC Charged-Current 5

NC Neutral-Current 5

PMNS Pontecorvo-Maki-Nakagawa-Sakata 6

CNB Cosmic Neutrino Background 10

PWN Pulsar Wind Nebulae 12

SNR Super Nova Remnant 12

AGN Active Galactic Nuclei 13

GRB Gamma Ray Burst 13

DOMs Digital Optical Modules 15

PMT Photomultiplier Tube 15

Baikal-GVD Baikal Gigaton Volume Detector 16

P-ONE Pacific Ocean Neutrino Expermient 17

NEPTUNE North East Pacific Time-series Underwater Networked Experiments 18

ONC Ocean Networks Canada 18

TTS transit time spread 23

TUM Technical University Munich 28

ROV Remotely Operated Vehicle 52

a.G. above ground 52

PCB printed circuit board 77

BLE Bluetooth Low Energy 82

List of Figures

1.1 The plane of the Milky Way galaxy in photons and neutrinos. 1
2.1 Schematic of Cherenkov light. 6
2.2 Ilustration of the signature topology for neutrino interaction types with matter. . 8
2.3 Estimated neutrino flux origination from a variety of sources. For more information on the latter, refer to the text. Especial gratitude goes to F. Henningsen for providing the figure. 10
2.4 Schematic of the location of neutrino telescopes on the Earth. 17
3.1 Schematic of the preliminary P-ONE detector design. 18
3.2 Plot of the results for the attenuation length of the STRAW-a pathfinder mission at Cascadia Basin. 19
3.3 Conceptional drawing of the P-ONE-1 line. 20
4.1 Conceptional drawing of the P-OM. 22
4.2 Schematic structure of a PMT. 23
4.3 Picture of a coated PMT under UV-light. 24
4.4 Plot for the dark rate median and its standard deviation plotted against the position of the PMTs in the setup. 27
4.5 Plot for comparison of the median dark rate and its standard deviation of the effected PMTs. 28
4.6 Picture of the gel pad production site in the clean tent. 29
4.7 Picture of the self-constructed tables for the integration of the hemisphere of the P-OM. 29
4.8 Picture of an assembled mold. 29
4.9 Picture of an integrated PMT with the alignment tool still in position. 30
4.10 Picture of a prototype hemisphere of a P-OM with eight integrated PMTs from the inside. 32
4.11 Picture of a prototype hemisphere of a P-OM with eight integrated PMTs from the outside. 32
4.12 Picture of one integration table. 33
4.13 Schematic of the planned shift system for the gel pad production and PMT integration. 33
5.1 Graphic of required latent heat for phase changes in water. 37
5.2 Theoretical salinity profiles of two different hypothetical locations in the open ocean with different latitudes. 39
5.3 Graphic of the percentages of dissolved gasses in different compartments on Earth. 40
5.4 Theoretical dissolved oxygen profiles for the Pacific and Atlantic Ocean. 41
5.5 Theoretical dissolved carbon dioxide profiles for the Pacific and Atlantic Ocean. . 42
5.6 Theoretical temperature profile for a typical open ocean location in a mid-latitude region. 44
5.7 Examplary temperature profiles for three different locations at varying latitudes. 45
5.8 Theoretical density profile for the open ocean at a mid-latitude location. 46
6.1 Measurement for temperature, oxygen and density over depth at location U1362A. 49

6.2 Measurement for temperature, oxygen and density over depth at location U1362B. 49
6.3 Measurement for temperature, oxygen and density over a depth from 0 to 500 metres at location U1362A. 50
6.4 Measurement for temperature, oxygen and density over a depth from 0 to 500 metres at location U1362B. 50
6.5 Measurement of the salinity over depth. 51
6.6 Measurement of the sound velocity over depth. 51
6.7 Measurement of the attenuation and transmissivity of a beam over depth. 52
6.8 Schematic of the setup for analysing water samples. 54
6.9 Front view of the setup for analysing water samples. 55
6.10 Top view of the setup for analysing water samples. 55
6.11 Measurement of the water sample from 500 m a.G.. 57
6.12 Measurement of the water sample from 1000 m a.G.. 58
6.13 Measurement of the water sample from 50 m a.G.. 59
6.14 Plot of the measurement of the 500 m a.G. sample. 60
6.15 Plot of the measurement of the 1000 m a.G. sample. 60
6.16 Plot of the measurement of the 50 m a.G. sample. 60
6.17 Plot of the measurement of the 500 m a.G. sample with the heights at and above 269 cm excluded. 60
6.18 Plot of the measurement of the 500 m a.G. sample with the heights above 252 cm excluded. 60
6.19 Plot of the measurement of the 500 m a.G. sample with the heights at and above 252 cm excluded. 60
6.20 Plot of the first measurement of distilled water. 62
6.21 Plot of the second measurement of distilled water. 63
6.22 Plot of the pre-selected data of the second measurement of distilled water. 63
6.23 The third measurement of distilled water. 63
6.24 The fourth measurement of distilled water. 63
6.25 Plot of the second measurement of the 500 m a.G. sample. 65
6.26 Plot of the second measurement of the 500 m a.G. sample with the excluded data. 66
6.27 The intensity over time with only air in the setup. 67
6.28 The intensity over time for distilled water in the sample pipe and air in the empty sample pipe. 68
6.29 The first measurement run of distilled water with adopted execution. 69
6.30 The second measurement of distilled water with adopted execution. 70
6.31 The third measurement of distilled water with adopted execution. 71
6.32 The fourth measurement of distilled water with adopted execution. 72
6.33 Plot of the first preliminary measurement of the scintillator Sasol LAB. 73
6.34 Plot of the second preliminary measurement of the scintillator Sasol LAB. 73
7.1 Schematic sketch of the functionality and positioning of the Oceanography Sensor Interface. 74
7.2 Simplified schematics of a inductive coupling circuit and a magnetic resonance coupling circuit.. 75

7.3 Comparison of efficiency and transmitted power over distance of inductive coupling and magnetic resonance coupling. 76
7.4 Plot of comparison of inductive and magnetic resonance coupling. 77
7.5 Picture of the PCB coils. 78
7.6 Plot of maximal coupling efficiency of PCB coils over distance. 78
7.7 Comparison of coupling ability for shielded and not-shielded coils. 79
7.8 Setup for testing the impact of wireless power transfer on a PMT signal. 80
7.9 Screenshot of the Oscilloscope measuring the power system and PMT signal. . . 80
7.10 Setup for testing the evaluation device of Fraunhofer ENAS. 81
7.11 Screenshot of the Oscilloscope measuring the power transmitted by the evaluation device. 81
7.12 Technical drawing of the outside of the inner mounting. 84
7.13 Technical drawing of the inside of the inner mounting. 84
7.14 Conceptional design of the outer housing attached to the P-OM. 85
7.15 Conceptional design of the outer housing. 85
A.1 Coating Procedure first part. 87
A.2 Coating Procedure second part. 88
A.3 Coating Procedure third part. 89
A.4 Procedure of Gel Pad Production first part. 90
A.5 Procedure of Gel Pad Production second part. 91
A.6 Procedure of Gel Pad Production third part. 92
A.7 Procedure of Gel Pad Production fourth part. 93
A.8 Procedure of Gel Pad Production fifth part. 94
A.9 Procedure of Gel Pad Production sixth part. 95
A.10 Procedure of PMT integration first part. 96
A.11 Procedure of PMT integration second part. 97
A.12 Procedure of PMT integration third part. 98

List of Tables

1 Listing of approximate absorption and effective scattering lengths with resulting attenuation length for different locations of neutrino telescopes. 14
2 List of requirements for the PMTs of P-ONE-1. 25
3 Listing of the attenuation lengths for the different water samples. 59
4 Listing of the attenuation lengths for different selected data of the 500 m a.G. sample. 61
5 Listing of the attenuation lengths of distilled water. 64
6 Listing of the attenuation lengths for the different runs of measurement of distilled water. 70

References

[1] Maurizio Spurio. *Particles and Astrophysics*. Cham: Springer International Publishing, 2015. DOI: 10.1007/978-3-319-08051-2.

[2] Thomas K. Gaisser, Ralph Engel, and Elisa Resconi. *Cosmic Rays and Particle Physics*. 2nd ed. Cambridge: Cambridge University Press, 2016. ISBN: 9781139192194.

[3] R. Abbasi et al. *Observation of high-energy neutrinos from the Galactic plane*. 2023. DOI: 10.1126/science.adc9818.

[4] IceCube Collaboration. *Neutrino emission from the direction of the blazar TXS 0506+056 prior to the IceCube-170922A alert*. 2018. DOI: 10.1126/science.aat2890.

[5] IceCube Collaboration et al. *Evidence for neutrino emission from the nearby active galaxy NGC 1068*. 2022. DOI: 10.1126/science.abg3395.

[6] Christian Spannfellner. "Development of pathfinder missions and instruments for the Pacific Ocean Neutrino Experiment". 2020.

[7] Imre Bartos and Marek Kowalski. *Multimessenger astronomy*. Version: 20170401. Physics world discovery. Bristol: IOP Publishing, 2017. ISBN: 9780750313698. DOI: 10.1088/978-0-7503-1369-8. URL: https://iopscience.iop.org/book/978-0-7503-1369-8.

[8] Marica Branchesi. "Multi-messenger astronomy: gravitational waves, neutrinos, photons, and cosmic rays". In: *Journal of Physics: Conference Series* 718 (2016), p. 022004. ISSN: 1742-6588. DOI: 10.1088/1742-6596/718/2/022004.

[9] *LIGO´s Dual Detectors*. 2024. URL: https://www.ligo.caltech.edu/page/ligo-detectors (visited on 01/03/2024).

[10] *A Worldwide Network - Advanced Virgo*. URL: http://public.virgo-gw.eu/a-worldwide-network/ (visited on 01/03/2024).

[11] Paolo Favali, Laura Beranzoli, and Angelo de Santis. *SEAFLOOR OBSERVATORIES*. Berlin, Heidelberg: Springer Berlin Heidelberg, 2015. ISBN: 978-3-642-11373-4. DOI: 10.1007/978-3-642-11374-1.

[12] Kai Zuber. *Neutrino Physics*. Boca Raton: CRC Press, 2020. DOI: 10.1201/9781315195612.

[13] Kevin McFarland. *Neutrino Interactions*. 2008.

[14] Christian Spiering. "Neutrino Detectors Under Water and Ice". In: *Particle Physics Reference Library*. Ed. by Christian W. Fabjan and Herwig Schopper. Cham: Springer Nature, 2020, pp. 785–822. ISBN: 978-3-030-35317-9. DOI: 10.1007/978-3-030-35318-6{\textunderscore}17.

[15] Schematic Cherenkov Light Cone. URL: http://large.stanford.edu/courses/2014/ph241/alaeian2/.

[16] József Kónya and Noémi M. Nagy. *Nuclear and Radiochemistry*. San Diego, CA, USA: Elsevier Science, 2018. ISBN: 978-0-12-813643-0.

[17] IceCube Collaboration et al. *Measurement of South Pole ice transparency with the IceCube LED calibration system*. 2013. DOI: 10.1016/j.nima.2013.01.054.

[18] M. Aker et al. "Direct neutrino-mass measurement with sub-electronvolt sensitivity". In: *Nature Physics* 18.2 (2022), pp. 160–166. ISSN: 1745-2473. DOI: 10.1038/s41567-021-01463-1.

[19] Imma Rea. "Rea_I_C_PhD_Thesis_semifinal2 copia". PhD thesis.

[20] A. Faessler et al. *Search for the Cosmic Neutrino Background.* DOI: 10.1088/1742-6596/580/1/012040.

[21] Brent Follin et al. *First Detection of the Acoustic Oscillation Phase Shift Expected from the Cosmic Neutrino Background.* DOI: 10.1103/PhysRevLett.115.091301.

[22] Carlo Giunti and Chung Wook Kim. *Fundamentals of neutrino physics and astrophysics.* Reprint. Oxford: Oxford University Press, 2016. ISBN: 9780198508717. DOI: 10.1093/acprof:oso/9780198508717.001.0001.

[23] Brigitte Falkenburg and Wolfgang Rhode. *From Ultra Rays to Astroparticles.* Dordrecht: Springer Netherlands, 2012. DOI: 10.1007/978-94-007-5422-5.

[24] Tonia M. Venters et al. *Energetic Particles of Cosmic Accelerators II: Active Galactic Nuclei and Gamma-ray Bursts.* 2019.

[25] Robert H. Stewart. *Introduction to physical Oceanograpy.* 2008th ed. 2008.

[26] Nicolai Bailly et al. *Two-year optical site characterization for the Pacific Ocean Neutrino Experiment (P-ONE) in the Cascadia Basin.* DOI: 10.1140/epjc/s10052-021-09872-5.

[27] A. Karle et al. "IceCube — the next generation neutrino telescope at the South Pole". In: *Nuclear Physics B - Proceedings Supplements* 118 (2003), pp. 388–395. ISSN: 09205632. DOI: 10.1016/S0920-5632(03)01337-9. URL: http://arxiv.org/pdf/astro-ph/0209556.pdf.

[28] M. G. Aartsen et al. "The IceCube Neutrino Observatory: instrumentation and online systems". In: *Journal of Instrumentation* 12.03 (2017), P03012–P03012. DOI: 10.1088/1748-0221/12/03/P03012. URL: http://arxiv.org/pdf/1612.05093.pdf.

[29] *IceCube Website.* URL: https://icecube.wisc.edu/ (visited on 01/09/2024).

[30] Annarita Margiotta. *The KM3NeT deep-sea neutrino telescope.* 2014. DOI: 10.1016/j.nima.2014.05.090. URL: http://arxiv.org/pdf/1408.1392.pdf.

[31] Petros A. Rapidis. "The NESTOR underwater neutrino telescope project". In: *Nuclear Instruments and Methods in Physics Research Section A: Accelerators, Spectrometers, Detectors and Associated Equipment* 602.1 (2009), pp. 54–57. ISSN: 01689002. DOI: 10.1016/j.nima.2008.12.216. URL: https://www.sciencedirect.com/science/article/pii/S016890020801824X.

[32] E. Migneco et al. "Status of NEMO". In: *Nuclear Instruments and Methods in Physics Research Section A: Accelerators, Spectrometers, Detectors and Associated Equipment* 567.2 (2006), pp. 444–451. ISSN: 01689002. DOI: 10.1016/j.nima.2006.05.257. URL: https://www.sciencedirect.com/science/article/pii/S0168900206010473.

[33] M. Ageron et al. *ANTARES: The first undersea neutrino telescope.* 2011. DOI: 10.1016/j.nima.2011.06.103. URL: http://arxiv.org/pdf/1104.1607.pdf.

[34] KM3NeT Collaboration. *The KM3NeT multi-PMT optical module*. 2022. URL: http://arxiv.org/pdf/2203.10048.pdf.

[35] A. Margiotta. *The KM3NeT infrastructure: status and first results*. 2022. URL: http://arxiv.org/pdf/2208.07370.pdf.

[36] KM3NeT Collaboration, ed. *Astroparticle physics with ARCA*. URL: https://www.km3net.org/research/physics/astronomy-with-arca/.

[37] *Particle physics with ORCA*. URL: https://www.km3net.org/research/physics/particle-physics-with-orca/.

[38] A.V. Avrorin et al. "Status of the Baikal-GVD project". In: *Nuclear Instruments and Methods in Physics Research Section A: Accelerators, Spectrometers, Detectors and Associated Equipment* 692 (2012), pp. 46–52. ISSN: 01689002. DOI: 10.1016/j.nima.2011.12.106. URL: https://www.sciencedirect.com/science/article/pii/S0168900211023667.

[39] Yury Malyshkin. "Baikal-GVD neutrino telescope: Design reference 2022". In: *Nuclear Instruments and Methods in Physics Research Section A: Accelerators, Spectrometers, Detectors and Associated Equipment* 1050 (2023), p. 168117. ISSN: 01689002. DOI: 10.1016/j.nima.2023.168117. URL: https://www.sciencedirect.com/science/article/pii/S0168900223001079.

[40] Niklas Retza. "The Pacific Ocean Neutrino Experiment: Advancements in the Optical Module Development for the First Detector Line of P-ONE". Technical University Munich, 2023.

[41] Lisa Johanna Schumacher et al. "PLEνM: A global and distributed monitoring system of high-energy astrophysical neutrinos". In: *PoS-ICRC* (), p. 1185. DOI: 10.22323/1.395.1185. URL: http://arxiv.org/pdf/2107.13534.pdf.

[42] Elisa Resconi and P-ONE Collaboration. *The Pacific Ocean Neutrino Experiment*. 2021. URL: http://arxiv.org/pdf/2111.13133.pdf.

[43] H. Paul Johnson, Susan L. Hautala, and Tor A. Bjorklund. *The thermal environment of Cascadia Basin*. DOI: 10.1029/2011GC003922.

[44] Christopher Barnes et al. "Final installation and initial operation of the world's first regional cabled ocean observatory (NEPTUNE Canada)". In: *Canadian Meteorological and Oceanographic Society Bulletin* 38 (2010), pp. 89–96.

[45] Christian Haack and Lisa Schumacher. "Machine-learning aided detector optimization of the Pacific Ocean Neutrino Experiment". In: 2023, p. 1059. DOI: 10.22323/1.444.1059.

[46] *P-ONE Website*. URL: https://www.pacific-neutrino.org/p-one/how-p-one-will-be-designed.

[47] M. Boehmer et al. *STRAW (STRings for Absorption length in Water): pathfinder for a neutrino telescope in the deep Pacific Ocean*. 2019. DOI: 10.1088/1748-0221/14/02/P02013. URL: http://arxiv.org/pdf/1810.13265.pdf.

[48] Kilian Holzapfel et al. *STRAW-b (STRings for Absorption length in Water-b): the second pathfinder mission for the Pacific Ocean Neutrino Experiment*. 2024. arXiv: 2310.16714 [astro-ph.IM].

[49] Christian Spannfellner. "Design of the Pacific Ocean Neutrino Experiment's First Detector Line". In: 2023, p. 1219. DOI: 10.22323/1.444.1219.

[50] Dilraj Ghuman, Felix Henningsen, and Matthias Danninger. "The Acoustic Calibration System for the Pacific Ocean Neutrino Experiment". In: *Proceedings of 38th International Cosmic Ray Conference — PoS(ICRC2023)*. Ed. by Kimihiro Okumura and Takayuki Saito. Trieste, Italy: Sissa Medialab, 2023, p. 1112. DOI: 10.22323/1.444.1112.

[51] Jakub Stacho et al. "Development of Calibration Light Sources for the Pacific Ocean Neutrino Experiment". In: *Proceedings of 38th International Cosmic Ray Conference — PoS(ICRC2023)*. Ed. by Kimihiro Okumura and Takayuki Saito. Trieste, Italy: Sissa Medialab, 2023, p. 1113. DOI: 10.22323/1.444.1113.

[52] "Felix Henningsen - The self-monitoring precision calibration light source for the IceCube Upgrade". PhD thesis.

[53] T. Anderson et al. "Design and performance of the multi-PMT optical module for IceCube Upgrade". In: *PoS-ICRC* (). URL: http://arxiv.org/pdf/2107.11383.pdf.

[54] HAMAMATSU. *Photomultiplier Tubes - Basics and Applications*. 2017. URL: https://www.hamamatsu.com/content/dam/hamamatsu-photonics/sites/documents/99_SALES_LIBRARY/etd/PMT_handbook_v4E.pdf.

[55] Lasse Halve and Johannes Werthebach. "Design of an Efficient, High-Throughput Photomultiplier Tube Testing Facility for the IceCube Upgrade". In: *PoS-ICRC* (). URL: http://arxiv.org/pdf/2107.09954.pdf.

[56] S. Adrián-Martínez et al. "A method to stabilise the performance of negatively fed KM3NeT photomultipliers". In: *Journal of Instrumentation* 11.12 (2016), P12014–P12014. DOI: 10.1088/1748-0221/11/12/P12014.

[57] Martin Antonio Unland Elorrieta. *Development, simulation, and characterisation of a novel multi-PMT optical module for IceCube Upgrade with emphasis on detailed understanding of photomultiplier performance parameters*. 2023. DOI: 10.5281/ZENODO.8121320.

[58] Florian Trittmaack. "Investigations of background light sources in photomultiplier tubes operated at negative high voltages". Master Thesis. Westfälische Wilhelms-Universität Münster.

[59] Kontakt Chemie. *Safety Data Sheet Plastik 70 Super*.

[60] Kontakt Chemie. *Datasheet Thinner 70*.

[61] Ben Nührenbörger. "Bachelorthesis_Ben_Nührenbörger_2023". Technical University Munich, 2023.

[62] *Introduction to Oceanography*.

[63] *ONC Multimedia Maps Website*. URL: https://www.oceannetworks.ca/multimedia/maps/ (visited on 2024).

[64] *EPA Website about Effects of Acidification on Ocean*. URL: https://www.epa.gov/ocean-acidification/effects-ocean-and-coastal-acidification-ecosystems (visited on 2024).

[65] *C-Star Transmissiometer SeaBird Scientific*. URL: https://www.seabird.com/c-star-transmissometer/product-details?id=60762467717.

[66] "JUNO physics and detector". In: *Progress in Particle and Nuclear Physics* 123 (2022), p. 103927. ISSN: 0146-6410. DOI: 10.1016/j.ppnp.2021.103927. URL: https://www.sciencedirect.com/science/article/pii/S0146641021000880.

[67] epoinescu. *SLS301 Halogen Light Source Datasheet*. URL: https://www.thorlabs.com/drawings/7920f894eef30056-5518BC48-9F96-163C-00752677554F21F6/SLS301-Manual.pdf (visited on 01/09/2024).

[68] Jamie LaCouture. *PM16-121-Powermeter*. URL: https://www.thorlabs.com/drawings/7920f894eef30056-5518BC48-9F96-163C-00752677554F21F6/PM16-121-SpecSheet.pdf (visited on 01/09/2024).

[69] *Maya2000Pro Data Sheet*. URL: https://spectrecology.com/wp-content/uploads/2020/11/Maya2000Pro-Data-Sheet.pdf (visited on 01/09/2024).

[70] *Atik-APX60 Datasheet*. URL: https://atikcameras.wpenginepowered.com/wp-content/uploads/2023/04/23-89-Atik-APX-Series-4PPA4.pdf (visited on 01/09/2024).

[71] *Dockweiler Pipes Characteristics*. URL: https://www.dockweiler.com/en/products/tubes-and-fittings.

[72] *Datasheet Elix Reference Water Purification Systems*.

[73] F. Amat et al. "Measuring the attenuation length of water in the CHIPS-M water Cherenkov detector". In: *Nuclear Instruments and Methods in Physics Research Section A: Accelerators, Spectrometers, Detectors and Associated Equipment* 844 (2017), pp. 108–115. ISSN: 01689002. DOI: 10.1016/j.nima.2016.11.032. URL: https://www.sciencedirect.com/science/article/pii/S016890021631186X.

[74] *Datasheet Oxygen Sensor 4831/4831f*. URL: https://www.aanderaa.com/media/pdfs/d403_aanderaa_oxygen_sensor_4831_4831f.pdf (visited on 2024).

[75] *Datasheet SBE 38 Digital Oceanographic Thermometer*. URL: https://www.seabird.com/sbe-38-digital-oceanographic-thermometer/product-downloads?id=60762467703 (visited on 2024).

[76] *Datasheet DST CTD online Sensor*. URL: https://www.star-oddi.com/media/1/dst-ctd-online-data-sheet-2.pdf (visited on 2024).

[77] Takehiro Imura. *Wireless Power Transfer*. Singapore: Springer Singapore, 2020. DOI: 10.1007/978-981-15-4580-1.

[78] *Arduino MKR WiFi 1010 Website*. URL: https://store.arduino.cc/products/arduino-mkr-wifi-1010.

[79] *Arduino UNO WiFi REV2 Website*. URL: https://store.arduino.cc/products/arduino-uno-wifi-rev2.

[80] *Arduino IDE 2.3.0 Website*. URL: https://www.arduino.cc/en/software.